Unraveling the Interplay between Structure and Photophysics in Colloidal Quantum Dot Nanostructures

By

Kemar Reid

Dissertation
Submitted to the Faculty of the
Graduate School of Vanderbilt University
in partial fulfillment of the requirements
for the degree of

DOCTOR OF PHILOSOPHY
in
Interdisciplinary Materials Science

May 10, 2019

Nashville, Tennessee

Approved:

Sandra J. Rosenthal, Ph.D.

Rizia Bardhan, Ph.D.

Richard F. Haglund, Ph.D.

Janet E. Macdonald, Ph.D.

Jason G. Valentine, Ph.D.

To my family

and

my future wife, Kristen

ACKNOWLEDGMENTS

To my parents—I am forever grateful for your support, humility and sacrifice. Mom, you are my inspiration. To my family—thank you for walking through life with me and for your unconditional support and encouragement.

To my advisor, Dr. Sandra Rosenthal—when I reflect on the past few years, some of my most challenging, but also rewarding experiences have been tied to my research in your lab. Thank you for the opportunity to be apart of groundbreaking work. I knew early on that your flexible approach and promotion of independent learning would be a good fit for me. I hope you have found my contributions worthy of the mentoring and support you have provided. The deep passion you bring to your work will continue to inspire me.

My committee members have provided invaluable insight and suggestions for my research. Thank you all for serving on my committee. Dr. Haglund, your thought provoking questions have pushed me to strive for a deeper understanding of my work. Thank you for your knowledgeable insight. I am sorry I did not take your class. Dr. Valentine —I wish we could have had more conversations about research. I have learned a lot from your valuable feedback during my examinations. Thank you. Dr. Bardhan—I have had a great experience working with you and your students on some interesting research topics. Thank you for allowing me to contribute to that work and for taking the time to serve on my committee. Dr. Macdonald—as a passionate researcher, your willingness to help others is inspiring. Thank you for our collaborations and discussions about research, in particular about nanoparticle synthesis.

I also have the deepest sense of gratitude for my co-PI, Dr. James McBride. James, thank you for keeping me on track and for advising and mentoring me from the very beginning. Your in-depth knowledge and willingness to help advance everyone in our lab has not gone unnoticed. Thank you for all your contributions to the work presented in this dissertation and to each of my manuscripts. When I look at these accomplishments, along with completing my first marathon, you were a cornerstone—thank you.

To the past and present crew in the laser lab—it has been a great experience working with each of you. Dr. Noah Orfield—Thank you for on-boarding me, contributing innovative research that I continue to use as a reference point and for encouraging me even following your departure. Your curious and composed nature, along with your dedication to your work (and running!) continues to inspire me. Nathaniel—your attention to detail, patience and maintenance of our laser system has not gone unnoticed. I have also appreciated our conversations about research, which have helped me tremendously. Thank you. Sophie, your experiences at Los Alamos along with your passion and resourcefulness will serve you well. Good luck! Dr. Lloyd Davis—thank you for your help with configuring the fluorescence microscope.

To my peers in the Rosenthal lab—thank you for providing a welcoming environment to work in. I am humbled to have been a part of the many accomplishments of the lab. Dr. Danielle Bailey—much like your Taylor Swift songs midway on our long-runs while marathon training, your positive energy was welcomed and encouraging in the Rosenthal lab. Louie—I have appreciated our conversations about one of my favorite things, music. Your determination and inquisitive nature will serve you well. Good luck to everyone!

I have a few collaborators that I would also like to acknowledge. Dr. Edward Sargent, Dr. Fengia Fan and Dr. Oleksandr Voznyy—thank you providing the material for the work in Chapter 3. Also, I owe a huge thanks to Dr. Andrew La Croix in the Macdonald lab at Vanderbilt for providing the material for the work in Chapter 5. Thank you for your willingness to share your knowledge of synthetic chemistry as I gained direction with this project.

I am tremendously grateful for the opportunities I have gained through my work at Vanderbilt University. I was very fortunate to be funded by a NSF research grant (CHE-1506587). I would also like to thank Vanderbilt Institute of Nanoscale Science and Engineering (VINSE) for a research fellowship.

To all of my friends who have supported me throughout this process—thank you! Andrew and Kemal–thank you for being a constant source of encouragement during this time. To my Nashville friends and roommates—Bobby, Kyle, Lindsay and Alex in different ways, you made my time in Nashville a great experience and I will always be grateful for that.

Finally, to my fiancee and best friend Kristen. Our time together has been the most fulfilling in my life. You inspire me in so many ways. Thank you for your patience, compassion and support throughout this process. None of this would be possible without you. You are my rock! I can't wait to see where life takes us next. I would also be remiss not to give a special shout out to my trusted companion, our dog, Bo. Thank you for the morning walks that allowed me to start my day off right with a clear headspace. Thanks buddy!

TABLE OF CONTENTS

LIST OF TABLES

Table Page

LIST OF FIGURES

Chapter 1

Introduction

1.1 Background and Motivation

Following the pioneering efforts of Louis Brus, Alexei Ekimov and Alexander Efros in the early 1980s,[1–3] there has been an explosive growth in the study and development of semiconductor nanocrystals with spatially confined electronic excitations. Owing to quantum size effects at the nanoscale, these "zero-dimensional" nanostructures, popularly referred to as quantum dots (QDs), feature tunable photophysical properties not observed in bulk. Furthermore, structures can be assembled on a large scale in solution (as colloids), enabling their use as solution-processable reagents in the development of novel functional materials. These features, significantly expanded prospects for one the most relevant classes of materials: semiconductors—captivating the attention of a diverse research community. In the three decades since they were first introduced, QDs have been successfully implemented in a wide array of applications, with the transformative potential to address many important technological challenges. These applications range from efficient solid-state lighting[4] and solar concentrators[5] to low-threshold lasers[6], wide-gamut displays[7] and robust fluorescent probes for biological imaging.[8]

To understand the effects of spatial confinement, it is important to first consider the excited state in a bulk semiconductor. When a semiconductor is struck by a photon with energy equal to or greater than its bandgap (E_g), an electron is promoted from the valence band (VB) to the conduction band (CB) of the material, leaving a hole in the VB. If the coulomb attraction (binding energy (E_b)) between the electron and hole is negligible, the generated electron and hole behave as free carriers and have no interactions with each other. However, if the binding energy between the two exceeds the thermal energy, an exciton—bound electron and hole pair—is formed. In this configuration, the preferred separation between the electron and hole is given by the exciton Bohr radius (a_0) of the material.

The effect of spatial confinement to small scales, is that, eventually a size regime is reached where the dimensions of the semiconductor is on the order of, or smaller than the Bohr radius. At this length scale, the exciton becomes 'squeezed' and can no longer achieve a favorable separation between the electron and hole. From this perspective, a QD can be thought of as a three -dimensional potential box that confines the motion of the electron and hole. This induces size-dependent transformations in the density of electronic states and in the energy separation between them. As the size of the QD is decreased, this manifests in an increase in the bandgap energy and the emergence of discrete atom-like energy levels near the edges of the VB and CB (Figure 1.1.).[9] This effect is also commonly referred to as quantum confinement and allows one to tune the properties of QDs by changing their size, while keeping the composition the same. A striking example of this phenomena, is the ability to drastically tune the absorbance and photoluminescence (PL)—over a wide spectral gamut—simply by making adjustments to the dimensions of the QD.

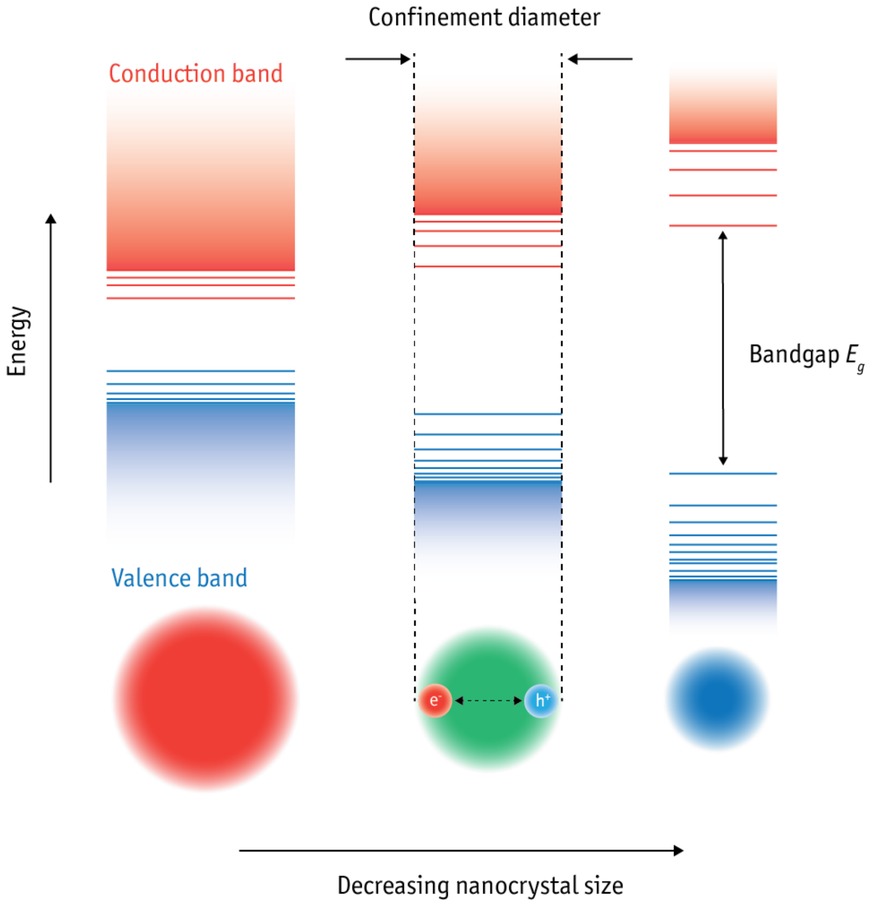

Figure 1.1: Illustration of quantum confinement. As the size of the QD decreases the band gap energy increases, while discrete energy levels develop at the edges of the conduction and valence band. The energy spacing between the levels at the band-edge also increases with decreasing size.

Although this conceptual quantum particle-in-a-box view provides a useful framework for understanding many of the fundamental properties of QDs, synthesized nanostructures represent more complex physical systems. At its simplest, a colloidal QD nanostructure comprises an inorganic core of a semiconductor material, surrounded by a passivating layer of organic surfactants. The core may contain anywhere from a few hundred to tens of thousands of atoms. Figure 1.2 presents a micrograph of a QD capturing the location and density of the atoms contained. Considered on the atomic scale, QDs are, in fact, very large structures, with many possible configurations of their atoms and morphology. Furthermore, due to the large surface-to-volume ratios encountered at nanometer sizes, a large fraction of these atoms lie at the surface—at the interface between the core and organic ligands. As a result, the surfaces of QDs make up a large part of their structure. These surface atoms have fewer neighbors, are associated with higher free energies, and can undergo substantial reconstructions of atomic positions.[10] In addition, the surface atoms may expose broken chemical bonds, in an amount that depends on the coverage of the organic ligands. Therefore, the conformation and ordering of passivating ligand molecules also have important consequences for the structure of QDs. It is further possible and often beneficial to construct QD nanostructures that consist two (or more) different semiconductor materials—configured in a core-shell system.[11] The atomic landscape of such QD heterostructures can be quite complex, as they already have two types of interfaces. The structure at the core-shell interface may be abrupt with no exchange between the core and shell atoms or interfacially mixed. Moreover, any mismatch between the lattice parameters of the core and shell materials, may be compensated by introducing broken bonds and crystalline defects at this interface. Such lattice mismatch may also impart considerable strain on the QD core that create changes in the bond lengths of the underlying lattice.[12] Clearly, QDs are remarkably complex structures.

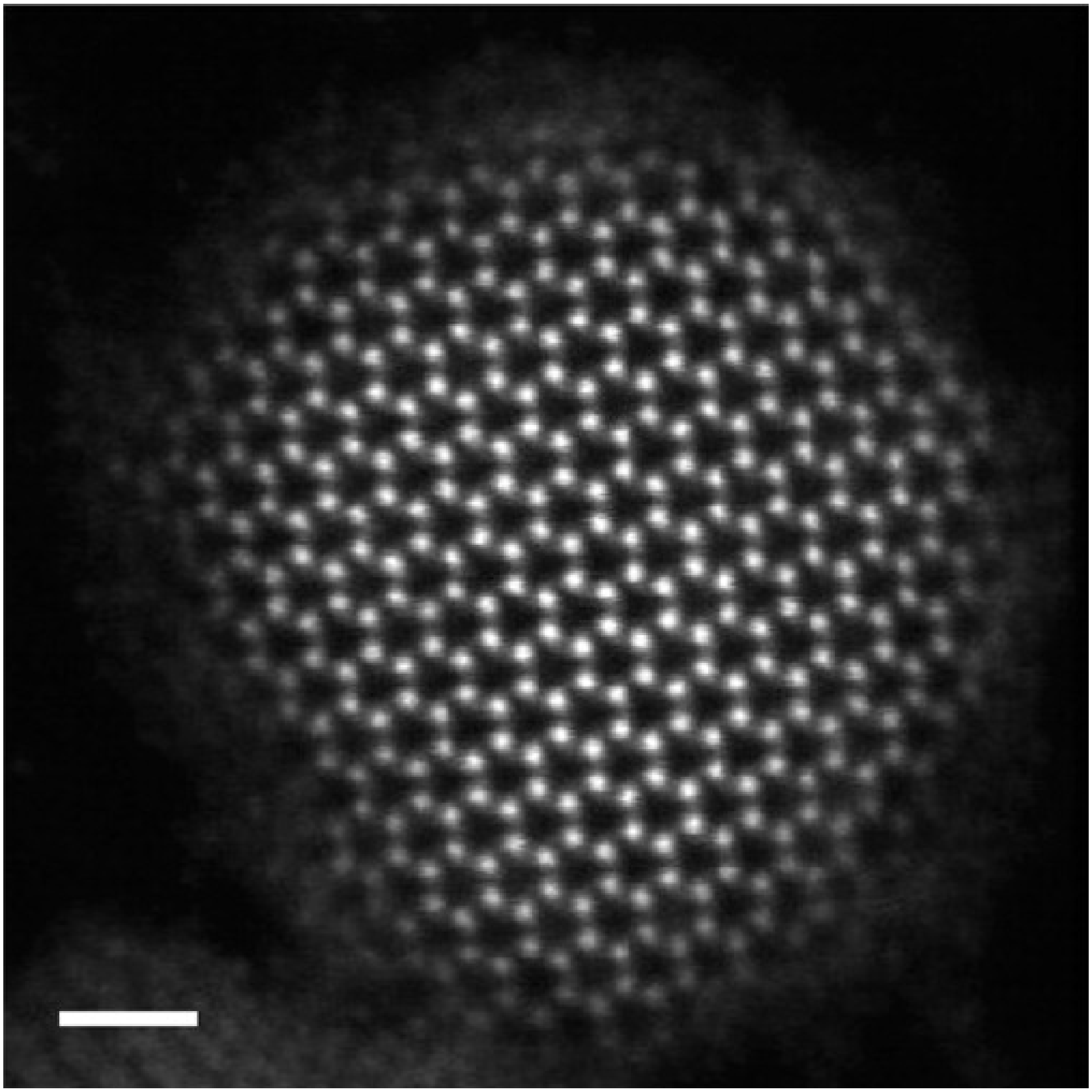

Figure 1.2: Abberation-corrected scanning transmission electron microscopy micrograph showing the atomic structure of a CdSe QD. Scale bar is 1 nm.

These many structural considerations may also influence the properties of QDs by having profound effects on their electronic structure and spatially confined excitations. For instance, unsaturated chemical bonds and defects at surfaces and interfaces can introduce localized electronic states within the band gap that can capture charge carriers—electrons and holes—and degrade the electrical and optical properties of QD structures.[13]Coupling of excitons to vibrations of the surface and passivating ligand molecules influence charge carrier lifetimes, charge transport and the line widths of optical transitions.[14] Chemical gradients at the interface of core-shell structures affect optical gain thresholds and the morphology of a QD can dictate the configuration of the energy levels near the band edges of the electronic structure.[15, 16]

Furthermore, any of these structural factors can vary between QD nanostructures within the same synthetic product—as random growth changes present in solution schemes may produce a myriad of QD architectures. Given the hundreds to tens of thousands of atoms that make up QDs, the number of possible structural configurations of their atoms is probably even larger than the number of QDs that comprise the sample. Even a single atom displacement in such quantum-confined structures could yield large changes in their behavior. The result of this structural disorder are well illustrated in the spectral properties of QD dispersions containing millions of particles. As mentioned previously, theory predicts that QDs should have discrete, atom-like transitions.[1] However, spectral measurements reveal an inherent broadening of the spectral transitions of QD ensembles (Figure 1.3). This inhomogeneous broadening effect is due to the array of sizes and morphologies—however slight—of QDs often present in synthesized samples.

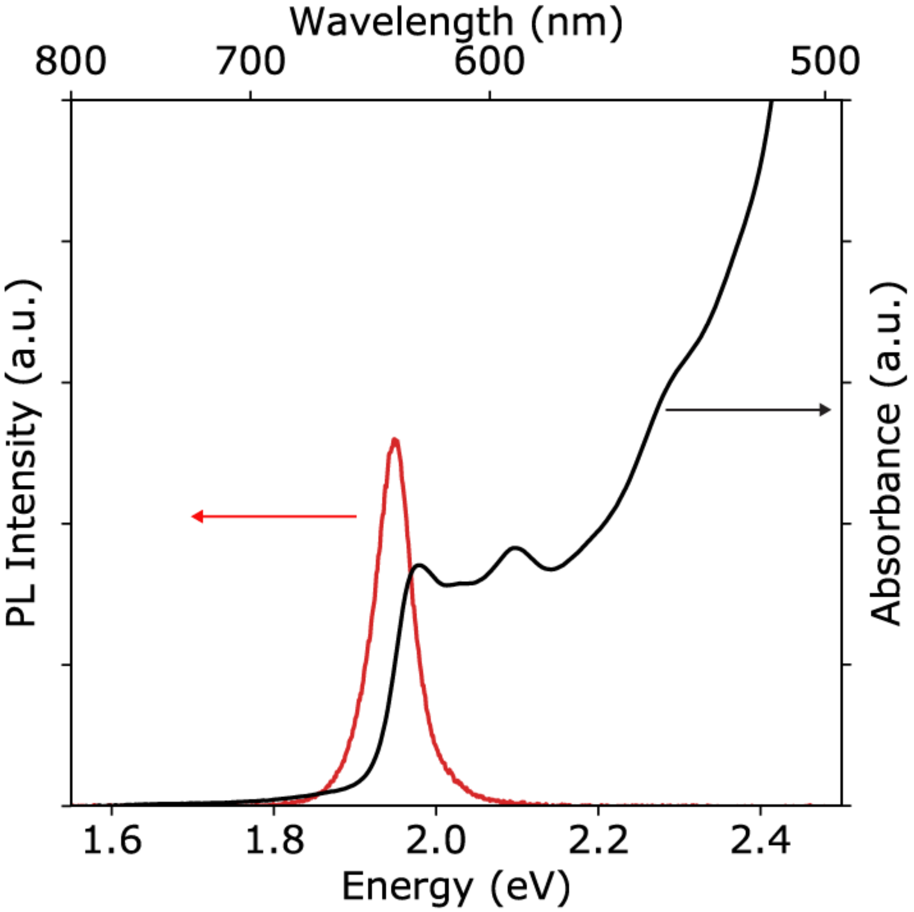

Figure 1.3: Inhomogeneously broadened absorption and emission spectra of a sample due to the distribution of QD shapes and sizes.

QD nanostructures are usually developed for a specific function: Giant shell architectures are being implemented in solid state lighting,[17] dot-in-rod designs are being developed for water splitting[18] and strain-engineered structures show promise as lasing materials.[6] In each case, the desired result depends on the properties of the QDs (e.g. high brightness and stability, long range charge carrier separation and low optical gain thresholds). In turn, these properties depend—sensitively—on the variety of structures present in QD samples. The growing use of QD nanostructures in these and other applications rely, crucially, on advancements in synthetic methodologies and advancements in the understanding of their behaviors. Therefore, it is imperative to gain a high-level understanding of the interplay between the physical structure and properties of QD nanostructures, in order to develop rational approaches to guide their design. This understanding could even lead to the discovery of unforeseen structure-property relationships that enable new means for controlling behavior. While approaches that measure the properties of millions of nanostructures at a time are highly valuable in this endeavor, diverging structures and photophysics are invariably averaged over in ensemble investigations. This not only results in the loss of a wealth of information but also obscures the intrinsic properties of individual nanostructures. In order to decode this information, it then becomes necessary to study QD nanostructures one at a time.

1.2 Single Quantum Dot Optical Spectroscopy

1.2.1 Photoluminescence Blinking

The first report of the detection and optical spectroscopy on single QDs came from the Bawendi group in 1996.[19] In this pioneering work, fluorescence from a sparse density of QDs was collected with a fluorescence microscope. Surprisingly, the emission from individual QDs was seen to randomly turn "on" and "off" in a binary fashion, even under constant illumination. This intermittency of the single QD PL was unexpected given the excellent stability observed in ensemble. The pattern of the "blinking" behavior was also dependent on the particular QD under examination—individual structures from the same synthetic batch often displayed different fluorescence signals. Additionally, the statistics of the duration of the on- and off-periods were shown to obey intricate power law distributions indicating a complex origin of the phenomena.[20]

One of the most commonly accepted explanation for blinking is the charging model.[21] The charging model states that a charged QD will stop emitting photons (i.e. turn "off") due to the interruption of radiative exciton recombination by non-radiative Auger processes. Several investigations, however, point out inconsistencies of the charging model in describing QD blinking behavior.[22, 23] Alternative models identify multiple recombination centers that switch between active and inactive conformations in QDs as the source of blinking—possibly *via* dynamic evolution of the surface or interfacial structure.[24, 25] Additionally, some studies indicate that blinking is actually a manifestation of both charging and recombination center processes that can occur in the same QD.[26–28] Even so, after more than two decades since its discovery, the exact origin(s) of QD blinking is still debated by the community.[29] Nonetheless, the foundational work by Bawendi revealed for the first time, divergent and complex behavior in the optical response of QDs.

Single QD blinking also has far-reaching consequences for the properties of the ensemble. By way of example, consider the PL quantum yield (QY), an important parameter that is routinely used to characterize the quality of QDs. Most QD preparations have sub-unity PL QYs, for reasons that are unclear from batch level investigations. However, after it was established that the emission efficiency of individual QDs approaches unity at their brightest,[30] it became apparent that blinking contributed to suboptimal quantum efficiencies of QD samples. This is because at any given time a fraction of particles will be dim or non-emissive. Blinking at the single QD scale is also linked to the photodarkening effect, in which the PL intensity from an array of nanostructures dim over time under constant excitation.[31] These observations illustrate the intimate connection between the properties of single QDs and ensemble behavior.

1.2.2 Spectral Behavior

In addition to uncovering the blinking phenomena, early single QD spectroscopy shed light on other aspects of the optical behavior of QDs. By dispersing the fluorescence signal from individual nanostructures, for example, it was possible to probe their spectral properties. It is well-established that the peak emission energy of a QD depends, minutely, on changes to its size. As a result, the PL spectrum in ensemble is broadened by any distribution in the sizes of QDs present in synthesized samples. Besides confirming this inhomogeneous broadening effect, spectral measurements on the single QD scale have also unearthed other dissimilarities in the emission of individual structures.[32] For instance, spectral features that report on the coupling of excitons to vibrations of the underlying structure have been shown to vary among QDs.[33] While the exact source for this divergence remains unclear, it has been postulated to stem from differences in the surface structure of QDs.[34]

Another effect displayed by single QDs is wandering of the emission energy in time—also known as spectral diffusion.[35] The associated energy shifts can be quite large—up to several meVs—and arise from random fluctuations of charges in the local environment of QDs. Such charge migrations may emanate from photo-induced re-arrangements of surface ligands or reconstructions of surface atoms.[36] The observation of spectral diffusion further emphasize the sensitive nature of QDs to structural changes and the power of single QD spectroscopy in extracting a wealth of information from these complex systems.

1.2.3 Time-resolved Photoluminescence Decay

Soon after these initial single QD experiments, time-resolved capabilities were added to the single QD spectroscopy tool set. These measurements enabled exploration of the processes affecting the relaxation of excited states (e.g. exciton) down to sub-nanosecond timescales. The first time-resolved studies on single QDs revealed appreciable heterogeneity in the PL decay between individual structures.[37] These measurements further indicated that much in the same way as PL intensity blinking, single QD PL decay were dynamic in time, implying a common origin. Together the results suggested that both averaging over inherent structural heterogeneities and temporal evolution in the PL dynamics of single nanostructures contribute to the complex PL decays typically observed for QD samples.

Subsequent to these measurements, it was demonstrated that changes in the PL decay of single QDs could also be multiplexed with other parameters, such as PL intensity in order to gain a deeper understanding of their behavior.[38] Such multiplexed experiments were instrumental, for example, in challenging the long-standing hypothesis that charging of nanocrystals alone was responsible for the blinking of QDs.[26]

1.2.4 Multiexciton Recombination

Unlike fluorescent organic molecules, QD nanostructures are capable of supporting multiple excitations at the same time. These excitations can interact to form bound multiexciton states known as multiexcitons. The control of multiexciton behavior has important ramifications for numerous applications of QDs. However, multiexcitons can be difficult to study and ensemble approaches only capture averaged behavior. In 2011, the Bawendi group demonstrated that photon correlation measurements employing a Hanbury Brown-Twiss setup, could be used with a single QD optical microscope to study the multiexciton properties of single QDs.[39] Specifically, this experiment was used to determine the efficiency of biexciton (two electron-hole pairs) emission from an individual QD structure.

In QDs, Auger recombination is a main source for loss of multiexciton efficiency. Therefore, the measurement of single QD biexciton quantum yield became the standard way to probe Auger recombination in QD samples. A major finding of the initial report was a considerable distribution of calculated single QD biexciton efficiency, which indicated variable levels of Auger suppression between individual nanostructures. This variation has since been corroborated by further studies and is speculated to result from slight differences in the structures of QDs present in synthesized samples including surface and crystal defects and chemical mixing at the interface of core-shell heterostructures.

1.3 Single Quantum Dot Electron Microscopy

1.3.1 Transmission Electron Microscopy

At the same time that single QD spectroscopy was being used to uncover new insights into the photophysical behavior of QD nanostructures, electron microscopy was also being employed to examine the structural nature of synthesized QD samples. Indeed, electron microscopy have been an indispensable tool in the development of QD nanostructures. As with single QD optical methods, a key advantage of electron microscopy is the ability to probe QD samples at the level of individual structures. Electron microscopy techniques further provide the most direct way to observe the many structural features of QDs. Techniques such as transmission electron microscopy (TEM) are still the standard for the determination of QD size and shape, and batch experiments readily yield useful information about their distribution in nanocrystal samples.[40] At high-resolution, TEM can also dispense vital information about QD orientation, morphology and crystal structure.[41]

1.3.2 Annular Dark-Field Scanning Transmission Electron Microscopy

Even though conventional TEM provides a highly useful probe of QD structure, TEM micrographs can be difficult to interpret due to the nature of image formation. Phase-contrast imaging in TEM rely on the presence of lattice fringes arising from the periodic structure of the crystal lattice. However, this periodicity is broken at the surface of QDs and nearby lattice defects which can complicate image interpretation. Another disadvantage of TEM is that the technique also suffer from contrast inversions with defocus and changes in the thickness of the sample. As a result, the structural detail that can be uncovered is often limited.[42]

Scanning transmission electron microscopy (STEM) techniques on the other hand provides a wealth of added information and afford micrographs that are easier to understand. In particular, the use of STEM with high angle annular dark-field (HAADF) detectors uses an incoherent imaging process, which produces images that can be directly related to the structure of the object being observed. Additionally, the intensity of the signal depends on the mass of the incident atom, providing atomic number contrast also known as Z-contrast—this contrast follows a power law relationship, Z^{α}, where α is between 1 and 2. As a result of these advantages, HAADF-STEM can capture greater structural detail than conventional TEM, including surface structure and can also be used to assess the chemical nature of QDs. Pioneering HAADF-STEM studies on QDs, for example, enabled the chemical identification of the atoms terminating distinct facets of CdSe nanocrystals.[43] The technique has also been used to visualize the nature of epitaxy in core-shell QD samples as well as in the observation of crystalline defects in these heterostructures.[44]

1.3.3 Energy Dispersive X-ray Spectroscopy

While HAADF-STEM imaging allows the identification of distinct chemical regions, the intensity in the STEM micrographs contains both chemical and thickness information. As a result, it can be difficult to discriminate the precise chemical structure of QD nanostructures. For this measurement, it is therefore useful to look for other techniques which the electron microscope may provide. An alternative method is energy dispersive X-ray spectroscopy (EDS), which can be used with STEM to determine the spatial composition of QD materials with high chemical precision.

STEM-EDS relies on the excitation and subsequent ejection of inner shell electrons of the atoms in a sample. Outer shell electrons then fills the empty inner shell levels while emitting X-rays of characteristic energy. As the STEM beam is scanned across the sample, the X-rays generated are measured and correlated with the beam position yielding the chemical composition of the material. In its infancy, the collection of high quality STEM-EDS elemental maps would require long acquisition times that greatly increased the likelihood of QD structural damage from the sustained electron dose. However, advancements in EDS detector design and efficiency in the past ten years now enable the collection of significantly higher X-ray counts from nanocrystal samples. The improved design allow these silicon drift detectors (SSD) to be located closer to the sample, increasing the solid angle for X-ray collection.[45] This improvement facilitates the acquisition of near atomically resolved chemical maps long before the QD sample undergo any appreciable damage.

1.4 Correlation of Structure and Photophysics of the Same Quantum Dot

Both single QD spectroscopy and electron microscopy affords powerful tools to probe the resultant array of structures often present in QD samples—revealing important microscopic and divergent features. However, these measurements have largely been uncorrelated. In most single nanocrystal studies, the structures of several nanostructures are measured and the optical properties of a few single QDs are separately determined. Although this approach provides valuable insight into the relationship between the structure and photophysics of QDs, it is also important to ascertain such relationships at the highest level of detail. A comprehensive view of the interplay between structure and function is crucial to achieving complete control over the behavior of QDs. Therefore, there also exists a need measure the structure and optical properties of the same QD.

The first published attempt at correlating single QD optical measurements with structural information collected on the same nanostructures was by the Banin group in 2002.[46] In this work, atomic-force microscopy (AFM) and single QD spectroscopy were used to simultaneously record a map of the topography and fluorescence from single QD nanostructures. This correlation proved to be very useful in revealing the presence of permanently non-radiative or "dark" structures in QD samples detrimental to ensemble PL QYs. However, AFM lacks the resolution required to provide any valuable structural insight. Therefore, a link between the observed optical behavior and structure was not established. In the same year, Basche *et al.*[47] reported a method using TEM to correlate atomic structure with optical measurements on the same QDs acquired before hand. One of the main challenges encountered with this correlation approach was a high level of ambiguity in matching the optical and structural information acquired for the same QD. This prohibited the collection of comprehensive datasets necessary to understand how subtle changes in QD structure impact optical behavior and ultimately influence the macroscopic properties of QD samples.

Recently, Orfield *et al.*[48] developed and demonstrated a simple platform to unambiguously correlate optical properties with the structures of the same QDs. The method utilizes inexpensive polymeric microshperes as placement markers such that the position of structures of interest can be specified in a straightforward and reproducible manner. This strategy facilitates a high fidelity in the classification of optical and atomic structural information collected *via* optical and electron microscopy, overcoming major hurdles in previous approaches. In addition, the simplicity of the correlation method enables large scale investigations of the array of structures and divergent behaviors in synthesized QD samples. Moreover, the strategy can be implemented using widely available optical and high-resolution electron microscopes.

Using this correlation platform, Orfield *et al.* investigated the detailed effects of structural heterogeneity on the optical properties of QDs in the same sample.[48] This work was the first to directly pinpoint and correlate specific surface defects to detrimental PL behavior in QDs, such as blinking. In addition, crystal structure, QD orientation and shell epitaxy were identified as important structural considerations that affect optimal performance of QD nanostructures. This study demonstrated the utility of the advanced single QD characterization methodology in providing additional insight into the properties that emerge in QD nanostructures and into the role of structure.

1.5 Overview

The aim of this dissertation is to: *examine the interplay between the structure and photophysics of different QD nanostructures using single QD characterization techniques; emphasize the need to establish direct structure-function relationships at the single QD scale to fully understand the properties of these complex nanostructures, and to provide an example in which the photophysics and atomic structure of individual QD nanostructures were correlated to acquire this information and uncover the role of surface roughness on excited state behavior.*

Chapter 1 of this dissertation lays the ground work and motivation for studying QD nanostructures at the single QD scale, in order to unravel structure-function connections necessary to further our understanding of their behavior. Chapter 2 outlines the implementation of the single QD experimental techniques used in this work.

In Chapter 3 the results of optical measurements on single CdSe-CdS core-shell nanostructures with a built-in anisotropic strain on the CdSe core are presented. It was found that the built-in strain narrowed the spectral line width of individual nanostructures and was responsible for the high spectral purity observed in ensemble.

Chapter 4 demonstrates the development of environmentally friendly thick shell InP-ZnSe core-shell QD structures as ’greener’ alternatives to prototypical CdSe-based QDs. Optical spectroscopy on individual InP nanostructures showed that blinking of the PL can be strongly suppressed—attributable to the presence of the large uniform shell—improving their PL efficiency. However, the optical measurements also revealed variable levels of blinking suppression between individual QDs. Structural characterization of the sample uncovered morphological defects in the shell of a subpopulation of QDs, pinpointing a potential structural factor that limited the performance of the material. These results suggest that future endeavors to directly correlate the structural and optical properties of individual InP QDs should provide valuable feedback to further advance the development of the non-toxic materials.

Chapter 5 detail the use of the correlation strategy outlined in Chapter 2 to establish such detailed structure-property relationships at the single QD scale. Applied to quantum-dot-in-rod nanostructures, this correlation enabled the identification of surface roughness as a crucial structural aspect to consider when engineering QDs with specific excited state outcomes.

Finally, Chapter 6 concludes the work presented in this dissertation and additionally offers perspective on possible future directions based on the findings and conclusions of these studies.

Chapter 2

Single QD Experimental Methods

2.1 Implementation of the Single Quantum Dot Optical Microscope

Investigation of the optical properties of single QDs requires instrumentation which enables the resolution of individual nanostructures, allows for efficient excitation and light collection and provides access to processes occurring at fast time scales. A schematic of the experimental setup used in this work and modified from Dukes *et al.*[49] is shown in Figure 2.1.

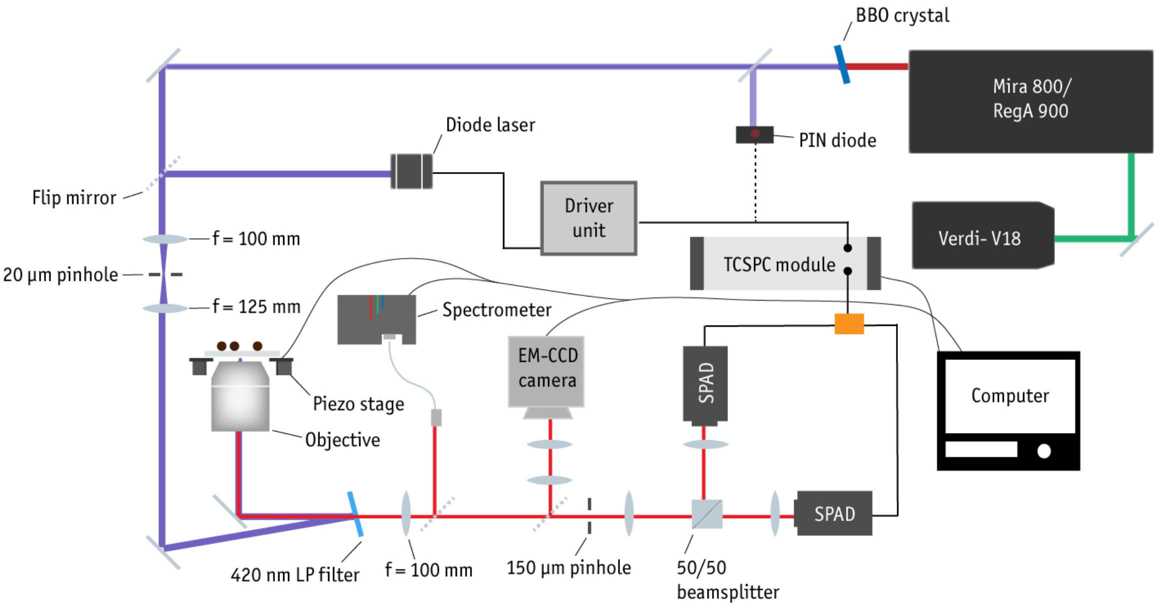

Figure 2.1: Setup of single QD optical microscope. A set of lasers are used to provide a suitable excitation beam that is directed to an objective to illuminate the sample. Fluorescence from the QDs is collected by the same objective, filtered to remove any residual excitation light, and the emitted light stream processed by a pair of single photon avalanche diodes (SPADs) configured in a Hanbury-Brown and Twiss geometry. Additionally, the emission can be directed to a CDD camera for wide-field imaging of the sample or a spectrometer for spectral dispersion. See text for a full description of the setup and optical components.

The primary excitation source is a turnkey pulsed diode laser (Picoquant, LDH-D-C-405) producing pulses < 100 ps in duration at a wavelength of 405 nm, suitable for excitation of visible and near-IR emitting QD nanostructures. The repetition rate is tunable from 31.25 KHz to 80 MHz using a stand-alone control driver (Picoquant, PDL 800-D). This provides a wide range of pulse-to-pulse (2.5 ns - 32 μs) separations that readily extends the typical relaxation times of QD nanostructures. It is also possible to use the PDL driver to operate the diode laser in continuous-wave (cw) mode. Average power outputs of the diode laser are in the mW range.

Additional excitation sources are provided by an ultrafast laser system (Coherent$^{\text{TM}}$). A neodymium-doped yttrium orthovanadate (Nd:YVO_4) cw laser (Coherent$^{\text{TM}}$ Verdi, 532 nm, 18W) pumps a 800 nm Ti:Sapphire ($\text{Ti:Al}_2\text{O}_3$) oscillator (Coherent$^{\text{TM}}$ Mira Basic 800) with a repetition rate of 76 MHz. The output from the Mira is focused onto a frequency doubling beta barium borate (1 mm β-BBO, Altos Photonics) nonlinear mixing crystal, (angle-tuned for efficiency) to produce a 400 nm beam. Alternatively, the output from the Mira is used to seed a Ti:Sapphire ($\text{Ti:Al}_2\text{O}_3$) regenerative amplifier (Coherent$^{\text{TM}}$ RegA 900). The energy of the 800 nm pulses from the RegA is amplified by a factor of $\sim 10^3$ and the repetition rate of the pulses is lowered to 250 KHz. The RegaA output is frequency doubled using a β-BBO nonlinear crystal to generate a 400 nm beam. Both outputs from the Mira and Rega feature pulses of < 200 fs in duration and enable dynamics occurring on very short time-scales, down to a few ps to be extracted from lifetime measurements.

Either excitation source is focused through a 20 μm pinhole to spatially filter the beam before being re-collimated and passed through a motorized shutter, used to block excitation prior to data collection. The beam is reflected from a 420 nm long pass (LP) dichroic filter (Omega Optics, 3RD420LP, angle-tuned to maximize transmission at 420 nm) into an inverted objective (Olympus UPLSAPO, apochromatic, water immersion, 1.2 N.A., 60x, FN 26.5, WD 0.28, ∞/0.13-0.21) and brought into focus at the sample. A variable neutral density (ND), can be inserted into the beam path to attenuate and control the laser power at the sample. Focusing is achieved using a cantilevered 3-axis piezoelectric scanning stage (Thorlabs Inc., NanoMax, MAX303) interfaced with a piezocontroller (Thorlabs Inc., BPC203) to adjust the high of the sample. Fluorescence from the sample is collected by the same objective and the resulting collimated beam passes through the dichroic filter and also through a 450 nm LP filter (Omega Optics, 3RD450LP) to remove any residual scattered or reflected excitation light.

The fluorescence beam is focused through a 150 μm pinhole and directed to a Hanbury Brown-Twiss interferometer. This setup was realized using a 50/50 non-polarizing beamsplitter cube and two single photon avalanche photodiodes (SPAD, Micro Photon Devices, $PD-050-0TC) configured so that half of the emitted photons is collected by each SPAD. The TTL output of the two SPADs are connected to a time-correlated single photon counting module with a time resolution of 4 ps (Picoquant, Picoharp 300) using an external router (Picoquant, PHR 403). The electrical trigger (reference signal) for the Picoharp is provided by the synchronization output of the driver of the diode laser. Alternatively, if the output from the Mira or Rega is in use, a small portion of the beam is sent to a PIN photodiode (Picoquant, TDA 200) used to generate the electrical trigger pulses. The overall timing resolution of the system is approximately 34 ps. Flip mirrors inserted into the beam path before the 150 μm pinhole can be used to direct the fluorescence beam to a spectrometer (Ocean Optics, QE, 600 l/mm) equipped with a thermoelectric-cooled Hamamatsu, back-illuminated charge-coupled device (CCD) to disperse fluorescence in the spectral dimension. The Flip mirrors can also direct the fluorescence to facilitate imaging onto an electron multiplying (EM) CCD camera (EM-CCD, Andor iXonEM+, DU-897E-CSO-#BV).

The spatial resolution of the imaging setup was determined by imaging the fluorescence from a single QD on a glass coverslip. The theoretical Rayleigh resolution (defined by $0.61\lambda/\mathrm{N.A.}$) of the system is 200 nm, when using an excitation wavelength of $\lambda = 405$ nm and a numerical aperture N.A. = 1.2. In practice, however, the spatial resolution of the instrument was found to be less than the theoretical limit with a full-width at half-maximum

(FWHM) of the the point spread function (PSF) of approximately 400 nm.

For wide-field excitation, a Kohler illumination lens (f = 300 mm) is inserted into the path of the laser before the dichroic filter. The Köhler lens focuses the beam to a point just behind the microscope objective, so that the objective approximately recollimates the beam at the sample to illuminate a large field of view ($\sim$100 μm beam diameter). In this configuration, the CCD camera is used to monitor the detection area. For imaging purposes the CCD array is typically thermo-electrically cooled to -50 ^{o}C or less to reduce noise from dark currents.

2.1.1 Principle of Time Correlated Single-Photon Counting

Time correlated single photon counting is a measurement technique that provides the time resolution necessary to examine single QD emission after excitation. The technique measures the time between an excitation event and subsequent emission of single photons. Over time, many of these times are collected for the sample under investigation. The delay times can then be binned to construct a histogram representative of the decay profile of the emitter(s). This time decay provides an estimate of characteristic lifetimes. In practice, TCSPC requires a highly repetitive light source to accumulate a sufficient number of time delays for an accurate representation of the dynamics of the emission process. The technique allows measurement of emission dynamics on pico- to micro-second timescales.

For a typical TCSPC setup, a high repetition pulsed source (e.g. laser, LED) is used for excitation and also provides the reference signal for the measurement of photon arrival times. Following excitation, a single-photon detector (e.g. SPAD) registers single photons emitted by the sample. The elapsed time T_1 between an excitation and photon detection event is recorded using standard TCSPC timing electronics (e.g. Picoharp 300). In practice, the probability of registering more than one photon per excitation cycle is kept low so that many cycles pass before the detection of a second photon event T_2. In order to meet this condition, the count rate at the detector is limited to at most 1 to 2% of the excitation rate

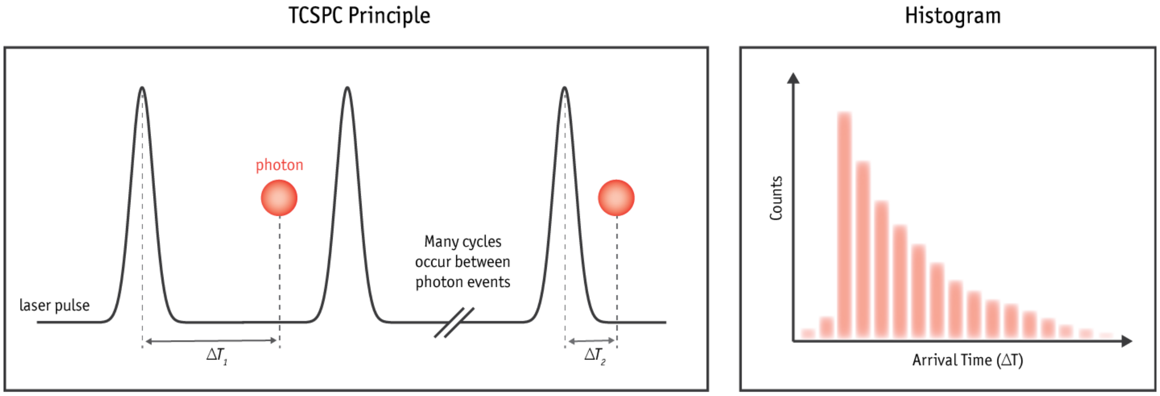

Figure 2.2: Time-Correlated Single Photon Counting Principle. (*Left*) A QD emitter is repeatedly excited by a pulsed laser and each single photon emission event detected by a SPAD. The elasped time (ΔT) between an excitation and photon emission event is measured using TCSPC timing electronics (e.g. Picoharp 300). In the single photon regime, many pulse cycles pass without registration of a photon event. (*Right*) A histogram of photon arrival times is built up over many excitation-emission events. The profile and rate constants (lifetime) of the decay provide insight into the exciton relaxation dynamics of the QD nanostructure.

and prevent pile-up effects in the histogram of arrival times. The time card registers each photon event and tags it in time relative to the last excitation pulse—typically resolved down to a few picoseconds. After the collection of a sufficient number of photon events, a histogram of the measured arrival times is constructed; this histogram can then be used to determine the lifetime of the QD emitter under investigation and to examine processes influencing exciton relaxation. The measurement process is demonstrated in Figure 2.2.

2.1.2 Photon Correlation

TCSPC modules are additionally suitable for measuring time correlations in the photon stream of individual QD nanostructures. These photon correlation studies are typically realized using two single-photon detectors configured in a Hanbury Brown-Twiss interferometric geometry.[50] In this setup, emitted photons are sent to one of the two single-photon detectors on either side of a 50/50 beam-splitter with equal likelihood and the elapsed time τ between consecutive pairs of photons recorded. Once a sufficient number of photons has been detected, a histogram of the photon-pair separation times is built up (under pulsed excitation). This histogram can be described by the second-order correlation function, $g^{(2)}(\tau)$, of photon counts between the two detectors, given by:[51]

$$g^{(2)}(\tau) = \frac{\langle n_1(t) n_2(t+\tau)\rangle}{\langle n_1(t)\rangle\langle n_2(t+\tau)\rangle}, \tag{2.1}$$

where $n_i(t)$ is the number of photon counts registered on detector i at time t. In essence, $g^{(2)}(\tau)$ is proportional to the conditional probability of detecting a second photon at some time $t+\tau$, given that a photon was detected at time t.

2.1.2.1 Photon Antibunching

The second-order correlation function is often used to classify the nature of an emitter. For a single photon emitter, as $\tau \to 0$, if $n_1(t) \neq 0$, then $n_2(t+\tau) \approx n_2(t) = 0$. Conversely, if $n_2(t+\tau) \neq 0$, then $n_1(t) = 0$. This means that if a single photon is detected as a result of excitation by a single laser pulse, it is impossible for a single photon emitter to generate another photon that could be registered simultaneously on a second detector. This leads to a lack of correlation counts between the two detectors at zero time delay. Therefore, as the time delay τ approaches zero, the second order correlation function also goes to zero:

$$\lim_{\tau\to 0} g^{(2)}(\tau) \to 0 \tag{2.2}$$

This behavior of $g^{(2)}(\tau)$ is a signature of photon antibunching and results from the fact that a single emitter can only emit one photon at a time. Under pulsed excitation photon antibunching produces a $g^{(2)}(\tau)$ trace similar to the one shown in Figure 2.3. The dip in the counts of the center peak at zero time delay demonstrates that the single emitter cannot emit two photons following excitation by a single pulse. Antibunching can therefore provide a sort of litmus test for the presence of a single QD. The observation of the antibunching effect in QDs also demonstrates that single QDs indeed can act as artificial atoms.[50]

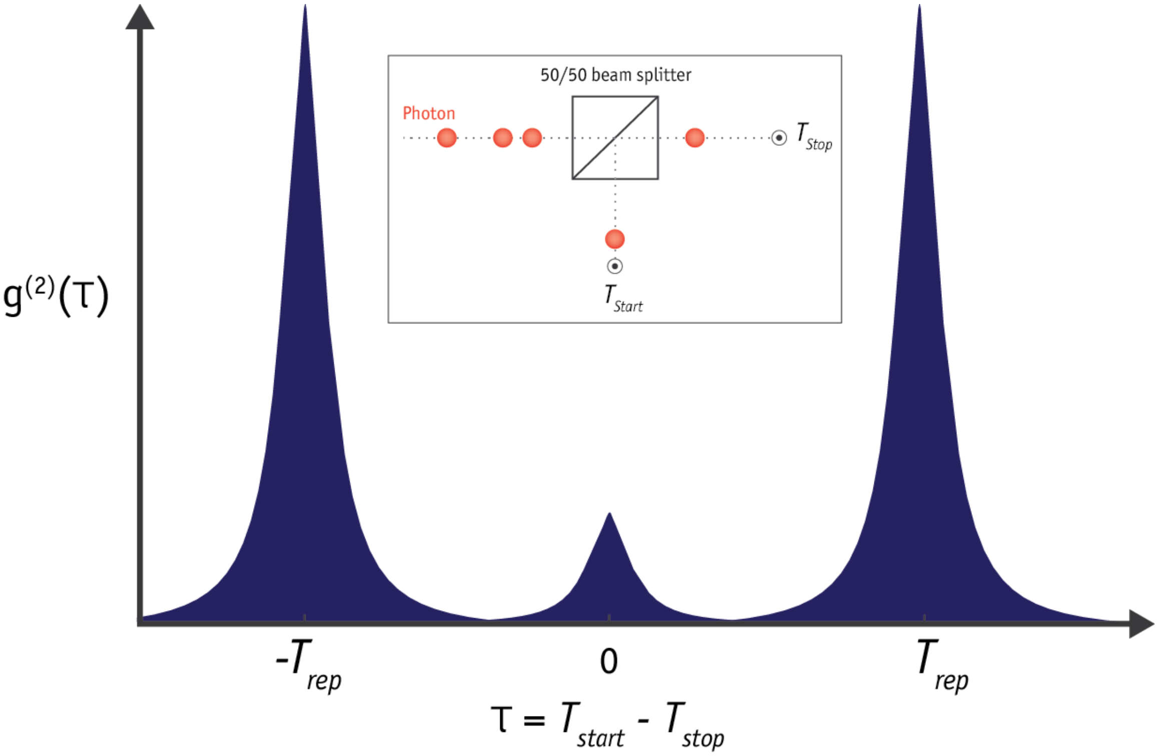

Figure 2.3: Illustration of second-order photon correlation ($g^{(2)}(\tau)$) measurement for a single QD. Inset: Schematic of Hanbury Brown-Twiss dual-detector setup used to register separation times between pairs of photons. Under pulsed excitation, the $g^{(2)}$ trace is made up of a series of individual peaks. Side peaks ($\tau = \pm T_{rep}$) correspond to photon pairs from separate excitation pulses, where as the central feature ($\tau = 0$) originate from the arrival of photon pairs following excitation by a single pulse. For a single photon emitter, the amplitude of this central peak is close to zero, demonstrating photon antibunching. However this peak can be non-zero in QDs due to emission from multiexcitons. In the limit of weak excitation intensities, the ratio of the areas under the center and side peaks approximately gives the biexciton quantum yield.

2.1.2.2 Biexciton Quantum Yield

Although the $g^{(2)}(\tau)$ signal is often used to distinguish individual QDs from multiple emitters, single QD nanostructures rarely show complete antibunching ($g^{(2)}(\tau \to 0) = 0$). For instance, it has been shown that the ratio of the integrated areas of the center and side peaks of the $g^{(2)}$ trace for a QD nanostructure typically has a finite value (Figure 2.3). This occurrence arises due to the ability of single QDs to support multiexcitons, created when the QD absorbs multiple photons (N) from the same excitation pulse. In the limit of low excitation intensity (when $\langle N \rangle \ll 1$), biexcitons (two electron-hole pairs) dominate. In QDs, biexcitons typically recombine non-radiatively, but a subset of generated biexcitons may undergo radiative recombination. When a biexciton recombines radiatively, two photons are promptly emitted one after the other. Biexciton emission events are therefore registered as photon pairs originating from the same excitation pulse and are responsible for the peak at zero time delay ($\tau = 0$) in the photon-correlation trace.

Furthermore, it can be shown that the ratio of the integrated areas of the center and side peaks, $g_0^{(2)}$, is quantitatively related to the biexciton quantum yield (BX QY):[39]

$$g_0^{(2)} \equiv \frac{\int_{-\Delta t}^{\Delta t} g^2(\tau) d\tau}{\int_{t_{rep}-\Delta t}^{t_{rep}+\Delta t} g^2(\tau) d\tau} \approx \frac{\eta_{BX}}{\eta_X} \tag{2.3}$$

where η_{BX} and η_X are the biexciton and single exciton quantum yields, respectively. Therefore, the $g^{(2)}(\tau)$ measurements additionally permit direct access to study the recombination processes of biexcitons in single QDs.

2.2 Implementation of Correlated Measurement of the Atomic Structure and Photoluminescence of the Same Quantum Dot

2.2.1 Sample Preparation

For a typical correlation sample preparation, polystyrene latex microspheres (Ted Pella, No. 610-38, 1μm) dispersed in aqueous solvent are dropcast onto a TEM substrate (Ted Pella, PELCO Ultra-Flat -8 nm- Silicon Dioxide Support Film). The substrate consist a flat 8 nm thick silicon dioxide (SiO_2) support film, grown on top a silicon wafer and overlaid with a silicon nitride (Si_3N_4) mesh to form several grid windows. For examination of the same QD nanostructures in both an optical and electron microscope, the choice of substrate is of great importance. An appropriate substrate should be transparent to both light and an intensely focused electron beam. In addition, it should also show minimal fluorescence at the photoluminescence wavelengths of the structures under investigation and should not quench their emission. The SiO_2 support films are well suited for this purpose. Furthermore, although SiO_2 is an electrically insulating material, the ultra-thin support films show minimal charging effects when imaging in an electron microscope. Upon deposition, the polystyrene beads naturally group together into distinctive patterns that are easily discernible when imaging with a fluorescence or electron microscope. Figure 2.4 shows an example TEM micrograph of the unique assemblies of the polystyrene beads that result when cast on the TEM support films. After the deposition of the polystyrene markers, a dilute solution of nanocrystals ($\sim$ 1 nM) dispersed in common organic solvent such as hexanes or toluene is dropcast onto the support film and allowed to dry. The prepared TEM substrate is then stored and transported in a grid holder.

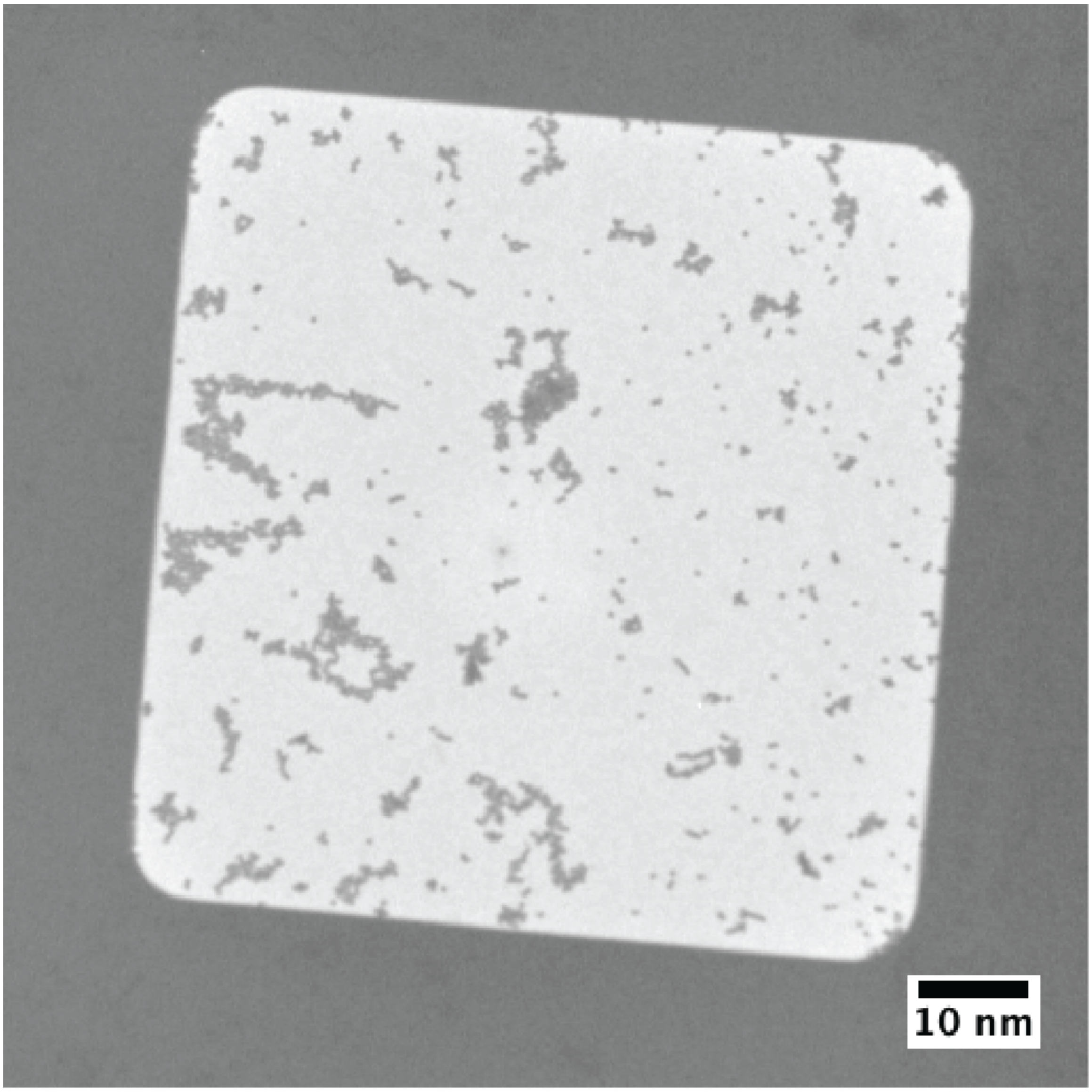

Figure 2.4: Transmission electron micrograph of polystyrene beads deposited on a SiO_2 support film. The beads randomly group together to form a sparse collection of features with unique shapes, orientation and connectivity. These formations allow different regions of the substrate to be readily identified.

2.2.2 Correlation Strategy

Figure 2.5 illustrates the general approach for the correlation of single QD optical behavior with atomic structure. The polystyrene patterns serve as placement beacons to facilitate instrument relocation and fast and precise localization of the same QD structures. The simple approach for the collection of fluorescence and atomic structural information from the same nanostructures is illustrated in Figure 2.6. This strategy can be implemented using widely available instrumentation without modifications to the optical or electron microscope.

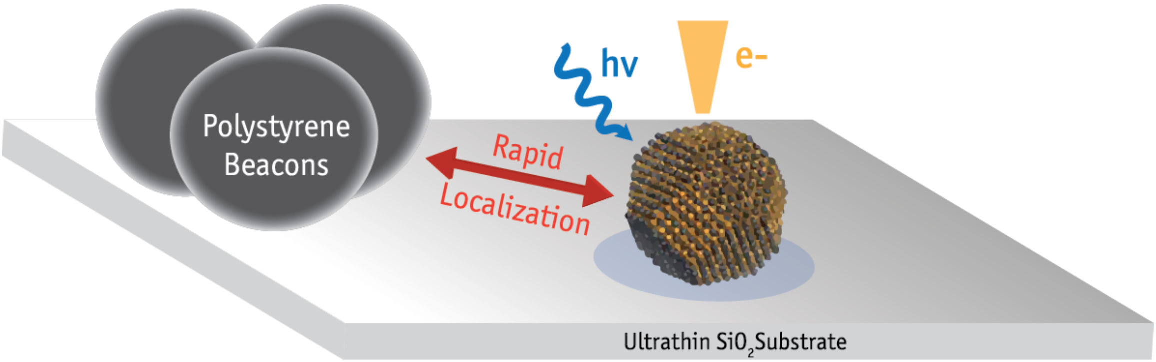

Figure 2.5: A simple, general approach to correlate single QD optical behavior with atomic structure. Polystyrene beacons enable fast and accurate localization of QD structures

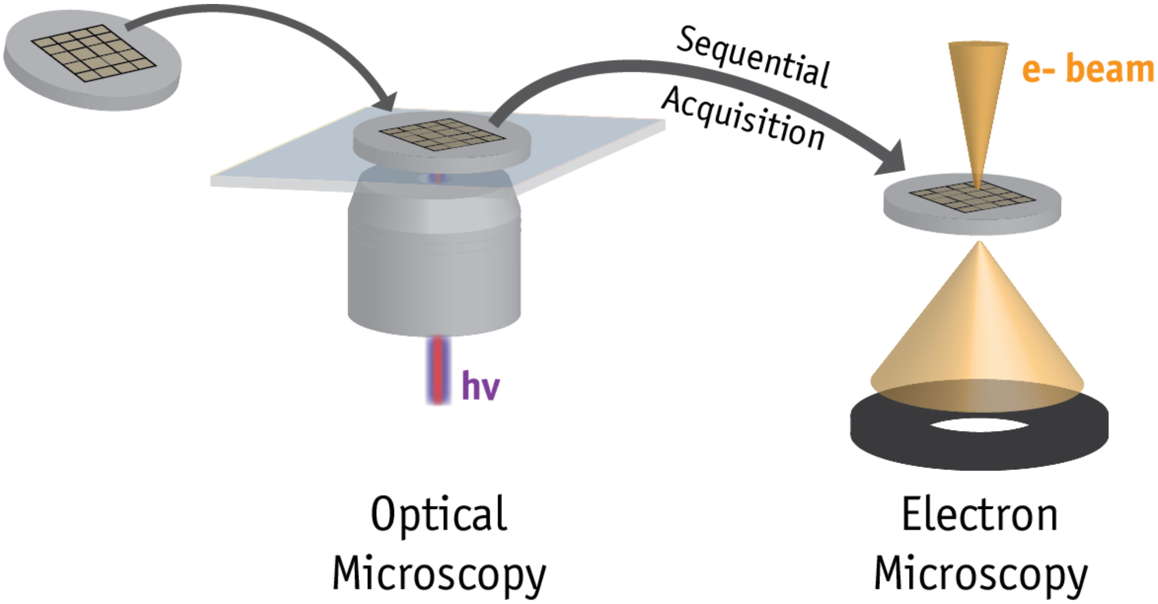

Figure 2.6: Overview of the correlation workflow. A low density of QDs is deposited on a TEM SiO_2 support grid with polystyrene placement markers to facilitate instrument relocation and rapid acquisition of optical and structural data from the same nanostructure. The grid is first positioned for optical imaging in a fluorescence microscope then relocated and imaged in an electron microscope.

2.2.3 Optical Microscopy

For single QD optical spectroscopy, the support film is placed on a glass coverslip and mounted onto the custom-built inverted fluorescence microscope described in Section 2.1. The support film is then centered over the objective using the adjustments of the piezo stage. In order to bring the image of the sample into focus the piezo stage is adjusted so that the laser beam is focused at the coverslip and is also partly reflected back along the incident path. In the fluorescence microscope, residual fluorescence from individual polystyrene microspheres provides the requisite signal to resolve their formations. Fluorescence imaging of the sample is done using wide-field Köhler illumination.

An example wide-field fluorescence image of a correlation sample recorded on the CCD array is shown in Figure 2.7. Large fluorescent features correspond to polystyrene assemblies and are easily distinguished from localized spots resulting from single QD fluorescence. The polystyrene beads are used to map positional information for identifying the same QDs in the electron microscope.

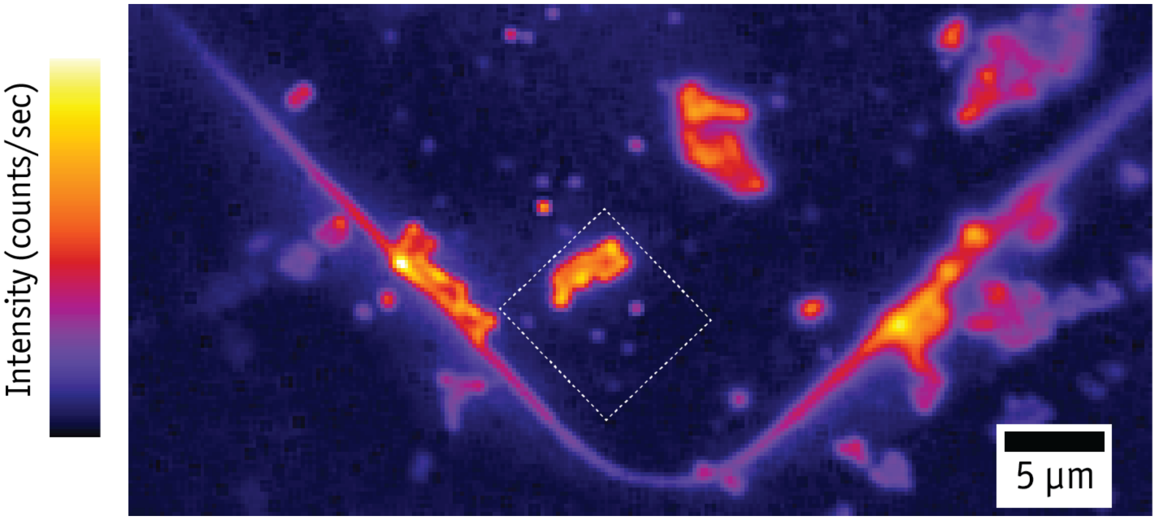

Figure 2.7: Wide-field fluorescence imaging of single QDs on a SiO_2 support film preloaded with polystyrene beacons. The image is constructed from the fluorescence maximum of each pixel over a 5 minute period. Large fluorescent features correspond to polystyrene assemblies and are easily distinguished from localized spots resulting from single QD emission.

2.2.4 Electron Microscopy

Subsequent to fluorescence imaging and collection of optical information from individual QD nanostructures, correlation samples are imaged in an electron microscope to retrieve atomic level structural information from the same QDs. Electron micrographs are acquired using a Tecnai Osiris electron microscope, typically operating at 200 kV, with a tunable beam current chosen to reduce potential charging effects. Imaging of the sample is primarily carried out in HAADF-STEM mode. Higher imaging contrast in HAADF-STEM compared to HRTEM better facilitates the localization of individual QDs at low imaging magnifications. The polystyrene landmarks deposited on the substrate are used to orient the sample in the electron microscope and to locate areas of interest.

Figure 2.8 shows a scanning transmission electron micrograph of the same area of the support film outlined in Figure 2.7. The unique assembly and distribution of the polystyrene beacons on the SiO_2 substrate were used to align and orient the correlation grid and to close in on the region of interest. The same QDs detected during fluorescence imaging are readily identifiable and are enclosed in red circles. This demonstrate the ease and high specificity of the technique. Additionally, the method is uniquely situated to identify non-emissive or "dark" structures that do no show up in fluorescence imaging, two of which are denoted by white circles in Figure 2.8.

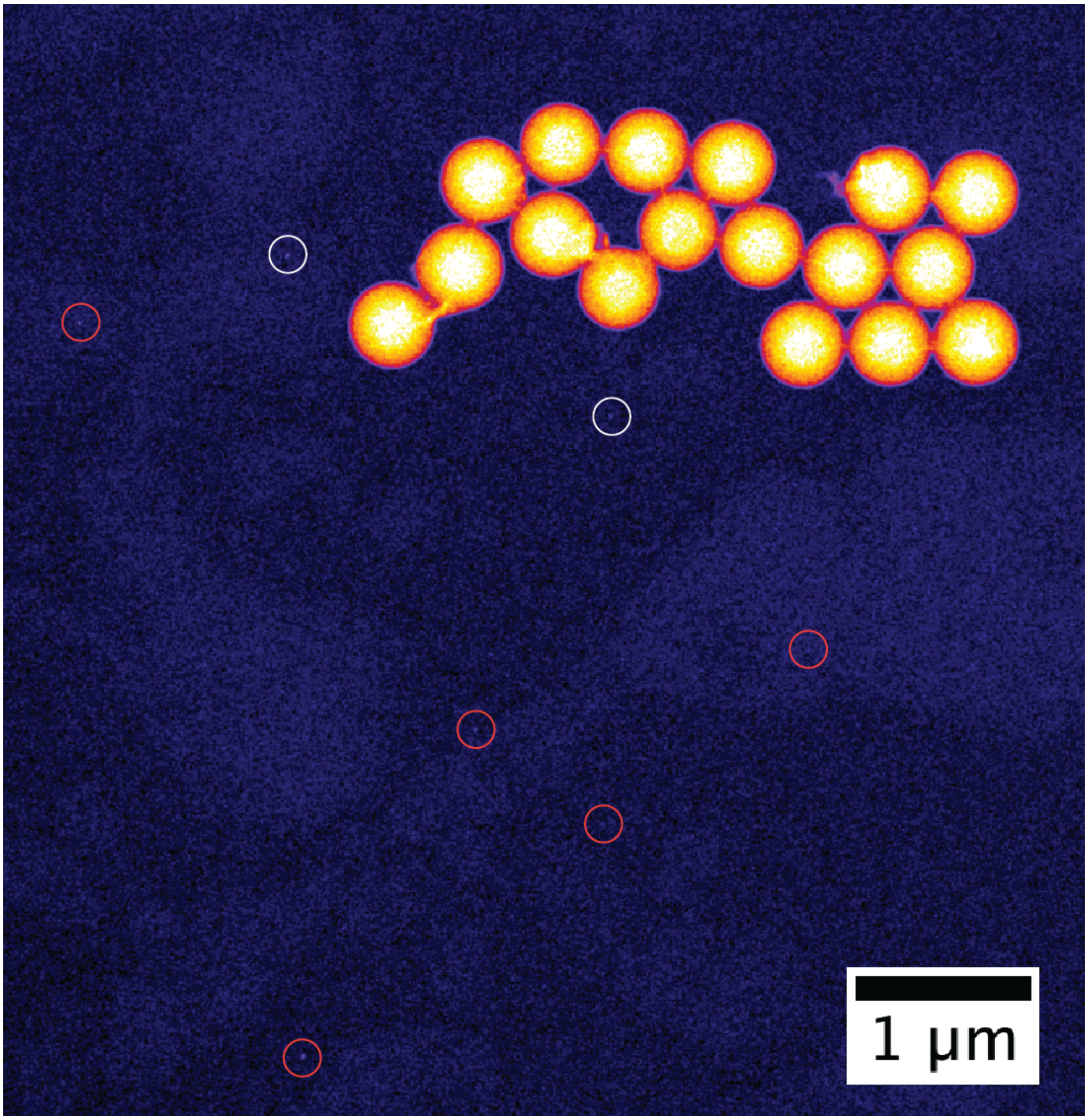

Figure 2.8: Localization of the same single QDs in an electron microscope. Scanning transmission electron micrograph of the highlighted area of the support film in Figure 2.7. Red circles denote the location of the fluorescing QDs. Non-emissive "dark" QDs are enclosed in white circles.

Chapter 3

Spectroscopy of Single Biaxially Strained Colloidal Quantum Dots[1]

3.1 Introduction

Colloidal quantum dot (QDs) are solution-processed semiconductor nanomaterials whose photophysical properties not only depend on their material composition but also their physical structure. As a result, QDs present remarkable opportunities to engineer materials tailored for a diverse range of optical applications. In addition to size- and shape-dependent optical and electronic properties,[52] QDs can be made with high quantum yields[53] and photo-stability.[54] Combined with the ability to process them from solution, QDs are of interest for incorporation into light-emitting devices,[55] displays,[7] biological imaging,[8] lasers[56] and photon sources for quantum technologies.[57] Despite their potential, for applications such as displays and biological multiplexing that require high spectral purity, as synthesized photoluminescence line widths of individual QDs (homogeneously broadened) remain sufficiently broad, thereby limiting optimal performance.

One factor that influences the emission line width of single QDs is that the band-edge exciton (lowest energy electron-hole pair) can comprise multiple electronic states.[58] For example, in CdSe QDs the band-edge exciton is spread among eight states at room temperature, several of which are optically active.[59] Therefore the room temperature photoluminescence is expected to exhibit contributions from multiple emissive states. For this reason Fan *et al.* experimented with the application of strain as a means of increasing the splitting the band-edge transitions to tighten the emission line width of QDs.[6] Strain provides a unique opportunity to control the properties of QDs and contribute an

---

[1] Adapted with permission from Fan, F.; Voznyy, O.; Sabatini, R. P.; Bicanic, K. T.; Adachi, M. M.; McBride, J. R.; Reid, K. R.; Park, Y.-S.; Li, X.; Jain, A.; Quintero- Bermudez, R.; Saravanapavanantham, M.; Liu, M.; Korkusinski, M.; Hawrylak, P.; Klimov, V. I.; Rosenthal, S. J.; Hoogland, S.; Sargent, E. H. “Continuous-Wave Lasing in Colloidal Quantum Dot Solids Enabled by Facet-Selective Epitaxy” Nature 2017, 544, 75-79. Nature Publishing Group.

additional modality to existing paradigms such as size, shape and band structure engineering through heterostructuring.[60] Interestingly, by engineering QD nanostructures with a built-in anisotropic biaxial strain, Fan *et al.* achieved narrower ensemble photoluminescence line widths compared to QDs synthesized by other methods. However, it was unclear whether the improvement resulted from narrower single QD lineshapes due to changes to the exciton electronic structure; or from a high structural uniformity—due to the developed synthesis procedure—which minimizes sources of inhomogeneous broadening.

As mentioned in Chapter 1, single QD spectroscopy is a vital tool for studying the behavior of QDs. By investigating QDs one at a time, both the intrinsic properties of individual nanocrystals and the effects of structural heterogeneity can be probed, thereby enabling a deeper understanding of the photophysics of QDs.[16] Here, single QD fluorescence spectroscopy is used to investigate the optical properties of individual biaxially strained QDs and to explore the structural origin of the narrow emission. Specifically, photoluminescence line width measurements were carried out on individual biaxially strained QD nanostructures and compared to conventional QDs in which a uniform strain is applied. In addition the blinking behavior and multiexciton recombination efficiency of the biaxially strained structures are examined.

3.2 Biaxially Strained QD Nanostructures

In order to arrive at QD nanostructures with the desired built-in anisotropic strain, a two-step facet-selective epitaxy scheme was employed to grow core-shell heterostructures with an asymmetric compressive shell. This approach takes advantage of the varying reactivities of the crystal facets at the complex surfaces of QDs.[61] Starting with inherently prolate wurtzite CdSe cores, a combination of shell precursors and surfactants were used to coordinate the growth of an asymmetric CdS shell in an oblate shape (see Methods for details). A second uniform shell growth step was necessary to fully passivate the CdSe core and to increase the photoluminescence quantum yield above 90%.

Figure 3.1 a shows a high-angle annular dark-field scanning transmission electron microscopy (HAADF-STEM) image overlaid with an energy dispersive X-ray spectroscopy (EDS) chemical map of the core-shell QDs which clearly depicts the asymmetric coverage of the shell. The chemical maps also reveal that the CdSe cores are off-centered inside the oblate CdSe shell but remain passivated on all sides. The lattice mismatch between CdSe and CdS (3.9%)[62] induces a compressive pressure on the CdSe core. In the case of the asymmetric QD heterostructures, this strain is anisotropic and is applied in the two directions perpendicular to the main crystallographic axis (*c*-axis) of the CdSe core. Figure 3.1b shows a high-resolution transmission electron microscopy (HRTEM) micrograph of one of the asymmetric core-shell structures oriented on edge and viewed along the $[12\bar{3}0]$ zone axis. Visible bending of the crystal lattice on one (right) side of the nanocrystal and in the region of the CdSe core is a key signature of lattice strain. Mapping the displacement of the local lattice in the direction of the *c*-axis (x-direction) shows stronger deviation from the underlying CdS, approaching undistorted CdSe, implying that the strain along this axis has been released. However, in the perpendicular direction (y-direction) the lattice spacing remains closer to CdS, indicating stronger compression of the CdSe core, confirming the hypothesized biaxial strain.

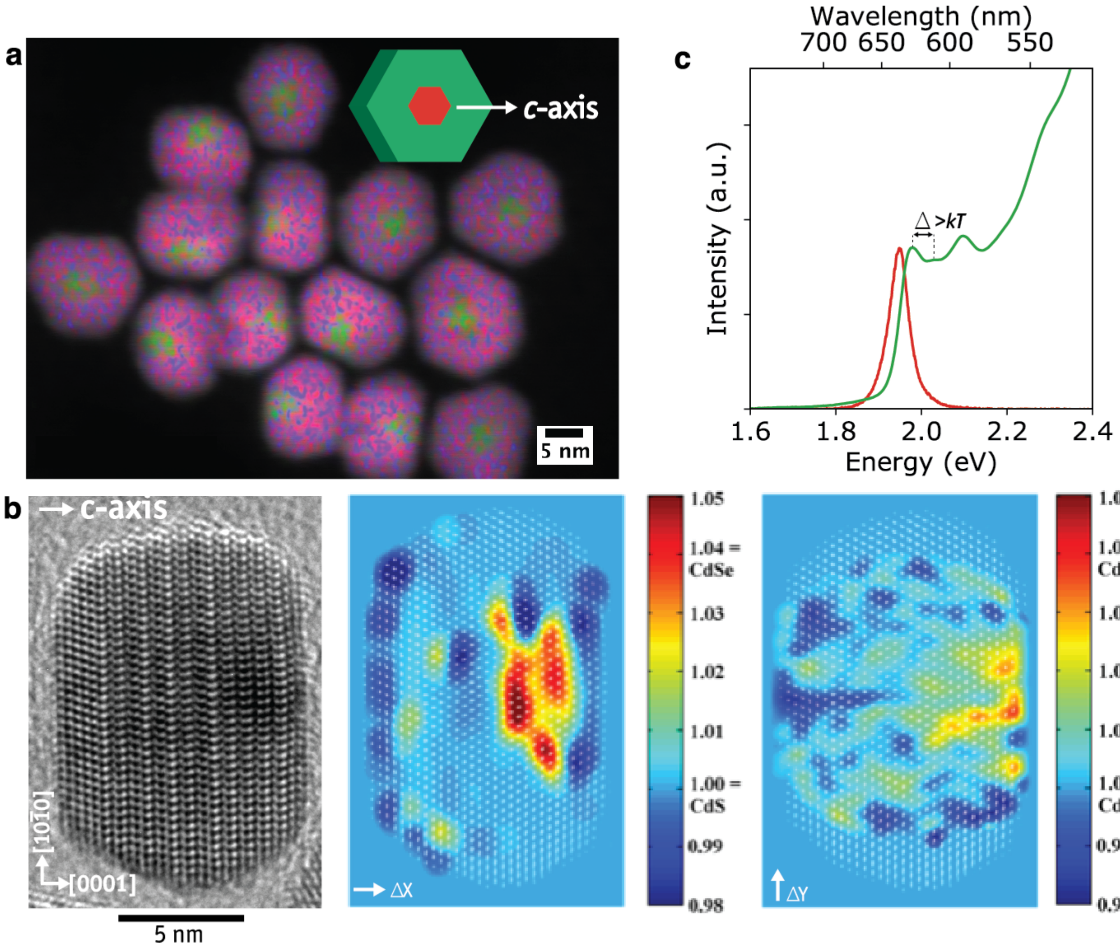

Figure 3.1: Structural, chemical and optical characterization of biaxially strained QD sample. (a) STEM-EDS chemical map of the asymmetric CdSe-CdS core-shell QD nanostructures. (b) High-resolution TEM micrograph of a biaxially strained QD (*left*) and corresponding local lattice constant mapping (*right*) indicating the built-in biaxial strain. (c) Absorption (green) and photoluminescence (red) spectra of the biaxially strained QDs. Δ represents the energy splitting of the first exciton peak and kT denotes the thermal energy at room temperature.

Absorption and photoluminescence spectra of a sample of the biaxially strained QDs are presented in Figure 3.1c. The lowest energy absorption peak, corresponding to transitions at the band-edge of CdSe is split into two. In the effective mass approximation, this splitting, denoted as Δ, is $\sim$ 55 meV and separates the heavy and light hole valence bands within the first exciton manifold.[58] In contrast, for conventional symmetric CdSe-CdS QDs in which strain is uniformly applied to the CdSe core (i.e. hydrostatic strain), Δ is comparable to the thermal energy ($kT \sim$ 25 meV) at room temperature. The additional splitting of the states at the band-edge of the biaxially strained QDs is therefore attributed to the anisotropic pressure of the CdS shell on the CdSe cores which induces a deformation potential that is felt differently by heavy and light hole states.[63] The biaxially strained QDs also exhibit exceptionally narrow ensemble PL line width (full-width at half-maximum (FWHM) of 54 meV, ($\sim$ 17 nm)) at room temperature. This represents a higher spectral purity compared to the narrowest lineshape observed for conventional core-shell QD structures (63 meV, ($\sim$ 20 nm)).[53]

3.3 Optical Spectroscopy of Individual Nanostructures

3.3.1 Role of Strain on Single QD Spectral Line Width

To further characterize the biaxially strained QDs and explore the origin of the narrow ensemble emission, single QD photoluminescence measurements were carried out on individual nanostructures (see Methods for details). Figures 3.2a,b shows representative room temperature photoluminescence spectra of single biaxially strained and conventional hydro-statically strained QDs (grown with the same size CdSe cores and similar QD volume (see Methods)) fit to a Lorentzian function. A short integration time (50 ms) and low excitation intensities (5-10 W/cm^{-2}) were used to minimize the influence of spectral wandering on the lineshape of the QDs.[33] Remarkably, the average extracted homogeneous single QD FWHM for biaxially strained nanostructures (33 $\pm$ 4 meV ($\sim$ 10 nm)) is twice as narrow as the single QD spectral width for conventional QDs (62 $\pm$ 8 meV ($\sim$ 20 nm)) (Figure 3.2c,d). This two-fold reduction of the single QD line width in biaxially strained structures can be explained by the increased splitting of the band-edge exciton states (in excess of the thermal energy) due to the built-in anisotropic pressure on the CdSe core. As a result, emission originates from the energy levels nearest the band-edge of the QDs.

The single QD spectral investigation also indicate that the narrow single particle lineshapes are responsible for the narrow photoluminescence peak of the biaxially strained

QDs in ensemble. Even so, the ensemble spectrum is still more than 60% broader than the average single QD line width, indicating a notable degree of structural non-uniformity throughout the sample despite a narrow ($\sim$ 4%) size dispersion and uniform shapes. This suggests that slight variations in the morphology, chemical or surface structure of the QDs may still contribute to broadening of the ensemble line width. Additionally, it may be possible that the sample lacks a uniform distribution of the built-in biaxial strain. In any case, the single QD spectral observations highlight the sensitive nature of QD photophysics to minute structural variations and also demonstrate that the already impressive purity of the ensemble emission of the biaxially strained QDs can be further refined with improvements to the synthetic methodology.

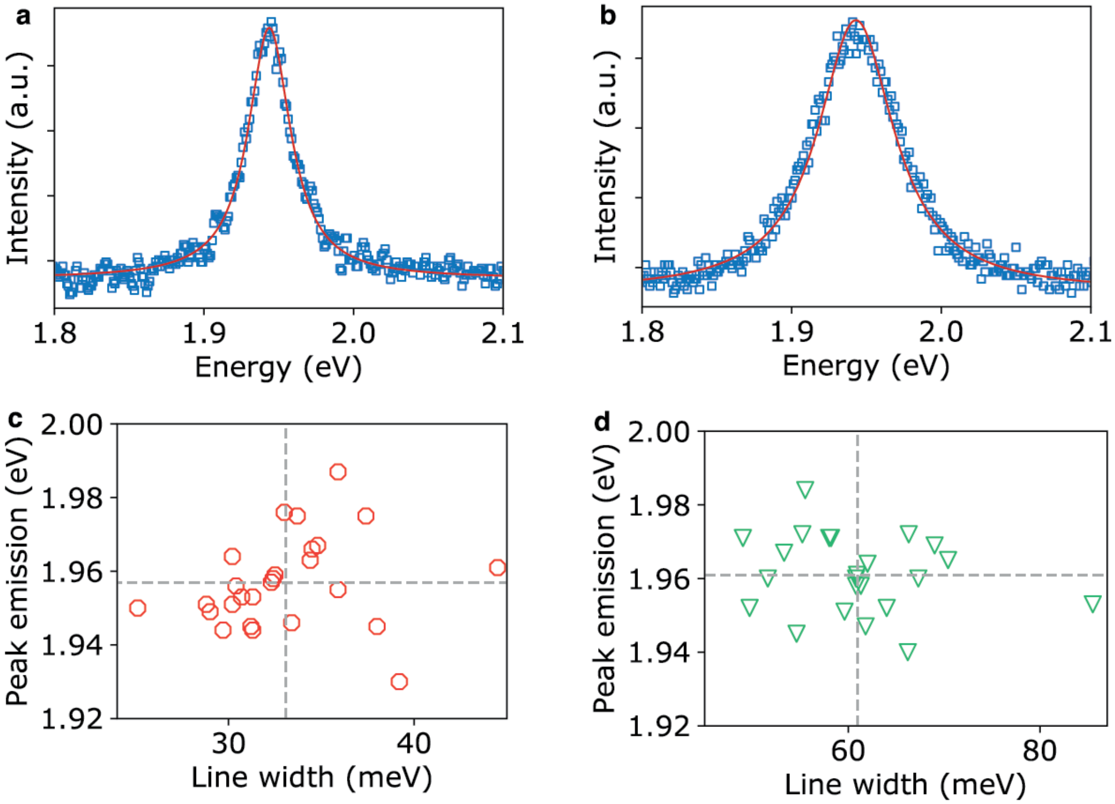

Figure 3.2: Single QD photoluminescence spectra. Photoluminescence spectra of a single biaxially (a) and hydro-statically (b) strained QD fitted to a Lorentzian function. The bin time for the single QD spectral measurements is 50 ms. (c) Distribution of the emission line width and peak position of *n*=26 single biaxially strained QDs. (d) Distribution of the emission line width and peak position of *n*=24 single biaxially strained QDs. Dashed lines indicate average line widths and peak positions.

3.3.2 Blinking Behavior

In Figure 3.3a the time-dependent evolution of the intensity of the exceptionally narrow emission from a single biaxially strained QD is presented along with a histogram of the intensity distribution. The emission is observed to randomly cycle between ’ON’ and ’OFF’ intensity periods under constant excitation. This intermittent behavior, known as blinking,[19] can be an intrinsic property of QDs and is detrimental to their use in many applications. At the ensemble level, blinking leads to sub-unity average quantum yields and darkens the photoluminescence intensity.[64] Photodarkening limits QDs as stable output sources under high flux excitation, such as in solid-state lighting. As single emitters, long blinking OFF events impede the use of QDs as probes for biological tracking and as single-photon sources in quantum optics applications. Therefore, QDs with suppressed blinking are desirable in a number of use cases.

To qualify the blinking suppression in the asymmetric QD structures the average time fraction that the QDs stay ON over the course of the measurement was retrieved from individual particles. ON and OFF periods are determined using an intensity threshold (dashed red line Figure 3.3a). This threshold was chosen as 4-6 standard deviations above the background level of the detector. The distribution of the ON time fraction extracted for 92 biaxially strained QDs is presented in Figure 3.3b. The average ON time fraction is $\sim 90\%$ with $\sim 20\%$ of the QDs displaying an ON time fraction in excess of 95%. These values support strong suppression of blinking in the asymmetric core-shell QDs and are similar to values reported for conventional CdSe-CdS QDs.[53] The high ON time fraction also indicate that surface traps typically implicated in QD blinking are well passivated in the biaxially strained heterostructures as is evident from the high photoluminescence yields in ensemble.

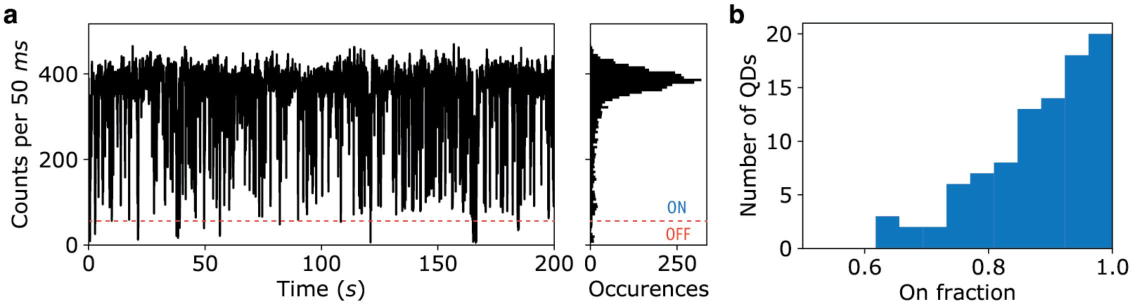

Figure 3.3: Blinking behavior of biaxially strained QDs. (a) Representative time-dependent photoluminescence intensity trace (*left*) and corresponding intensity distribution (*right*) of a single biaxially strained QD. The bin size of the intensity trace is 50 ms. The dashed red line represent the chosen threshold between ON and OFF states used to determine the ON time fraction. (b) Distribution of blinking ON time fraction (n=92).

3.3.3 Multiexciton Recombination Efficiency

The single QD measurements additionally facilitate the assessment of multiexciton recombination processes in the biaxially strained structures. Efficient multiexciton recombination in QDs is desirable in applications requiring high pump fluences (when multiexcitons are most likely to form), such as in optical amplification and lasing and as entangled photon sources for quantum technologies.[65, 66] To investigate the effect of biaxial strain on multiexciton recombination, if any, second-order photon correlation functions, $g^{(2)}(\tau)$, were acquired using a Hanbury-Brown Twiss interferometric setup to probe the recombination of biexcitons (BX)—two electron-hole pairs—in single QDs. The $g^{(2)}(\tau)$ measurements (Figure 3.4a) depict the likelihood of BX emission from a single QD following BX formation due to sequential photon absorption by a single excitation pulse.[39] When a QD emits two photons in succession after excitation by one pulse, a count is registered near the zero-time delay center peak ($\tau = 0$). Side peaks correspond to photon pairs from separate excitation pulses. The ratio of the areas under the center and side peaks is typically used to determine the biexciton quantum yield (BX QY) relative to the single exciton yield.

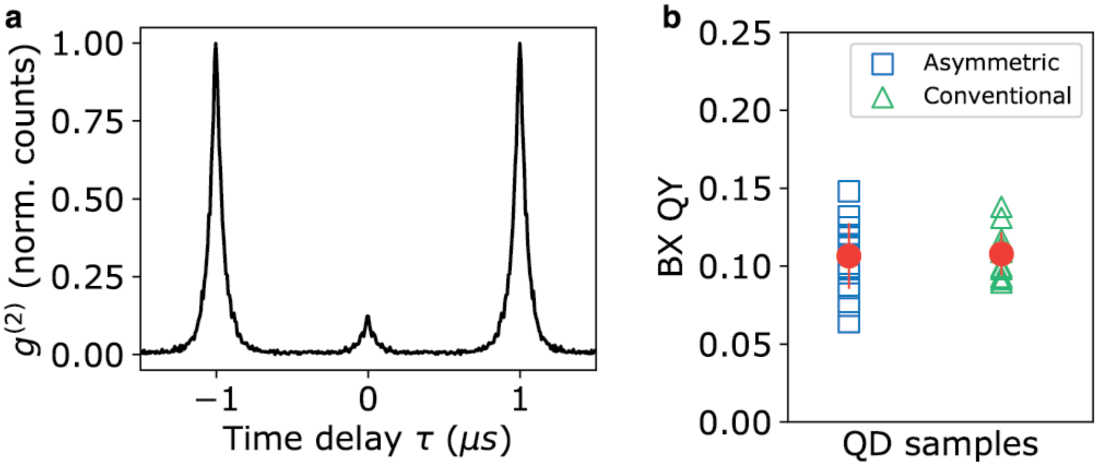

Figure 3.4: Single QD biexciton quantum yield. (a) Example $g^2(\tau)$ measurement for a single QD. (b) Biexciton quantum yield determined from $g^2(\tau)$ traces for 30 QDs. Average BX QY values are indicated by solid red circles.

The BX QY of several biaxially strained and conventional CdSe-CdS QDs calculated from their $g^{(2)}(\tau)$ function are presented in Figure 3.4b. Average estimated BX QY of the asymmetric and conventional QDs are ~ 0.10 and ~ 0.11 respectively. Factors known to correlate to BX efficiency in QDs, such as core size and QD volume were kept the same between the two QD types.[67] The similar efficiency of BX recombination in both QD samples therefore indicate that the built-in anisotropic pressure in biaxially strained does not considerably influence the likelihood of multiexciton emission. This result was expected as the built in strain should not affect the processes known to govern the efficiency of multiexciton emission.[65] Low average BX QY of the biaxially strained QDs also suggest that non-radiative decay of multiexcitons remain efficient. Interestingly, we observe an appreciable spread of the BXQY values in both biaxially strained ($\sim \pm 0.021$) and conventional QDs ($\sim \pm 0.013$). Similar QD-to-QD inhomogeneity in BX QY have been reported elsewhere[68] and is thought to reflect the sensitive nature of the processes (e.g. Auger recombination[69]) that control multiexciton efficiency to subtle changes in QD structure. In the case of the biaxially strained structures studied here, the distribution may derive from minute fluctuations in the thickness of the second passivating shell layer, heterogeneity in the passivation of the [0001] facet of the CdSe core or subtle variations in the quality and smoothness of the core-shell interface.[39, 67] Furthermore, varied BX QY among the biaxially strained QDs revealed by single QD detection suggest that their structures can be altered to optimize the emissive behavior of multiexcitons.

3.4 Conclusion

To summarize, we have studied the optical properties of single biaxially strained QDs. The built-in anisotropic strain in the core-shell QD nanostructures distorts the underlying CdSe lattice and spreads the band-edge states of the electronic structure. As a result, the QDs feature ultra narrow single QD line widths and the ensemble lineshape remains remarkably narrow. Optical spectroscopy on individual nanostructures was key in connecting the strain-induced lattice distortions to this reduction of the spectral line width. Combined with a high photoluminescence quantum yield and minimal blinking these nanostructures meet a number of important specifications for the implementation of QDs in technologies ranging from displays and solid-state lighting to biological multiplexing and tracking. In addition, although multi carrier emission efficiencies remain low and unaffected by biaxial strain, the biaxially strained QDs were found to be excellent lasing materials. Fan *et al* discovered that in addition to narrowing the emission lineshape, splitting of the band edge states alters the room temperature condition for achieving population inversion, effectively lowering optical gain thresholds in comparison to conventional QDs. In conjunction with a narrowed spectral line width, this reduced gain threshold facilitated the demonstration of steady-state lasing from a solid array of the biaxially strained QD structures.[6]

The single QD measurements further reveal significant lineshape broadening and some heterogeneity in the BX QY of the biaxially strained QDs—otherwise hidden in ensemble investigations. This variability in the optical performance of single QDs can be attributed to a level of structural non-uniformity present in the QD sample and emphasize an intimate link between QD behavior and structure. Establishing correlated structure-function relationships between single biaxially strained QDs should enable a deeper understanding of the sources of performance variations and inform further synthetic refinement of these already impressive QD nanostructures. In Chapter 5 we demonstrate the utility of a method to correlate the optical and structural properties of single QD nanostructures to establish this connection.

3.5 Experimental Methods

Materials

Cadmium oxide (CdO, > 99.99%), sulfur powder (S, > 99.5%), selenium powder (Se, > 99.99%), oleylamine (OLA, > 98% primary amine), octadecene (ODE, 90%), oleic acid (OA, 90%), tri-octylphosphine (TOP, 90%), tri-butyl phosphine (TBP, 97%), tri-octylphosphine oxide (TOPO, 99%), octadecylphosphonic acid (ODPA, 97%), 1-octanethiol (> 98.5%), thionyl chloride ($SOCl_2$), toluene (anhydrous, 99.8%), hexane (anhydrous, 95%), acetone (99.5%) and acetonitrile (anhydrous, 99.8%) were purchased from Sigma-Aldrich and used without further purification.

CdSe QD synthesis

CdSe QDs were synthesized by upscaling an existing literature procedure by 8 times.[70] QDs exhibiting an exciton peak at 590 nm were synthesized as a result of $\sim$3 min growth.

Syntheses of Cd-oleate and TOPS

2.98 g CdO was fully dissolved in 40 mL oleic acid at 170 ^{o}C under vacuum and then nitrogen to get Cd-oleate. TOPS was prepared by mixing and magnetically stirring 960 mg sulfur powder in 16 mL TOP inside the glovebox.

Biaxially strained QD synthesis

The first asymmetric shell was grown as follows: By measuring the absorbance at peak exciton (590 nm) with 1 mm path length cuvette, we quantified CdSe QDs.[71] A 5.8 mL CdSe QDs in hexane dispersion with an optical density of 1 at the exciton peak was added to a mixture of 42 mL ODE and 6 mL OLA in a 500 mL flask, and pumped in vacuum at 100 ^{o}C to evaporate hexane, then the solution was heated to 300 ^{o}C and kept for 0.5 h. As-prepared 9 mL Cd-oleate was diluted in 15 mL ODE and 3 mL TOPS in 21 mL ODE as a sulfur precursor, respectively. Cd-oleate and TOPS solutions were injected simultaneously and continuously at a rate of 6 mL/h.

The second uniform shell was grown as follows: 4 mL Cd-oleate diluted in 20 mL ODE and 427 µL octanethiol diluted in 23.6 mL ODE were continuously injected at a speed of 12 mL/h to grow the second shell. The reaction temperature was elevated to 310 ^{o}C before injection. After 13 mL injections of Cd-oleate in ODE solution, 5 mL oleylamine was injected into the solution to improve the dispersibility of the QDs.

Core-shell QD purification

When the injection was complete, the final reaction mixture was naturally cooled to

$\sim$50 ^{o}C and transferred into 50 mL plastic centrifuge tubes, no anti-solvent was added and the precipitation was collected after 3 min centrifugation at a speed of 6000 rpm. 20 mL hexane was added into the centrifuge tubes to disperse the QDs, and acetone was added dropwise until the QDs started to aggregate. The precipitation was collected again by 3 min centrifugation at a speed of 6000 rpm, this dispersing and precipitate process was repeated 3 times to completely remove smaller CdS QDs. The final QDs were re-dispersed in octane with first exciton peak absorbance in 1 mm path length fixed as 0.25.

Hydrostatically strained QD synthesis

Conventional symmetric QDs were synthesized through modifying a published method.[53] A 8.8 mL CdSe core dispersion with an optical density of 1 at the exciton peak 590 nm was added to a mixture of 24 mL ODE and 24 mL OLA in a 500 mL flask, and pumped in vacuum at 100 ^{o}C to evaporate hexane, then the solution was heated to 310 ^{o}C and kept for 0.5 h. 6 mL as-prepared Cd-oleate was diluted in 18 mL ODE and 640 μL octanethiol in 23.36 mL ODE as sulfur precursor. Cd-oleate and octanethiol solutions were injected simultaneously and continuously at a rate of 12 mL/h. After injection, 4 mL OA was injected and the solution was further annealed at 310 ^{o}C for 10 min.

Absorption and photoluminescence measurements

QDs in hexane dispersion were collected into a 1mm path length quartz cuvette and measured on a Cary 60 UV-VIS spectrometer over an excitation range from 400 to 800 nm. PL spectra were collected on a PTI QuantaMaster fluorescence spectrophotometer using a 75 W Xe arc lamp as the excitation source. PL was measured with a 1 sec. integration time and a 1 nm slit width.

Transmission electron microscopy

HRTEM and STEM-EDS samples were prepared by adding a drop of the solution of QDs onto an ultrathin-carbon film on lacey-carbon support film (Ted Pella 01824) and were baked under high vacuum at 165 ^{o}C overnight and subsequently imaged using a Tecnai Osiris TEM/STEM operating at 200 kV. Drift-corrected STEM-EDS maps were acquired using the Bruker Esprit software with a probe current on the order of 1.5 nA and about 0.5 nm probe size.

Single QD optical spectroscopy

To obtain single-QD photoluminescence measurements, dilute solutions of QDs in hexanes were drop-cast on quartz substrates. Single-particle photoluminescence measurements were conducted using a custom-built epifluorescence microscope modified from Dukes *et al.*[49] Samples were excited by a 400 nm, frequency-doubled 76 MHz Ti:Sapphire pulsed laser or with a 405 nm PicoQuant pulsed diode laser operating at a repetition rate of 1 MHz using low powers (5-10 W/cm^{-2}). Photoluminescence was collected through a water-immersion Olympus objective with a numerical aperture of 1.2. A flip mirror is used to project the emission individual QDs onto the entrance slit of an Ocean Optics QE spectrometer (600 lines mm^{-1}) equipped with a Hamamatsu, back-illuminated cooled charge-coupled device (CCD) array for detection. Time series of integrated spectra were acquired at room temperature with integration times of 50 ms. For blinking analysis the photoluminescence from individual QDs was imaged onto an electron-multiplying charge coupled device (EM-CCD). Time-dependent intensity traces were recored at 20 KHz (50 ms per frame). A Hanbury-Brown Twiss interferometric setup was used to measure the second-order intensity correlation function, $g^2(\tau)$.

Chapter 4

Development and Single Particle Characterization of Cadmium-free Thick-Shell InP-ZnSe Quantum Dots[1]

Thick-shell (> 5 nm) InP-ZnSe colloidal quantum dots (QDs) grown by a continuous-injection shell growth process are reported. The growth of a thick crystalline shell is attributed to a high temperature, slow growth process and the relatively low lattice mismatch between the InP core and ZnSe shell. In addition to a narrow ensemble photoluminescence (PL) line-width ($\sim$ 40 nm), single particle emission measurements indicate that blinking is suppressed in these heterostructures. More specifically, high single dot ON-times (> 95%) were obtained for the core-shell QDs. Further, high-resolution energy dispersive X-ray (EDS) chemical maps directly shows for the first time significant incorporation of indium into the shell of the InP-ZnSe QDs. Examination of the atomic structure of the thick-shell QDs by high angle annular dark field scanning transmission electron microscopy (HAADF-STEM) reveals structural defects in sub-populations of particles that may mitigate PL efficiencies ($\sim$ 40% in ensemble), providing insight towards further synthetic refinement. These InP-ZnSe heterostructures represent progress toward fully cadmium-free QDs with superior photo-physical properties important in biological labeling and other emission-based technologies.

4.1 Introduction

Colloidal semiconductor nanocrystals, also known as quantum dots (QDs), offer great promise as ideal optical materials for a number of emission-based technologies. Indeed, QDs have recently been popularized by their use as phosphors in wide-gamut, high bright-

---

[1] Adapted with permission from Reid, K. R.; McBride, J. R.; Freymeyer, N. J.; Thal, L. B.; Rosenthal, S. J., "Chemical Structure, Ensemble and Single-Particle Spectroscopy of Thick-Shell InP–ZnSe Quantum Dots" Nano Letters 2018 18 (2), 709-716. Copyright 2018 American Chemical Society.

ness displays.[72] In biology, QD labeling strategies developed for single molecule tracking allow detailed mapping of cellular and neuronal processes over extended periods.[73] QDs have also been developed for use in solid-state lighting,[55, 74] luminescent solar concentrators (LSCs),[5] low threshold solution-processed lasers,[6] and as single and entangled photon sources.[50, 75] However, the bulk of progress towards the commercialization of QD technologies has so far centered on the development of cadmium-based materials, which are optically active at visible wavelengths and are fairly easy to synthesize with high quality photo-physical properties.[40, 53] With concerns over the toxicity of cadmium [76] and recent restrictions on its use in consumer products, considerable effort has been devoted to developing copper-indium chalcogenides and indium phosphide (InP) QDs as cadmium-free alternatives.

InP is of particular interest due to its size-tunable emission over the visible and near infrared spectral range (band gap $\sim$ 1.35 eV) and lower intrinsic toxicity.[77] However, compared to ubiquitous cadmium selenide (CdSe) QDs, InP QDs suffer from synthetically induced broad size distributions, have relatively low photoluminescence (PL) quantum yields (QY) and poor environmental stability.[78] While significant attention has been given to improving these aspects of InP QDs,[79–81] InP QDs are further characterized by strong PL instability/blinking at the single dot level,[20] where the intensity of the emission from individual nanocrystals cycles between high and low values under continuous excitation.[19] PL blinking limits the use of QDs in single-molecule tracking experiments, as stable single-photon sources and in other emission-based applications. The most proven strategy to minimize blinking in QDs has been to encapsulate the QD core in a thick crystalline inorganic shell.[54, 82] In this way, excited charge carriers are decoupled from the nanocrystal surface and surrounding environment.

In this work, we encapsulate InP QDs in a thick (> 5 nm) crystalline zinc selenide (ZnSe) shell. Thick-shell growth is credited to slow continuous injection of the shell material at high temperature and a small lattice mismatch [11] (3.4%) between the core and shell material. Concomitantly, high-resolution chemical maps of the QDs provides evidence for alloying of indium into the shell, which could further facilitate thick shell growth. The resulting core-shell heterostructures exhibit significant room temperature blinking suppression, characterized by ON-time fractions that can exceed 95% despite a modest PL QY in ensemble. Using high-angle angular dark-field scanning transmission electron microscopy (HAADF-STEM) we further identify structural defects in the shells of sub-populations of QDs that are potentially responsible for mitigating PL efficiencies in the thick-shell heterostructures.

4.2 Development of Thick Shell InP-ZnSe QDs

Figure 4.1a shows the absorbance and PL spectra of a sample of thick-shell InP-ZnSe QDs. Zinc (II) oleate and selenium dissolved in trioctylphosphine are employed as shell precursors. Shell growth is carried out at high temperature (300 °C) *via* a continuous injection route in an inert atmosphere. During the growth procedure the QDs develop a strong absorbance feature at photon energies in the blue part of the visible spectrum; the onset of which matches the band edge of bulk ZnSe (2.7 eV, 460 nm) and is consistent with the growth of a large shell. Additionally, both the absorbance and PL of the InP-ZnSe QDs significantly shift to lower energy (InP core emission peak $\sim$ 590 nm) during the first 2 hours of shell growth, a signature of relaxed exciton confinement induced by the ZnSe shell.[80] We remark that calculated conduction band offsets for bulk InP-ZnSe ($\sim$ 0.39 eV),[83] are comparable to accepted values for CdSe-CdS core-shell QDs ($\sim$ 0.32 eV) [84] in which photo-excited electrons delocalize into the CdS shell.[85] Similarly to these CdSe-CdS heterostructures, a larger valence band offset likely strongly confines excited holes to the InP core.[86] The InP-ZnSe heterostructures exhibit PL QYs of $\sim$ 40% at room temperature (emission maximum $\sim$ 2.0 eV, 620 nm) and a full-width at half-maximum (FWHM) of $\sim$ 40 nm ($\sim$ 130 meV), which is among the highest color purities reported for InP QDs.[87]

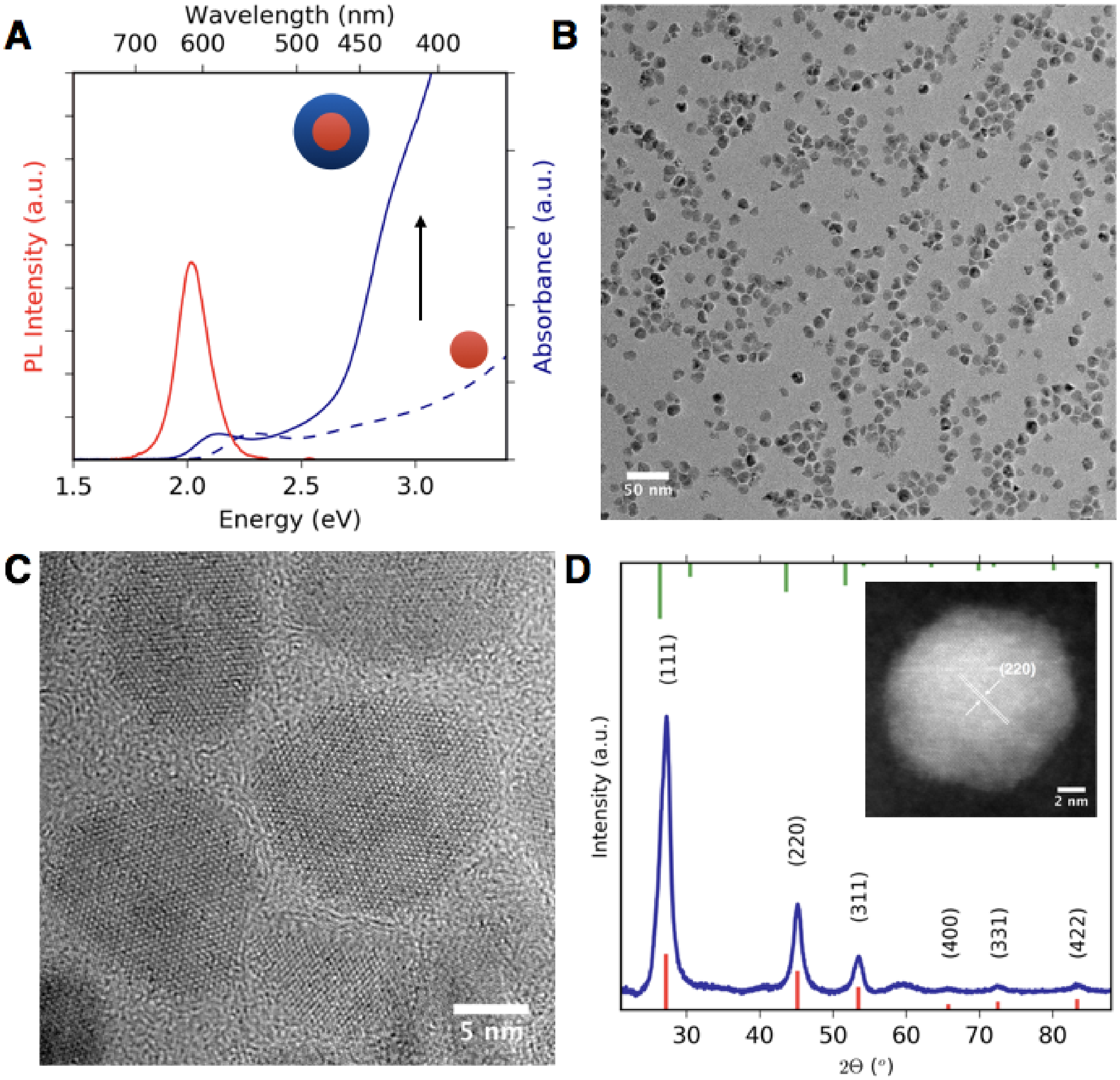

Figure 4.1: Optical and structural characterization of thick-shell InP-ZnSe QDs. (a) Absorption (blue) and photoluminescence (PL) (red) spectra of a batch of thick-shell InP-ZnSe QDs. Dotted line corresponds to the absorption spectrum of the starting InP core. (b) TEM image of the InP-ZnSe core-shell heterostructures. (c) High-resolution TEM image of the QDs. (d) X-ray powder diffraction pattern obtained from the sample shown in b. Inset: High-resolution high-angle annular dark-field (HAADF) STEM image of a InP-ZnSe QD. The red (green) tick pattern show the reference XRD peak positions of bulk zinc-blende ZnSe (InP).

Imaging of the QDs using transmission electron microscopy (TEM) shows that following ZnSe shell growth, the average diameter of the particles increases from $\sim$ 3.0 nm for the InP core to 14.1 nm (Figure 4.1b), corresponding to a shell thickness of $\sim$ 5.5 nm ($\sim$ 17 monolayers). We note a slight degree of irregularity in the shapes and morphology of the QDs produced by our shell growth method, highlighting the challenges and complexities related to InP epitaxy. The possible implications of these irregularities on the optical properties of the QDs are discussed below. Despite this, we obtain size distributions comparable to similarly thick-shell CdSe-CdS QDs of $\sim$ 11%.[82]Furthermore, high-resolution transmission electron microscopy (HR-TEM) (Figure 4.1c) depicts the highly crystalline nature of the heterostructures, revealing that they can be uniform and faceted with lattice fringes throughout. The lattice spacing ($\sim$ 0.21 nm) depicted in the high-resolution image acquired in HAADF-STEM mode (Figure 4.1d, inset) corresponds to the (220) plane of the zinc-blende (ZB) crystal structure. Powder X-ray diffraction (XRD) measurements (Figure 4.1d) supports epitaxial growth of ZB-ZnSe on top a ZB-InP core, indicating a retention of the starting crystal phase.

4.3 Chemical Structure and Elemental Distribution

Figure 4.2a shows a high-resolution energy dispersive X-ray (EDS) chemical map of a core-shell InP-ZnSe QD. The map reveals in great detail the location of the core and shell elements of the particle and clearly shows that the InP core tends to be centered in a symmetrically grown ZnSe shell. This is further confirmed by a line scan profile of the QD (Figure 4.2b). Interestingly, the chemical maps also show that during shell growth, indium is distributed across the core-shell interface and into the ZnSe shell (Figure 4.2c) of the heterostructures. Specifically, a $\sim$ 2% (atomic percent) incorporation of indium in the ZnSe shell was estimated from the EDS maps, (Figure 4.3 suggesting that during shell growth indium alloys into the shell of the core-shell structures. This incorporation of indium into the shell may have implications on the shell growth as well as the optical properties of the QDs.[88, 89] Future experiments will be needed to determine the precise role that alloying plays in these thick-shell QDs. However, it possible that alloying further facilitates the growth of a uniform thick-shell by alleviating strain at the epitaxial interface of the core and shell materials. The EDS maps additionally provide information on the relative amounts of each element present throughout the entire QDs and indicate that the core-shell particles are predominantly ZnSe (96% by composition) as expected.

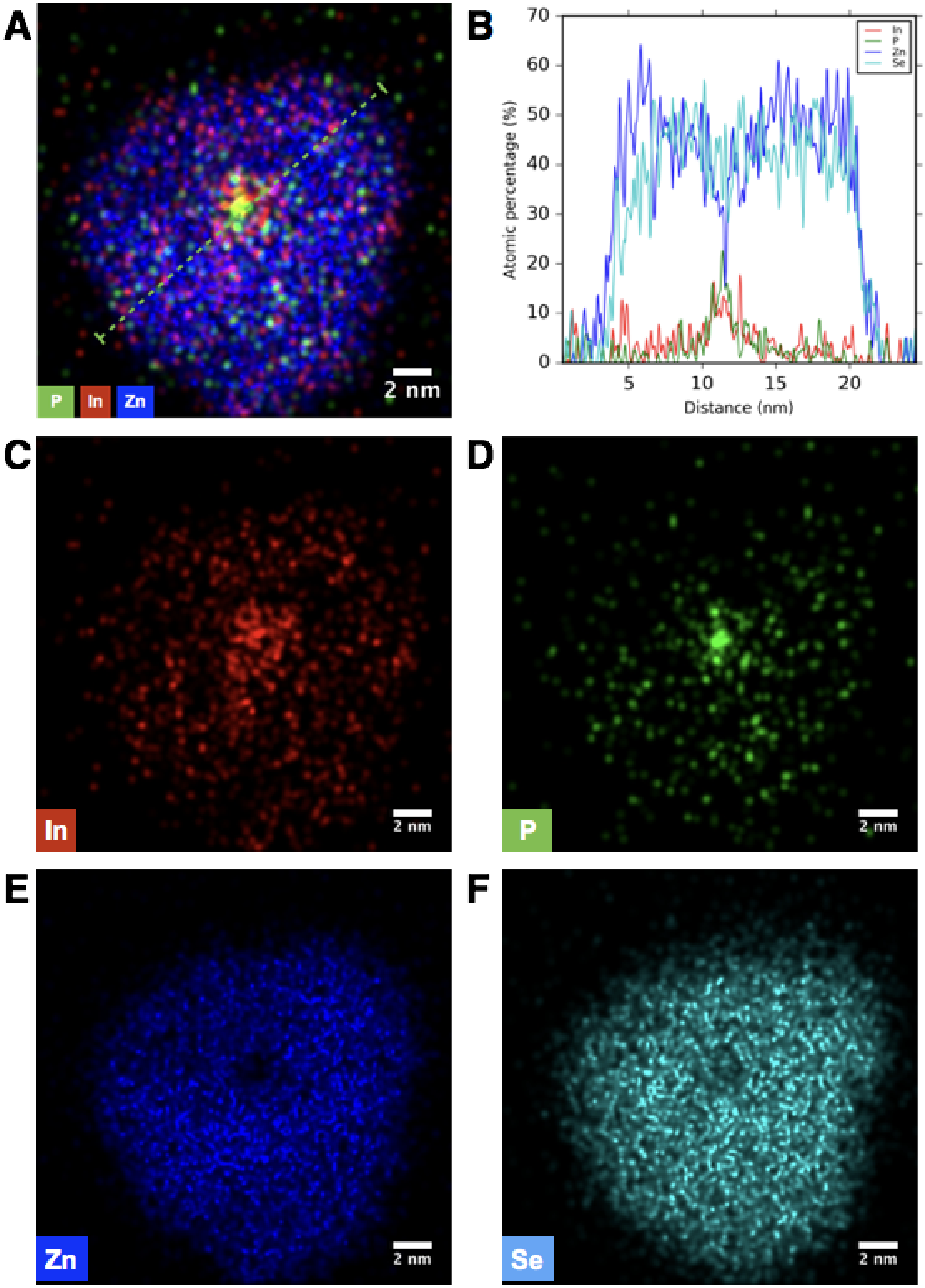

Figure 4.2: Elemental characterization of thick-shell InP-ZnSe QDs. (a) Energy dispersive X-ray (EDS) chemical map of a core-shell InP-ZnSe QD. (b) Corresponding line scan showing the intensity profile of each element across the diameter of the particle. (c) Indium, (d) Phosphorus, (e) Zinc and (f) Selenium chemical maps from the particle in a.

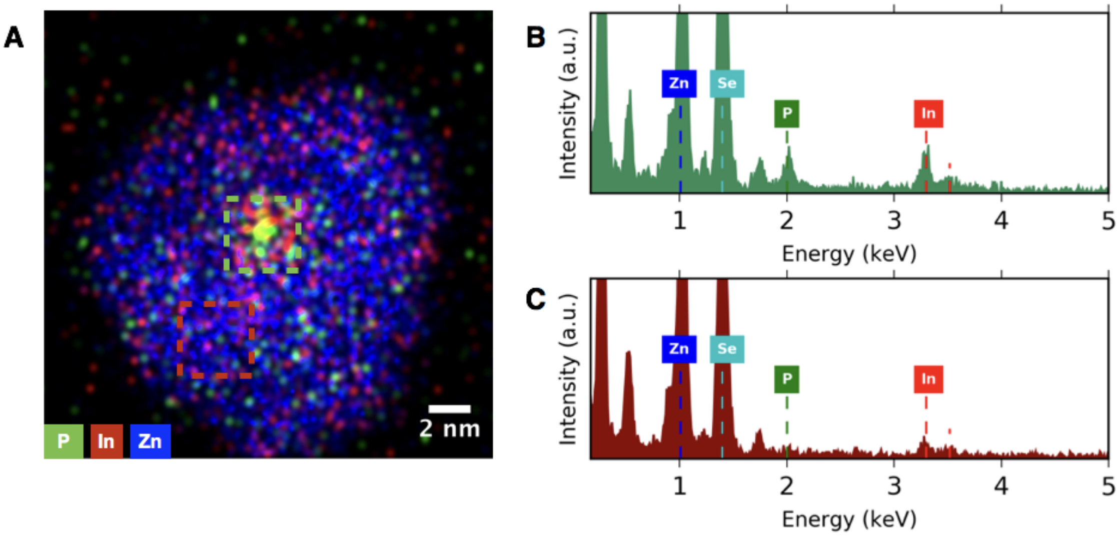

Figure 4.3: Quantification of Indium in the thick-shell InP-ZnSe QDs. (a) Energy dispersive X-ray (EDS) map of the thick-shell InP-ZnSe QD in figure 2a. The region of interests (ROIs) labeled in green and red correspond to core and shell regions respectively of the core-shell particle. (b) EDS spectra for the core ROI. (c) EDS spectra rendered from the shell ROI. Average atomic percentages of In: core ROI (4.8%), shell ROI (2.3%). Average atomic percentages of P: core ROI (4.1%), shell ROI (undetected).

4.4 Blinking Suppression in Single Thick-Shell InP-ZnSe QDs

In order to characterize the thick-shell InP-ZnSe structures at the single-dot level, blinking measurements were conducted on individual core-shell nanocrystals. The core-shell QDs were diluted to $\sim$ 1 nM concentration and drop-cast onto glass cover-slips. The resulting films were sealed in a nitrogen dry-box in order to minimize the influence of photo-oxidative degradation on the blinking behavior of the QDs over the time period investigated. The emission from single dots was collected with a custom-built epi-fluorescence microscope using a 400 nm (3.1 eV), 76 MHz laser for excitation.[48] The mean separation between QDs of around 4 μm, minimizes the possibility of observing emission from aggregates. Single-dot PL intensity-time traces were recorded using an electron-multiplying CCD (charge-coupled device) camera at 10 Hz (100 ms per frame) for up to ten minutes. An intensity-time trace for a thick-shell InP-ZnSe QD and corresponding intensity distribution are shown in Figure 4.4a. The emission intensity can be seen to fluctuate between

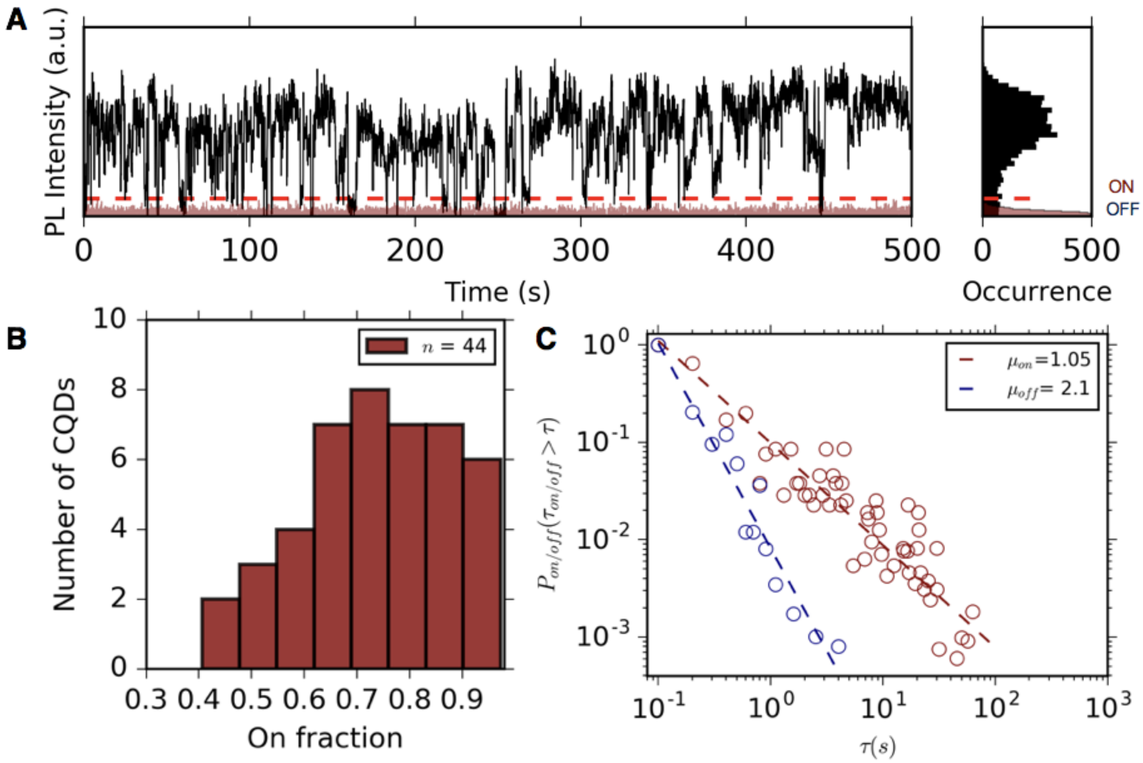

Figure 4.4: Photoluminescence blinking behavior of single thick-shell InP-ZnSe QDs**. (a) Intensity-time trace and distribution of the PL intensity from an individual InP-ZnSe QD (bin size is 100 ms). The background (red trace) was recorded from a region with no QDs. Dotted (red) line represents the ON-OFF threshold for analysis. (b) Distribution of the blinking ON-time fraction. (c) Distribution of ON (red) and OFF (blue) time durations plotted on a log-log scale. Dashed lines represent power-law ($\tau^{-\mu_{off/on}}$) fits to the data.

high ('ON') and low ('OFF') values. To quantify this blinking behavior, the time spent in high intensity periods (ON-time) during the course of the experiment was extracted from each QD studied (n = 44). A QD is considered to be in the ON state when its emission intensity is above, $\langle BG\rangle + 4\sigma$, where $\langle BG\rangle$ is the mean background signal from a spot without QDs and σ is the standard deviation. The core-shell InP-ZnSe QDs studied have an average ON-time $\sim$ 80% with several (15%) individuals having ON-time fractions in excess of 90% (Figure 4.4b). Although our observations were conducted in a reduced-air environment, blinking measurements made in air using a lower energy excitation source indicate that the thick-shell dots can be stable under ambient conditions (Figure 4.5).

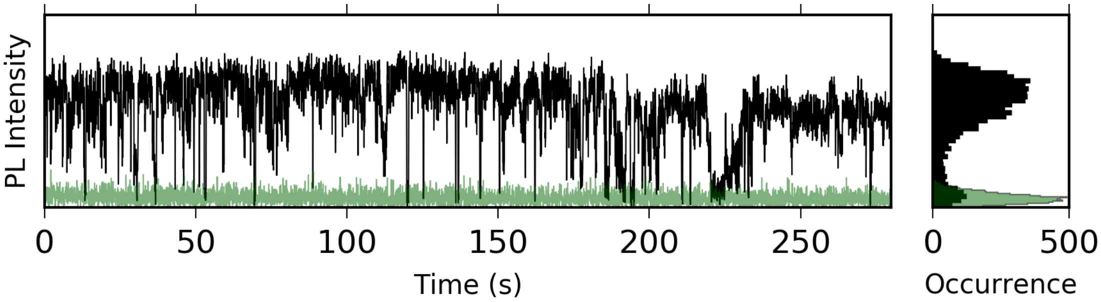

Figure 4.5: Additional blinking trace and intensity histogram of an individual thick-shell InP-ZnSe QD recorded in air using a lower energy excitation source (488 nm, 2.5 eV). The background (green trace) was recorded from a region with no QDs.

To understand the observed blinking reduction in the thick-shell InP-ZnSe QDs, we consider further the processes that lead to blinking. In QDs, blinking is commonly thought to originate from one of two processes; dubbed type A and type B blinking.[26] In A-type blinking - conventional charging/discharging model,[21] a nanocrystal becomes charged following photo-induced Auger ionization or trapping (long-lived) of excited charge carriers and the emission is dominated by non-radiative Auger recombination. In B-type blinking, off events arise when excited ’hot’ charge carriers become trapped at recombination centers that introduce non-radiative recombination channels other than Auger recombination.[90] Independent of a particular model; PL blinking is initiated when excited charge carriers become trapped at defects typically situated at the surface of the nanocrystal or within the external environment. By encapsulating the InP QD core in a thick crystalline shell, these traps become less accessible to excited charge carriers. In this way, the thick ZnSe shell serves as a physical barrier that decouples excited carriers from the nanocrystal surface and surrounding environment.

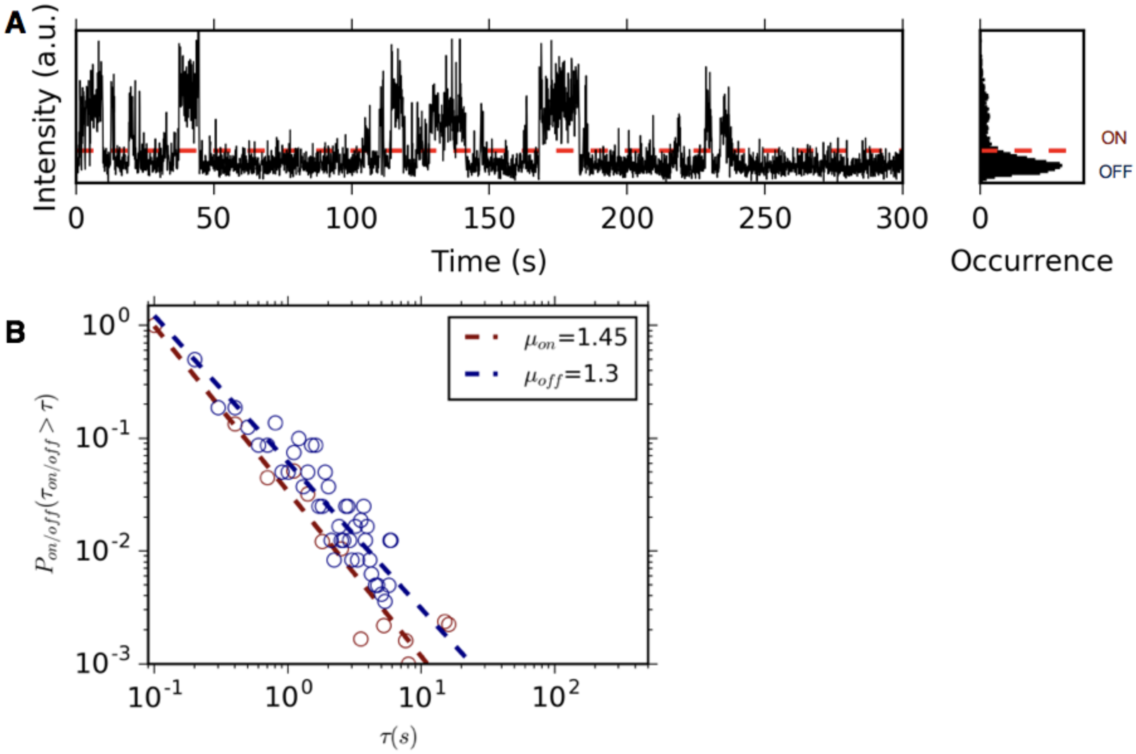

Figure 4.6: Representative single QD intensity-time trace and intensity distribution from the InP-ZnS sample synthesized by our method for which the extracted ON-time fraction was 20% (n=15). The dashed red line represents the chosen ON-OFF threshold. (b) Distribution of ON (red) and OFF (blue) time durations plotted on a log-log scale. Dashed lines represent power-law ($\tau^{-\mu_{off/on}}$) fits to the data, μ_{off} = 1.3 and μ_{on} = 1.45.

In stark contrast to thick-shell InP-ZnSe QDs, single InP-ZnS QDs prepared using the same starting InP core were characterized by strong blinking, with typical ON-time values < 25% (Figure 4.6a). We remark that ZnS is the most commonly employed shell material used to passivate InP QDs. The large amount of time that the InP-ZnS core-shell particles spend in the off state can be attributed to the limited shell growth that typical occurs in the overcoating process ($\sim$ 1.7 nm). This is due to the large lattice mismatch between InP and ZnS ($\sim$7.7% for zinc blende phases)[11] which restricts the growth of thicker shells. As a result, excited charge carriers more readily overlap with the disordered nanocrystal surface. In addition, the lattice mismatch can result in the formation of defects within the shell and at the interface of the core-shell heterostructures during growth as strain between the core and shell relax to form defects at the core-shell interface or within the ZnS shell.[44] Indeed, such defects can increase the availability of trap sites for charge carriers, inducing strong intermittent emission from individual QDs.[48]

The PL intermittency of the single QDs can further be characterized by observing the statistics of the duration of OFF and ON times, $\tau_{off/on}$. This approach has been used extensively to study the long-time kinetics related to blinking in QDs and other systems.[91, 92] In Figure 4.4c, the cumulative distribution of $\tau_{off/on}$, that is, the probability, $P_{off/on}(\tau_{off/on} > \tau)$, of observing an OFF or ON period greater than τ is plotted for InP-ZnSe QDs. In QDs this distribution follows a power-law distribution, $P_{off/on}(\tau_{off/on}) \sim \tau^{-\mu_{off/on}}$, where $\mu_{off/on}$ is the power-law exponent describing the statistics of OFF or ON periods. Previously reported values for $\mu_{off/on}$ in InP QDs with high blinking rates are close to 1.5.[20] For the thick-shell InP-ZnSe QDs (trace shown in Figure 4.4a), $P_{off/on}(\tau_{off/on} > \tau)$ can be fitted to a power-law distribution with $\mu_{off} = 2.1$ and $\mu_{on} = 1.05$. The values of the power-law exponents indicate that PL blinking is dominated by much shorter OFF events and longer ON periods, consistent with the observation of higher on-times. The departure of $\mu_{off/on}$ in InP-ZnSe QDs from typical values is in good agreement with previous results obtained for CdSe-CdS [53, 82] and suggests that access of photo-excited charge carriers to trap sites is restricted in the InP-ZnSe heterostructures.

4.5 Structural Defects in QD Subpopulation

Despite successful thick-shell growth, we note that several InP-ZnSe QDs have low ON-times and the ensemble PL QY ($\sim$ 40%) is relatively low compared to values that have be obtained for thinner shelled InP heterostructures.[81] These observations indicate that while a thick ZnSe shell may restrict access to surface-related trap states, moderate quantum efficiencies and incomplete blinking suppression possibly arise from imperfections in the internal structure of some particles within the synthetic batch, giving rise to a dim or dark population of QDs. Emission from these QD subpopulations would be expected to be dominated by non-radiative processes that quench their PL. Indeed, our group has

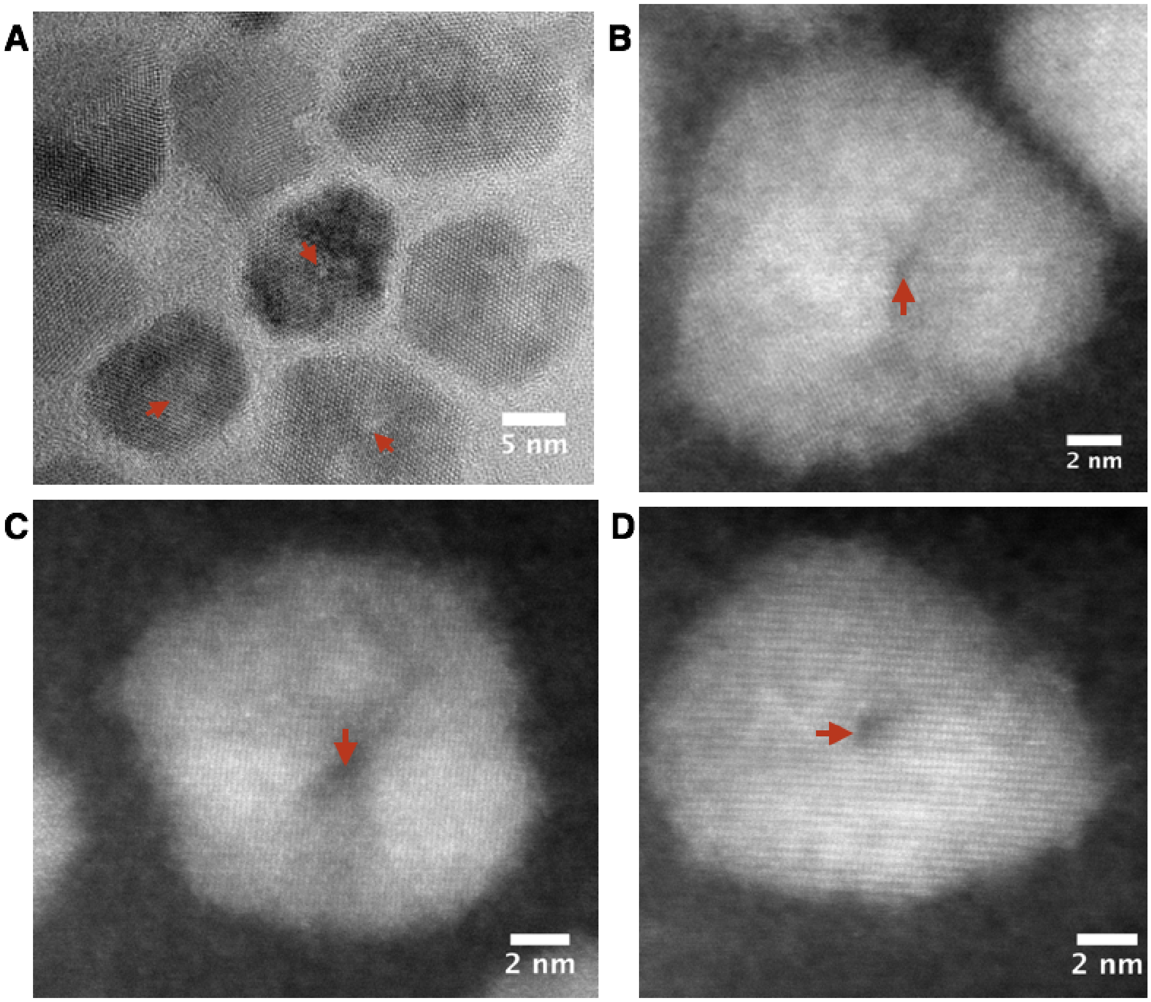

Figure 4.7: Imaging of structural defects in thick-shell InP-ZnSe QDs. (a) HR-TEM image showing low-contrast features in the InP-ZnSe QDs (red arrows). (b-d) HAADF-STEM images of InP-ZnSe core-shell QDs with extended (bulk) shell defects propagating from the InP core region.

previously identified dim and dark defected sub-populations in thick-shell CdSe-CdS QDs afflicted by strong PL intermittency and contributing to low ensemble PL QYs.[48, 93]

Figure 4.7a shows a HR-TEM image of the thick-shell InP-ZnSe QDs. Besides some residual structural inhomogeneity, there are apparent regions of low contrast in some of the particles within the synthetic batch. We utilized HAADF-STEM in conjunction with a very low beam current to image the atomic structure of several of these particles without inducing damage. The HAADF-STEM images in Figures 4.7b-d clearly show extended features in the shell structure near the core region of the particle that are likely one of the primary factors limiting the PL QY of the material. These unique features may be the result of a point defect propagating from the InP core, prohibiting proper shell growth. Additionally, in the case of InP QDs, it has been shown that high temperature (>250 °C) growth processes employing carboxylate precursors can lead to the formation of an irregular amorphous oxide layer at the surface of the InP core.[94] Uniform shell growth atop such a disordered surface layer would be expected to be difficult, if at all possible, and may be a plausible explanation for this non-uniform defected shell growth observed for some particles. Furthermore, any oxidation at the core-shell interface potentially introduce defects at the surface of the InP core that render the ZnSe shell passivation ineffective. In the future, direct investigations of the relationship between the atomic structure and optical properties of these thick-shell InP-ZnSe QDs at the single QD scale should provide additional insight into the effects of the observed structural irregularities on the performance of the heterostructures.

4.6 Conclusion

In conclusion, we have synthesized InP core-shell QD nanostructures with a thick (> 5 nm) crystalline inorganic shell. This was achieved by employing a slow shell growth process at high temperatures. Thick-shell growth was also facilitated by a small lattice mismatch between the InP core and ZnSe shell material. These cadmium-free QD heterostructures feature suppressed blinking—characterized by high ON-time fractions at the single particle level. The observed blinking reduction is attributed to the large uniform ZnSe shell volume, which isolates excited charge carriers from the nanocrystal surface and surrounding environment—where they can become trapped and undergo non-radiative recombination. Advanced high-resolution STEM and EDS imaging provide an unprecedented level of insight into the atomic and chemical structure of the thick-shell QDs. Structural imaging pinpoint morphological irregularities in the shell that possibly limit the optical performance of the developed thick-shell nanostructures. Further work should involve direct correlation of the structure and optical properties of individual thick-shell InP-ZnSe QD structures in order to gain a deeper understanding of the developed heterostructures. This could inform synthetic refinements necessary to enable these cadmium-free dots for applications in challenging biological settings and in other emission-based technologies. The next chapter presents an example in which this correlation is conducted.

4.7 Experimental Methods

Materials

Indium (III) acetate (99.99%-in), tris(trimethylsilyl)phosphine (95%), myristic acid (99%), oleic acid (90%, technical grade), 1-octadecene (ODE, 90%, technical grade), trioctylamine (TOA, 98%) and trioctylphosphine (TOP, 97%) were obtained from Aldrich. Zinc acetate (98%, extra pure) was obtained from Acros Organics. Selenium powder (99.99%, 200 mesh) was obtained from Alfa Aesar. Sulfur powder (99.99%), isoproponal (99.9%) and toluene (99.9%) were obtained from Fisher Scientific. All chemicals were used without further purification unless noted otherwise.

Precursor preparation

Indium myristate and zinc myristate were synthesized according to a previously published method.[95] Zinc oleate (0.4 M) was prepared by heating 1.6 g of zinc acetate in 12 mL of oleic acid and 8 mL TOP under argon at 150 °C for 30 min until the zinc acetate was dissolved. The solution was then degassed at 100 °C under vacuum for 30 min. TOP-Se (0.4 M) was prepared by dissolving 640 mg of selenium powder in 20 mL TOP with stirring overnight in a nitrogen-filled drybox. TOP-S (0.4 M) was prepared by heating 256 mg of sulfur in 20 mL TOP at 100 °C until completely dissolved in a nitrogen drybox.

InP core synthesis

Zinc blende InP QD cores were synthesized using a modified literature protocol [96]. Briefly, 160 mg (0.2 mmol) indium myristate and 5 mL ODE were added to a 100 mL

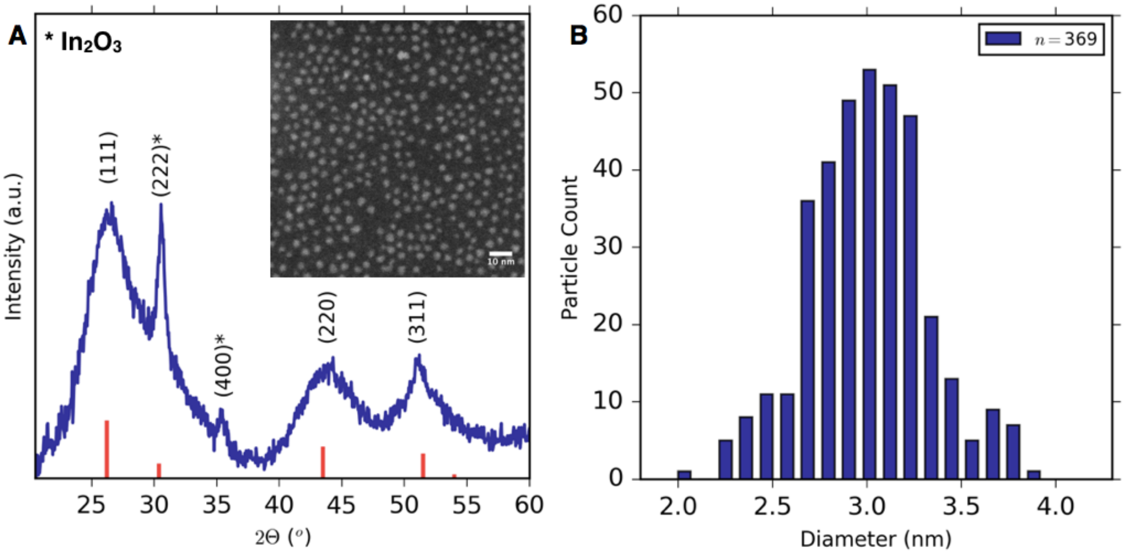

Figure 4.8: InP core crystal structure and size distribution. (a) X-ray powder diffraction pattern obtained from the InP starting cores. The stick pattern (red) shows the reference peaks of bulk zinc blende InP. Peaks resulting from oxidation to In_2O_3 are denoted by an asterisk (*). Inset: HAADF-STEM image of the particles. (b) Size distribution of the InP cores. The average particle diameter is $\sim 3.0 \pm 0.3$ nm

three-neck round-bottom flask. The mixture was heated to 100 °C with stiring and degassed under vacuum for 30 min. The reaction was then placed under an argon atmosphere and heated to 300 °C. In a nitrogen drybox, 45 μL (0.15 mmol) tris(trimethylsilyl)phosphine ($(TMS)_3P$) was mixed with 1 mL TOP. The $(TMS)_3P$ solution was quickly injected into the reaction flask and the QDs grown for 30 minutes before cooling to room temperature. The nanocrystals obtained were typically 3 nm in diameter (Figure 4.8).

ZnSe and ZnS shell growth

For ZnSe shell growth, 50 mg of zinc myristate and 3 ml TOA were loaded into the reaction flask consisting of freshly made InP cores. The mixture was degassed at 100 °C under vacuum for 30 min to remove water and oxygen inside the solution. The flask was then filled with argon and heated to 300 °C. A mixture of zinc oleate (6 mL, 0.4 M stock) and TOP-Se (6 mL, 0.4 M stock) was added drop-wise into the growth solution at a rate of 1.5 mL/h using a syringe pump. The reaction solution was further annealed at 300 °C

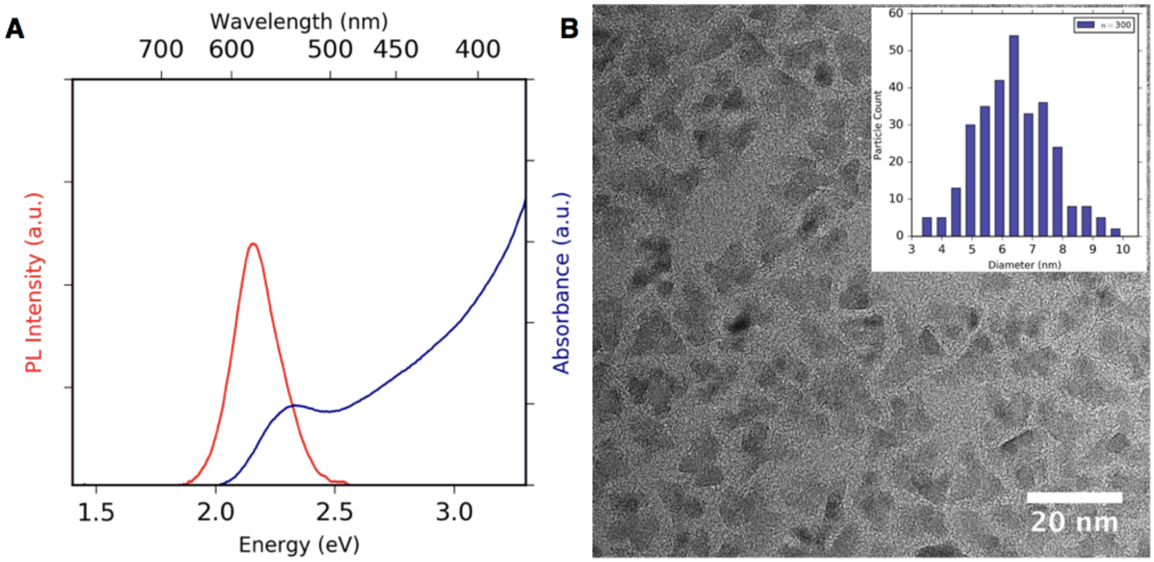

Figure 4.9: Characterization of InP-ZnS QDs. (a) Absorption (blue) and Photoluminescence (red) spectra of the InP-ZnS QDs. The PL is centered around 585 nm with a FWHM $\sim$ 51 nm (165 meV) and PL QY $\sim$ 43%. (b) The corresponding TEM image of the sample in a. Inset: Size distribution of the InP-ZnS QDs. The average particle diameter is $\sim$ 6.3 $\pm$ 1.3 nm. The InP-ZnS QDs produced are highly irregular, have a poor size distribution ($\sim$20%) and the average shell thickness ($\sim$ 1.7 nm) obtained is significantly less compared to employing ZnSe as the shelling material.

for 2 h. After cooling to room temperature the crude InP-ZnSe core-shell stock was stored in a nitrogen drybox. Samples for optical and structural characterization were prepared by washing with isopropanol and re-dispersing in toluene twice. ZnS shell growth was carried out using the above procedure, substituting TOP-S for TOP-Se. The InP-ZnS QDs grown had an average shell thickness of 1.7 nm(Figure 4.9).

Transmission electron microscopy (TEM) imaging

HRTEM, HRSTEM images were obtained using a Tecnai Osiris TEM/STEM operating at 200 kV equipped with a SuperX™ quad EDS detection system. Samples were baked at 165 °C under high vacuum prior to imaging. STEM-EDS maps were acquired using the Bruker Esprit software with a sub-nm probe having $\sim$ 1 nA of beam current (Spot size 6). Quantification was performed using the Cliff Lorimer method. Nanocrystal sizes were determined by manually measuring the diameters of QDs from TEM images in the ImageJ software.

Powder X-ray diffraciton

Powder X-ray diffraction (XRD) measurements were obtained using a Rigaku Smart-Lab X-Ray diffractometer operating at 40 kV and 44 mA using a Cu Kα line (λ = 1.5418 angstrom). XRD patterns were collected at a scan rate of 2 deg/min.

Ensemble Spectroscopy

Absorption spectra were recorded on a Cary 60 UV-VIS spectrometer. Photoluminescence (PL) spectra were collected on a PTI QuantaMaster fluorescence spectrophotometer using a 75 W Xe arc lamp as the excitation source. PL was measured with a 1 sec. integration time and a 1 nm slit width. Quantum Yield (QY) measurements were determined by comparing the PL of the QDs to a reference dye (R6G in methanol, QY $\sim$ 94%).

Single QD PL blinking measurement

For single nanocrystal blinking measurements, core-shell QDs were diluted to $\sim$ 1 nM concentration in toluene and drop-cast onto a No. 0 glass cover-slip. The resulting dried QD films were then packaged between the cover-slip and a cover glass and the assembly sealed with epoxy. The entire sample preparation was carried out in a nitrogen dry-box in order to minimize the influence of photo-oxidative degradation on the blinking behavior of the QDs over the time period investigated. Room temperature single QD intensity-time traces were acquired in wide-field configuration of a custom-built epi-fluorescence microscope.[48] The microscope uses a water immersion objective (Olympus, 60X, 1.2 NA). QDs were excited by a 400 nm, 76 MHz laser focused to a spot $\sim$ 60 μm in diameter. The average excitation power density was $\sim 5W/cm^2$. Emission from individual dots was collected through the objective and imaged onto an EM-CCD camera (Andor, iXonEM+, DU-897e-CSO-#BV). Intensity-time traces were recorded at 10 Hz (100 ms per frame).

Chapter 5

The Role of Surface Morphology on Exciton Recombination in Single Quantum Dot-in-Rods Revealed by Optical and Atomic Structure Correlation[1]

The physical structure of colloidal quantum dot (QD) nanostructures strongly influences their optical and electronic behavior. A fundamental understanding of this interplay between structure and function is crucial to fully tailor the performance of QDs and their assemblies. Here, by directly correlating the atomic and chemical structure of single CdSe-CdS quantum dot-in-rods with time-resolved fluorescence measurements on the same structures, we identify morphological irregularities at their surfaces that moderate photoluminescence efficiencies. We find that two non-radiative exciton recombination mechanisms are triggered by these imperfections: charging and trap-assisted non-radiative processes. Furthermore, we show that the proximity of the surface defects to the CdSe core of the core-shell structures influences whether the charging or trap-assisted non-radiative channel dominates exciton recombination. Our results extend to other QD nanostructures and emphasize surface roughness as a crucial parameter when designing colloidal QDs with specific excitonic fates.

5.1 Introduction

Precise control over optical and electronic properties is an important goal in the synthesis and assembly of colloidal quantum dot (QD) nanostructures. Because desired properties often derive from the confinement of excitons to near-atomic scale dimensions, the physical structure of quantum dots strongly influences manifested optical and electronic behavior.[97] A defining feature of QDs, for example, is that exciton energies can be extensively

---

[1] Adapted with permission from Reid, K. R.; McBride, J. R.; La Croix, A. D.; Freymeyer, N. J.; Click, S. M.; Macdonald, J. E.; Rosenthal, S. J. "Role of Surface Morphology on Exciton Recombination in Single Quantum Dot-in-Rods Revealed by Optical and Atomic Structure Correlation." ACS Nano 2018 12 (11), 11434-11445. Copyright 2018 American Chemical Society.

tuned by making adjustments to the dimensions of their physical structure.[1] Possibilities for control are further expanded by the ability to design structures that combine different geometries, compositions, crystal phases and surface chemistries owing to tremendous progress in the synthesis of QDs in recent years.[61, 62, 98]

However, despite these advancements in synthesis, colloidal preparations of QD nanostructures are often characterized by structural imperfections and inhomogeneities that lead to unwanted properties, including sub-unity photoluminescence (PL) quantum efficiencies,[44] blinking[19] and poor charge transport.[99] This becomes increasingly so when considering compositions other than archetypal cadmium-based QDs.[100, 101] Moreover, little is known about the microscopic nature of these imperfections or of the effect of dissimilar structures on macroscopic optical and electronic properties. A fundamental understanding of structure-function relationships is necessary in order to fully tailor the performance of QDs and their assemblies.

An often employed approach in this endeavor is the use of ensemble methods to monitor performance against variations in synthetic conditions. Although informative, ensemble measurements neglect the effects of structural variances among individual particles in the same batch. Instead, by studying QDs one by one, it is possible to bypass challenges in batch-level investigations, namely, averaging of measured responses, in order to uncover precise relations between the structure of a QD and its optical and electronic properties.[102] Recently, we demonstrated a simple platform to combine, without ambiguity, optical measurements from time-resolved fluorescence spectroscopy on single QD nanostructures with atomic-level structural and chemical information from the same QD captured with advanced electron microscopy.[48] This correlation provided a detailed view of the effects of synthetically-induced structural imperfections, such as stacking faults, incomplete shell epitaxy and surface defects on the optical performance of individual core-shell QD nanostructures.

Here, we extend our technique to study CdSe-CdS quantum dot-in-rod (DiR) nanostructures. DiRs comprise two components of different shapes: a QD core embedded in a rod-like shell. Elongation of the shell introduces improved properties over spherical core-shell QDs, including strong linear polarization of emission and efficient multi-photon absorption.[103, 104] Adjustments to the dimensions of the shell also allow extensive control over the exciton fine-structure, wave function overlap, exciton lifetimes and charge carrier localization and separation.[105–107] Furthermore, DiRs can be synthesized with good control over their dimensions and assembled into large, ordered, solid arrays and are a useful model system for investigating structure-function relationships in colloidal nanostructures. The remarkable properties of this system are also of interest in a growing number of applications, including displays,[108] light-emitting devices,[109] biological imaging,[110] luminescent solar concentrators,[111] exciton storage,[112] single-photon sources[113] and photo-catalysis.[18]

In this work, CdSe-CdS DiRs were synthesized using a well-established fast shell growth scheme.[70, 114]Interestingly, even with the fast growth rates taking place, structures produced using this procedure generally have narrow size distributions and PL quantum yields up to 75%.[105] However, despite the success and high repeatability of the conventional fast growth method, improvements in PL efficiencies remain limited. Additionally, quantum yields quickly decrease with further elongation of the CdS shell, restricting the utility of large aspect ratio structures. While reduced PL efficiencies have been attributed to trap-induced non-radiative exciton processes related to the growth of the CdS shell in the DiRs;[70] the physical origin of the defects associated with these traps has yet to be clearly elucidated. Moreover, the effects of fine structural variances among DiRs on exciton recombination remain to be examined. Using time-resolved single QD fluorescence spectroscopy we identified two non-radiative recombination mechanisms responsible for moderating PL efficiencies in DiRs: charging and trap-assisted non-radiative processes. Direct correlation of the structures of the DiRs with their fluorescence show that both processes are linked to morphological imperfections at the surface of the nanostructures. Furthermore, we show that the location of the defects influences the non-radiative channel that dominates exciton recombination.

5.2 Acquisition of Atomic, Chemical Structure and Optical Information for the Same Quantum Dot-in-Rod

The DiRs used in this study consist of 2.7 nm CdSe cores and CdS shells with an average shell length and diameter of 33 ± 3.5 nm and 6.4 ± 1.2 nm respectively (Figure 1). We also note that the DiRs have a similar solution PL quantum yield (70%) to state-of-the-art samples reported in literature.[70]

To probe both the fluorescence and structure of individual particles, a dilute concentration ($\sim$ 1 nM) of the DiR solution was deposited on an SiO_2 support film along with fluorescent localization markers (details in Methods). The markers facilitate accurate indexing of the PL and structural information collected from the same nanostructure (Figure 5.1). First, time-tagged, time-resolved PL measurements were conducted using time-correlated single photon counting (TCSPC) electronics in a custom-built epi-fluorescence microscope. This setup enabled the simultaneous acquisition of time-dependent PL intensity and PL lifetime data for each DiR. Subsequently, high-resolution structural images of the DiRs were acquired *via* high angle annular dark field detection (HAADF) using a scanning transmission electron microscope (STEM) equipped with energy dispersive X-ray spectroscopy (EDS) capabilities. STEM-EDS measurements allowed mapping the chemical composition of the same DiR structure. A summary of all the data collected on an individual DiR is presented in Figure 5.2. In total we examined 37 single DiRs from the same synthetic batch.

5.3 Exciton Recombination Dynamics

For each DiR, we analyzed correlations in the temporal variation of the PL intensity and the PL lifetime in order to gain insight into the dynamics underlying exciton recombination. All the DiRs exhibited random fluorescence intensity blinking between bright and dim

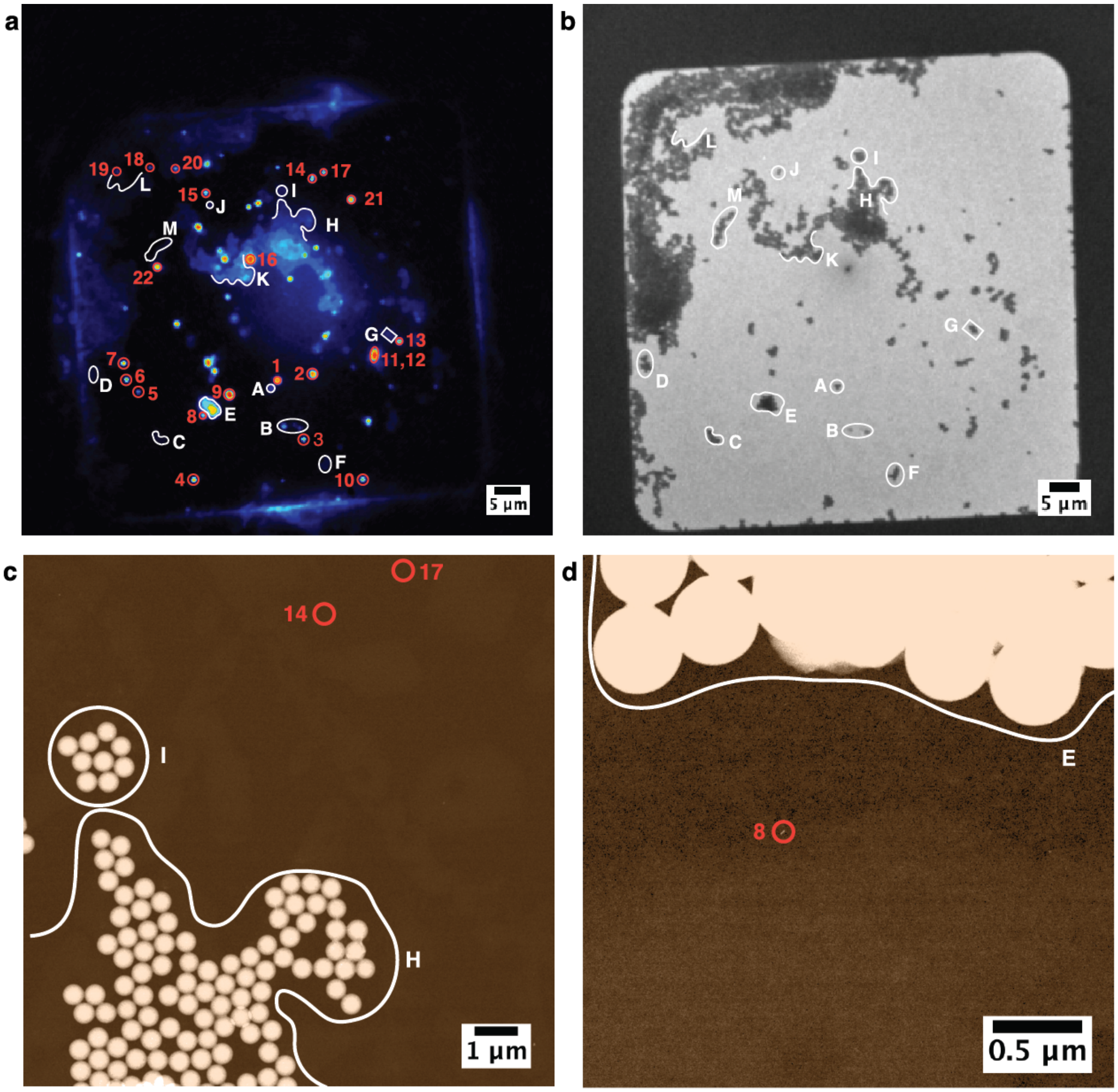

Figure 5.1: Correlation of single DiR fluorescence and atomic structure. (a) Wide-field fluorescence image of a SiO_2 support window. Single DiRs are denoted by red circles. Key polystyrene (marker) formations are outlined in white. (b) TEM image of the same support window. (c,d) False color HAADF-STEM images depicting the location of three DiRs.

emissive states but showed differences in the dynamics of the PL lifetime. The distinct PL behaviors observed are summarized in Figure 5.3.

5.3.1 A-type Quantum Dot-in-Rods

Figure 5.3a (top panel), shows the time-dependent PL intensity trace and intensity distribution for one of the DiRs. We see that the fluorescence cycles between bright and dim

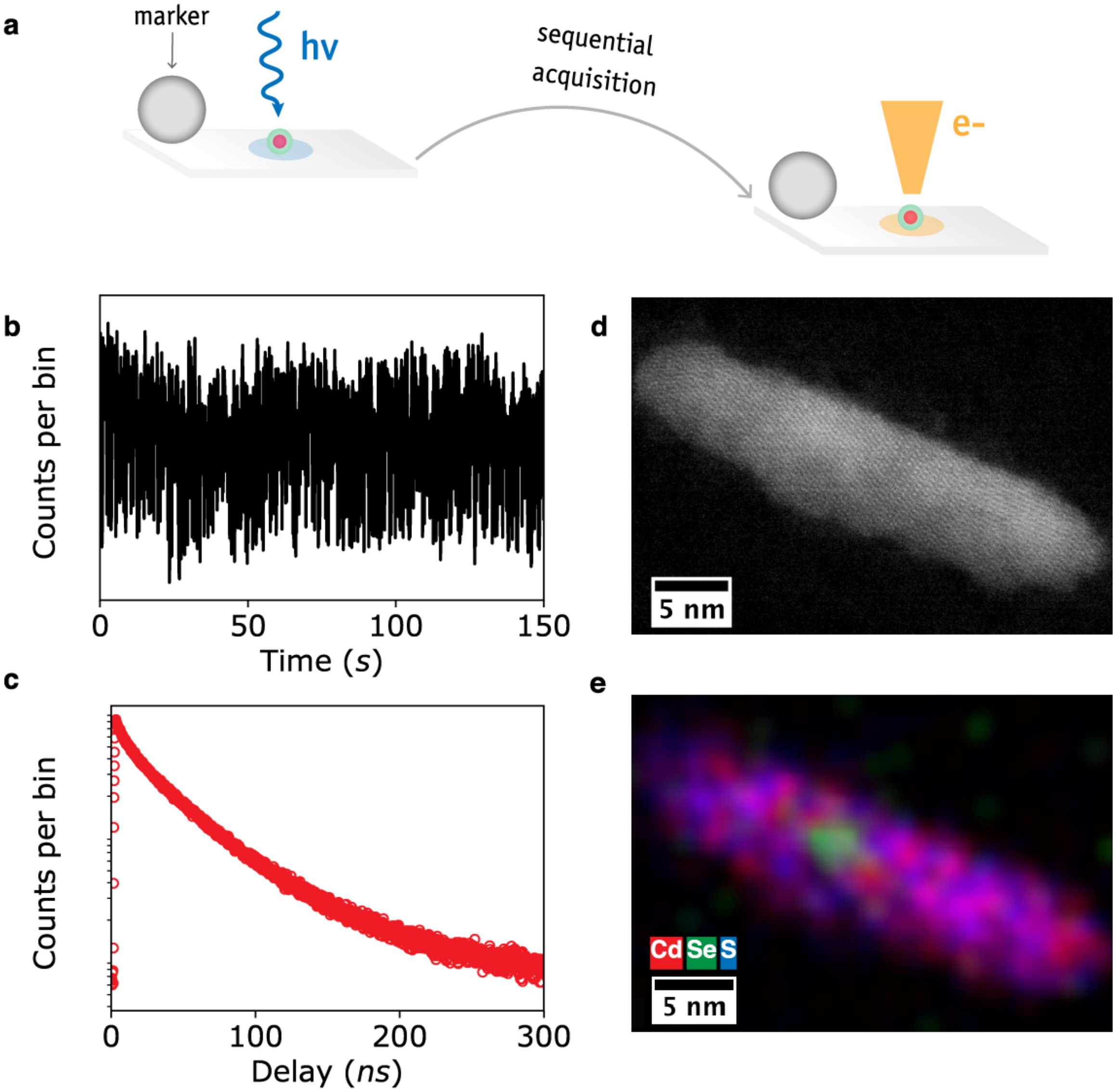

Figure 5.2: Optical, structural and chemical information collected from a single DiR using platform suitable for single QD optical spectroscopy and advanced electron microscopy. (a) Overview of work flow: A sparse collection of colloidal nanostructures is deposited on a SiO_2 support film along with positioning markers to facilitate instrument relocation and rapid acquisition of optical and structural data from the same nanostructure. Measurements for a single DIR include: (b) time-resolved photoluminescence intensity and (c) lifetime decay, (d) high-resolution atomic structure and (e) spatially-resolved chemical structure of the same DiR.

emissive states. A fluorescence lifetime-intensity distribution (FLID) constructed from the PL intensity and lifetime demonstrates that two states are mainly responsible for jumps in the fluorescence of the DiR (Figure 5.3b). Additionally, the FLID shows that transitions from the bright high intensity state to the less efficient dim state are correlated with shortened PL lifetimes. On the basis of the FLID plot, we further extracted the state-averaged lifetime decays by selecting the experimental time bins belonging to each of the two identified state. The lifetime decay traces are well-fit to mono-exponential functions (Figure 5.3c), demonstrating that fluorescence in the bright and dim periods are each dominated by a single process.

The observed PL behavior, that is, fluorescence intensity blinking from the bright to dim state accompanied by shortened lifetimes, is often attributed to the charging and discharging of QDs, also referred to as A-type blinking (Figure 5.3d).[21, 26] In A-type blinking, emission from the bright and dim periods is assigned to the neutral (X) and charged exciton states respectively. The charged state in CdSe-CdS core-shell structures including DiRs has previously been identified as the negative trion (X^-).[115, 116] When a QD becomes charged, non-radiative Auger recombination—where the exciton recombination energy is transferred to an excess carrier—directly competes with radiative recombination of one of the electron and the hole, quenching both the PL intensity and lifetime.

Charging models also predict an increase in the rate of radiative recombination of the charged compared to the neutral exciton. This is because radiative rates in QDs increase with the number of carriers in the system.[117] In the trion state either electron can recombine with the hole and based on the observed scaling of multicarrier rates in QDs,[65] the radiative rate is predicted to increase two-fold. In order to estimate the scaling between the radiative rate of the bright and dim states, we use the following relationship to retrieve the radiative contribution, τ_r, to the PL lifetime, τ

$$I \sim \eta = \frac{k_r}{k_r + k_{nr}} = \tau k_r = \frac{\tau}{\tau_r} \tag{5.1}$$

where, I is the PL intensity, k_r is the radiative rate and k_{nr} is the non-radiative relaxation rate. We assume that the efficiency η of the bright state approaches unity. The assumption is based on previous measurements of near-unity quantum yields of the bright periods in core-shell QDs and similar findings in DiRs.[30, 116, 118] The estimated radiative lifetime of the bright ($\tau_{r,X}$ = 35.9 ns) and dim (τ_{r,X^-} = 18.2 ns) states correspond to a scaling of 1.97. The near two-fold increase is in excellent agreement with the expected scaling of the three-carrier trion state. We therefore ascribe the dynamics in this DiR to charging processes.

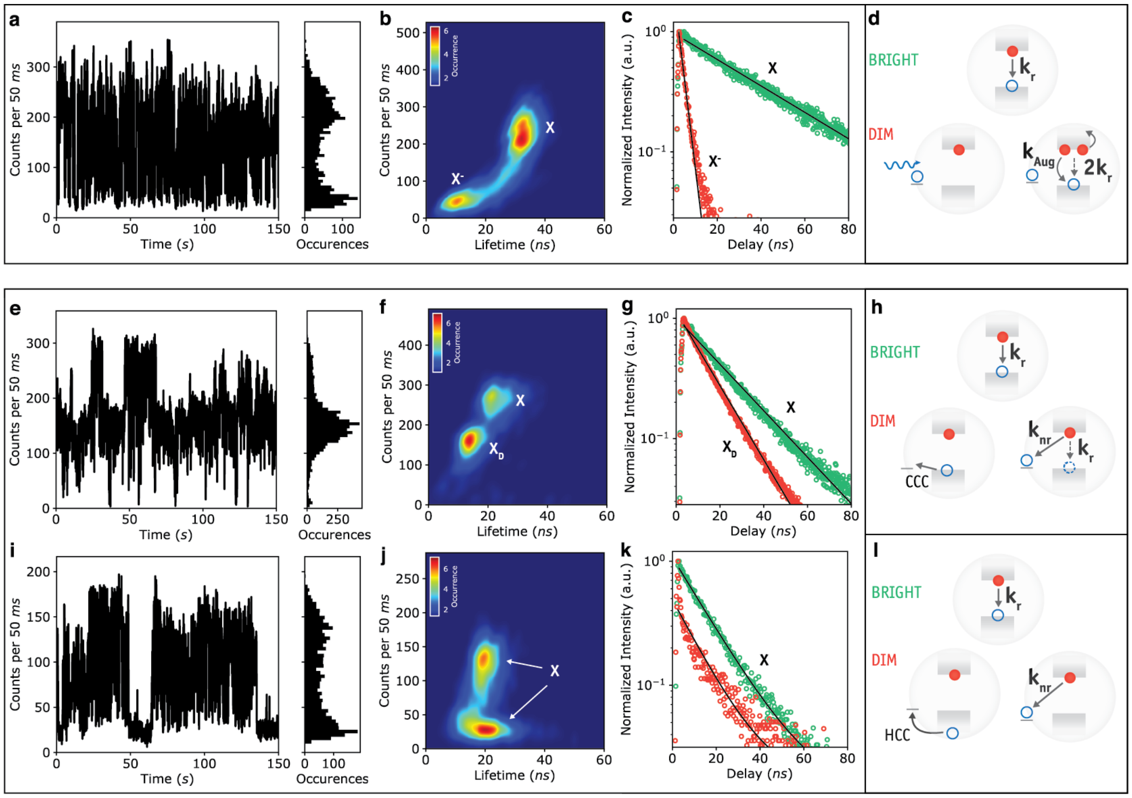

Figure 5.3: Exciton recombination dynamics in individual DiRs. Top panel: A-Type blinking - charging/discharging. Bottom panel: B-Type blinking - trap-assisted non-radiative recombination. (a) Time-dependent PL intensity trace (left) and associated intensity distribution (right). (b) Fluorescence lifetime-intensity distribution (FLID) plot for a DIR displaying A-type blinking. The FLID provides a convenient way to visualize PL intensity and lifetime fluctuations over long time scales. The color bar in the FLID represent the joint occurrence of each intensity-lifetime pair. (c) PL lifetime of each identified state. (e-g) and (i-k) presents the same data for two DIRs displaying B-type blinking (band-edge and hot-carrier capture respectively). (d) Mechanism for A-type blinking: The bright exciton (X) state is dominated by radiative recombination (k_r); in the dim charged exciton (X^-) state, Auger recombination (k_{Aug}) competes with radiative recombination and the radiative rate doubles ($2k_r$). (h,l) Mechanism for B-type blinking: Exciton (X) radiative recombination (k_r) is responsible for emission in the bright state; trapping of an excited carrier opens up a fast non-radiative channel (k_{nr}) in the dim excitonic (X_D) state. CCC = cold-carrier capture, HCC = hot-carrier capture.

5.3.2 B-type Quantum Dot-in-Rods

Figures 5.3e-g (bottom panel), present PL measurements on another DiR with a similar behavior as before—fluorescence blinking correlated with shorter lifetimes in the dim state. However, for this DiR, we estimated a one-to-one scaling between the radiative rate of the bright (X) and dim (X_D) state ($\tau_{r,X_D} \sim \tau_{r,X}$ = 23 ns). This observation is inconsistent with the charging model and indicates that recombination in the dim state involves a single electron and hole. In this scenario PL jumps are attributed to trap-assisted non-radiative processes in which the radiative rate of the exciton remains fixed but the non-radiative rate fluctuates in time.[28, 38, 119] This behavior is consistent with a model based on multiple recombination centers (MRC).[24, 25] In the MRC model, fluctuations in the non-radiative channel result from the opening and closing of non-radiative recombination centers that can capture band-edge electrons and holes. The non-radiative channels compete directly with radiative recombination of the band-edge exciton quenching both the PL intensity and lifetime (Figure 5.3h). We denote the dim state in this case simply as X_D since no additional charge carriers are involved.

A different PL signature emerges when the rate of carrier capture in the trap-assisted route is faster than the rate of cooling to the band-edge. PL spectroscopy on the DiR in Figures 5.3i-j (bottom panel), shows that intensity fluctuations can also be accompanied by minimal changes in the PL lifetime. The observed behavior, that has previously been referred to as B-type blinking, results from hot-carrier trapping[120] of electrons and holes that recombine non-radiatively before they relax into emitting states at the band-edge of the DiR (Figure 5.3l).[26] This process bypasses radiative recombination, reducing the PL intensity without affecting the PL decay dynamics. Instead the fluorescence observed in dim states is from unintercepted excitons that cool to the band-edge and recombine radiatively. Since both cold- (band-edge) and hot-carrier capture processes involve trap-assisted non-radiative recombination we collectively refer to them here as B-type blinking. We note however that intensity fluctuations originating from hot-carrier trapping was only distinguishable in two instances, therefore we focus primarily on the band-edge process.

5.4 Coexistence of A- and B-type Processes

Neither A- nor B-type mechanisms, that is, fluorescence blinking due to charging or trap-assisted non-radiative recombination, exclude the other. Several reports provide evidence that both can occur in the same QD.[22, 26, 27] This was also recently confirmed by Yuan *et al.*[28] using similar lifetime-scaling arguments. In some of the DiRs we also delineated contributions from both A- and B-type processes to the fluorescence intensity.

Figure 5.4a shows the time-dependent PL intensity trace of a DiR displaying both A- and B-type fluctuations. Three intensity states are highlighted. A bright exciton (green), charge (grey) and dim exciton (red) state. The FLID in Figure 5.4b demonstrates that the three states are mainly responsible for fluctuations in the PL intensity. The lifetime of each state was extracted by fitting each decay curve in Figure S3c to a single-exponential function. Using equation 1 we retrieved the radiative contribution to the lifetime of each state:

$$\tau_{r,X} = 28.9 \text{ ns}$$

$$\tau_{r,X^-} = 14.9 \text{ ns}$$

$$\tau_{r,D} = 29.8 \text{ ns}$$

The ratio of the radiative lifetimes is:

$$\tau_{r,X} : \tau_{r,X^-} : \tau_{r,D} \approx 1 : 2 : 1$$

The observed scaling is in agreement with our assignment and also confirms the existence of charging and trap-assisted non-radiative processes in the same DiR. Roughly 75% (n=28) of DIRs exhibited clear signatures of A-type transitions where as 49% (n=18) displayed contributions from B-type mechanisms. Our findings directly implicates both charging and trap-assisted non-radiative processes in mitigating PL efficiencies in the DiRs examined.

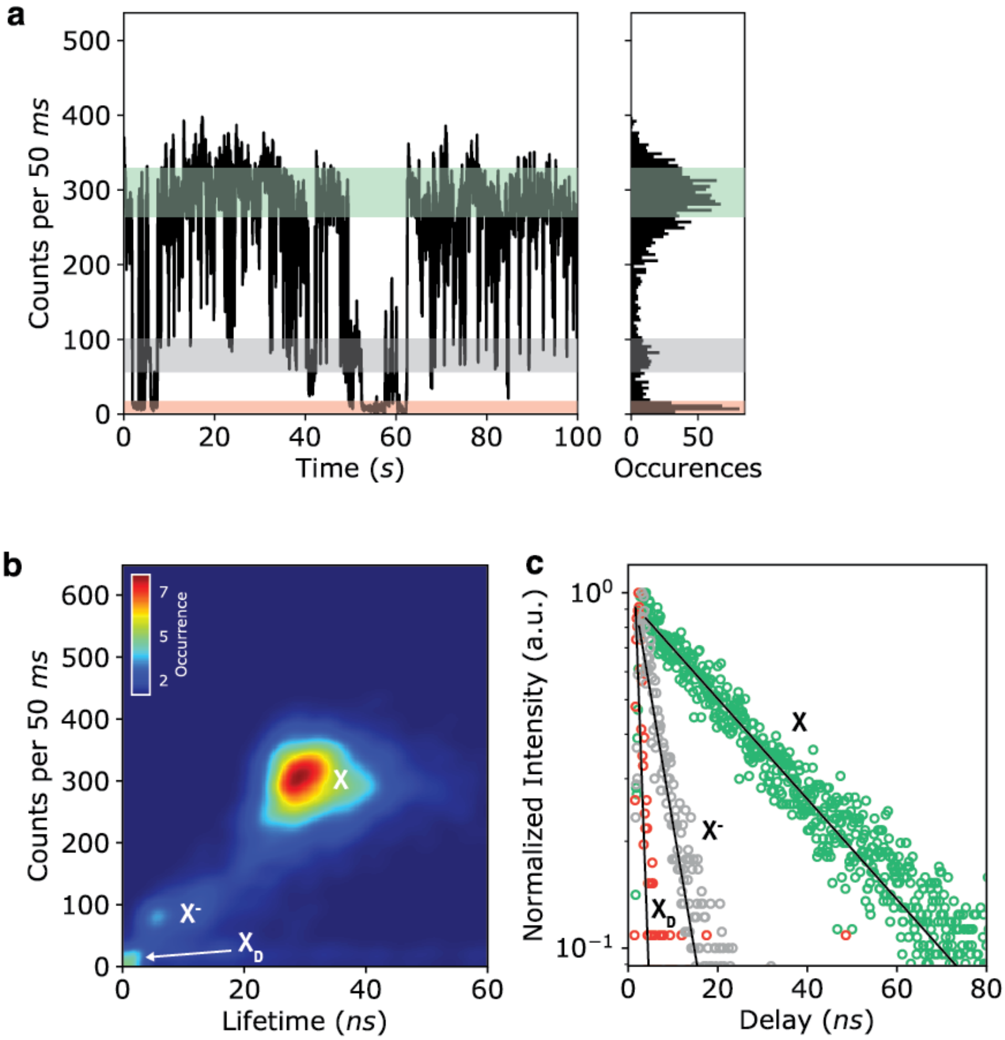

Figure 5.4: Coexistence of A- and B-type blinking in single DiRs. (a) Time-dependent PL intensity trace of a DiR displaying both A- and B-type intensity fluctuations. (b) Fluorescence lifetime-intensity distribution (FLID). (c) PL lifetime of each identified state.

5.5 Key Characteristics of the Observable Exciton States

Figure 5.5 summarizes key trends related to the observable excitonic states for all the DiRs investigated. In Figure 5.5a the correlation between the radiative lifetime of the exciton ($\tau_{r,X}$) and trion (τ_{r,X^-}) state is presented. Radiative decay in the charged trion state is faster on average by a factor of 1.9 ± 0.2 and is in good agreement with the scaling of radiative recombination in a three-carrier QD system. Figure 5.5b shows the correlation between the non-radiative Auger decay time in the charged state (τ_{Aug,X^-}) and the volume of the DiRs. Auger lifetimes were recovered using equation 1 and assuming that the Auger channel is the dominant non-radiative pathway in the charged state. The volume of the DiRs were estimated from the HAADF-STEM images of each nanorod. Auger recombination of an electron and hole is observed to slow in DiRs coated with a larger shell. This scaling of the non-radiative channel in the charged state with volume, often referred to as V-scaling, is another signature in favor of charging processes, as Auger rates are expected to vary with QD volume.[121] Several other factors related to the increase in the shell volume of the DiRs are known to affect Auger rates and may also contribute to the trend observed. These include: (1) an increase in the spatial separation between the core and the surface of the heterostructure, (2) a reduction of the electron and hole spatial overlap and (3) possible 'smoothing' of the confinement potential experienced by the extra charge carrier.[115, 121, 122]

Figure 5.5c presents the correlation between the radiative time of the bright and dim (τ_{r,X_D}) exciton related to trap-assisted non-radiative decay. The dim state was chosen as the lowest intensity period in the PL intensity trace. This state is typically referred to as the dark or off state and was discernible in all the DiRs displaying B-type fluctuations. In all cases the intensity period was emissive and above background (1.5 counts /50 ms). We see that the radiative time of this dim exciton is unchanged with an approximate one-to-one scaling of the radiative rate (0.91 ± 0.2). This scaling indicates that only one electron and hole are involved in the fluorescence from the dim state. Figure 5.5d shows the correlation

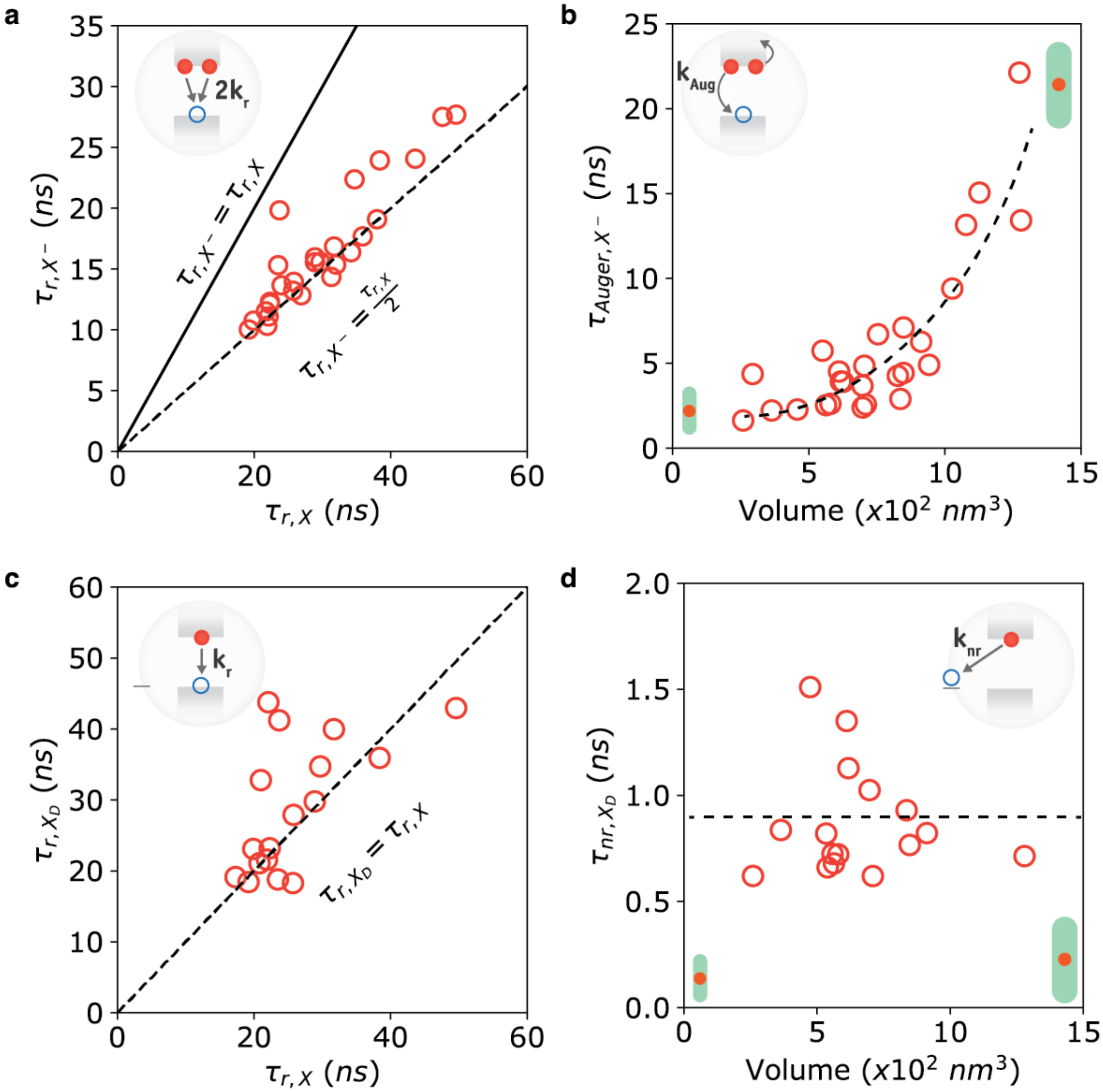

Figure 5.5: Summary of the characteristics of the charged (A-type) (X^-) and dim (B-type) (X_D) exciton state for all DIRs (n=37). (a) Correlation between the radiative lifetime of the neutral (X) and charged (X^-) exciton. Radiative decay in the charge state roughly doubles, increasing by a factor of 1.9 ± 0.2. (b) Auger lifetime (τ_{Aug,X^-}) of the charged state as a function of the volume of the DiRs. Non-radiative Auger rates slow with increasing shell volume of the DiRs. (c) Correlation between the radiative lifetime of the neutral (X) and dim (X_D) exciton. The radiative lifetime in the dim state remains unchanged, with a scaling of 0.91 ± 0.2. (d) Non-radiative decay time (τ_{nr,X_D}) of the dim state as a function of volume. Decay rates are uncorrelated with changes in volume.

between the non-radiate decay time of the dim exciton (τ_{nr,X_D}) and volume of the DiRs. The decay rate of the non-radiative channel of the dim exciton is uncorrelated to changes in the shell volume of the particles. The lack of a dependence of the non-radiative time on volume provides further support to B-type processes involving a single exciton.[22] In the presence of additional carriers one would expect to observe a similar trend as in the case of the charged trion state (Figure 5.5b). We note that the non-radiative decay time of the dim exciton is considerably shorter than Auger times in the charged state. As a result, the fluorescence of the dim exciton is sufficiently quenched below the level of the trion state in DiRs that display both A- and B-type transitions and the two states were readily distinguishable.

5.6 Role of Structure

Although the carrier relaxation channels in A- and B-type mechanisms are distinct from one another, the two processes are physically related. Both charging and trap-assisted models invoke the capture or transfer of excited charge carriers to defect-related traps.[24, 123] These acceptor sites are typically situated near or at the surface of QDs. In previous work, we provided direct evidence of the deleterious effects of these defects on QD photoluminescence, however, specific photo-physical mechanisms were not explored.[48] In order to investigate the role of structure on both A- and B-type processes in the DiRs studied here, we attempted to identify specific morphological and structural features tied to the low efficiency charged (X^{-}) and dim exciton (X_D) state. For this purpose, we examined the structures of predominantly charged and dim DiRs.

5.6.1 A-type Quantum Dot-in-Rods

The frequency of charging and dim state events was approximated as the fraction f of time over the course of the entire fluorescence measurement that a given DiR spent in each state. Figure 5.6a shows the time-dependent PL intensity trace and associated intensity distribution for a strongly charged DiR ($f(X^-) = 0.7$). The dotted red line represents the intensity threshold used to filter the charged state fluorescence. Evidently, the DiR resides predominantly in the low efficiency charged state. Such predominance of charging events was recently linked to low ensemble PL quantum yields in giant-shell QDs.[93] The FLID representation (Figure 5.6b) for the DiR also depicts this increased likelihood of sampling the low intensity trion state compared to the bright neutral exciton state.

Figure 5.6c shows a HAADF-STEM image of the structure of the DiR above. The intensity of the HAADF signal is proportional to the square of the atomic number (Z) of the core and shell elements and the thickness of the DiRs.[43] However, because of the small CdSe cores used, contrast is mainly from variations in the thickness of the CdS shell. On inspection of the morphology we see a fairly uniform deposition of the shell along the DiR with the exception of a region at the surface (indicated by the red box) in a direction perpendicular to the *c*-axis [001] of the wurtzite lattice. Figure 5.6d presents a false color image of this region. A dip in the thickness of the shell can clearly be seen indicating that uniform shell growth on top the CdSe core was interrupted.

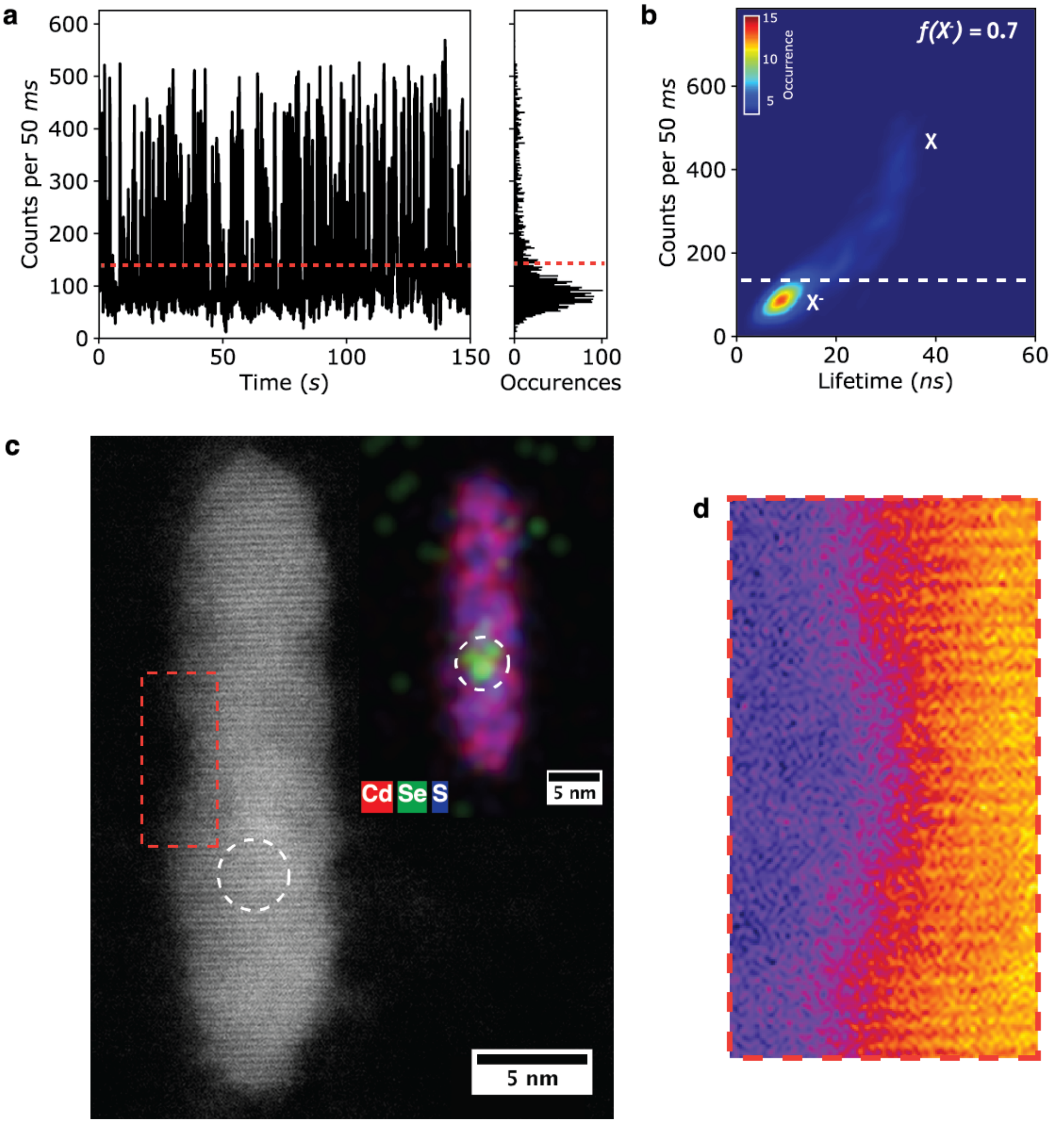

Figure 5.6: Charged DiRs. (a) Time-dependent PL intensity trace (left) and corresponding intensity distribution (right) of a strongly charged DiR. Dotted red line represents the chosen threshold for determining the degree of charging. (b) Associated FLID color plot, clearly showing that charged exciton (X^{-}) recombination DiR dominates the emission from the DiR. (c) High-resolution HAADF-STEM image of the same DIR, inset: spatially-resolved EDS chemical map of the heterostructure. Circle denotes the approximate location of the CdSe core. (d) Colorized micro-graph of defect region of the core-shell particle (red box) in (c).

Interestingly, in almost all charged DiRs ($f(X^-) \geq 0.5$, n=7) we were able to discern similar morphological variations in the thickness and distribution of the CdS shell (Figure 5.7a-f). This correlation directly associates increased shell roughness in the DiRs with the occurrence of charging events. The surfaces in these shell regions are likely poorly terminated and possibly associated with a set of traps attributed to dangling bonds and vacancies that can capture photo-generated electrons and holes and promote charging.[124, 125] In the future, full resolution of the atomic arrangement in these regions using aberration-corrected imaging techniques should facilitate a detailed characterization of the imperfections.[44] Similar morphological irregularities have been observed elsewhere and were connected to diminished ensemble quantum yields in DiRs.[126] The authors attributed poor shell deposition to the rapid growth rates that take place in conventional fast-injection growth schemes. Coropceanu *et al.* also showed that the surface quality and hence the quantum yield of the DiRs could be improved when a second slow shell growth step was introduced. Another possible source that could contribute to irregular shell growth may result from the relaxation of strain in the CdSe core above the critical shell thickness. Similar to planar heterostructures, strain relaxation in core-shell QDs has been suggested to lead to roughening at the surface.[127] Strain has also been connected to the formation of crystalline defects such as stacking faults in DiRs.[128] However, in the present study stacking faults were not observed, likely due to the small size of the CdSe core used.[128, 129]

It was useful to also consider the role of passivation of the CdSe core, if any, on the occurrence of charging in the DiRs. To delineate the position of the CdSe core within the CdS shell, we evaluated the chemical structures collected by STEM-EDS. The chemical map for the DiR, presented in Figure 4c (inset), clearly shows the location of the CdSe core. The approximate boundary of the core is indicated by the white circle. We see that the core is well passivated on all facets by the CdS shell and that the core position is uncorrelated to the irregular shell regions. A similar observation was made for the other charged DiRs as well (Figure 5.7a-f).

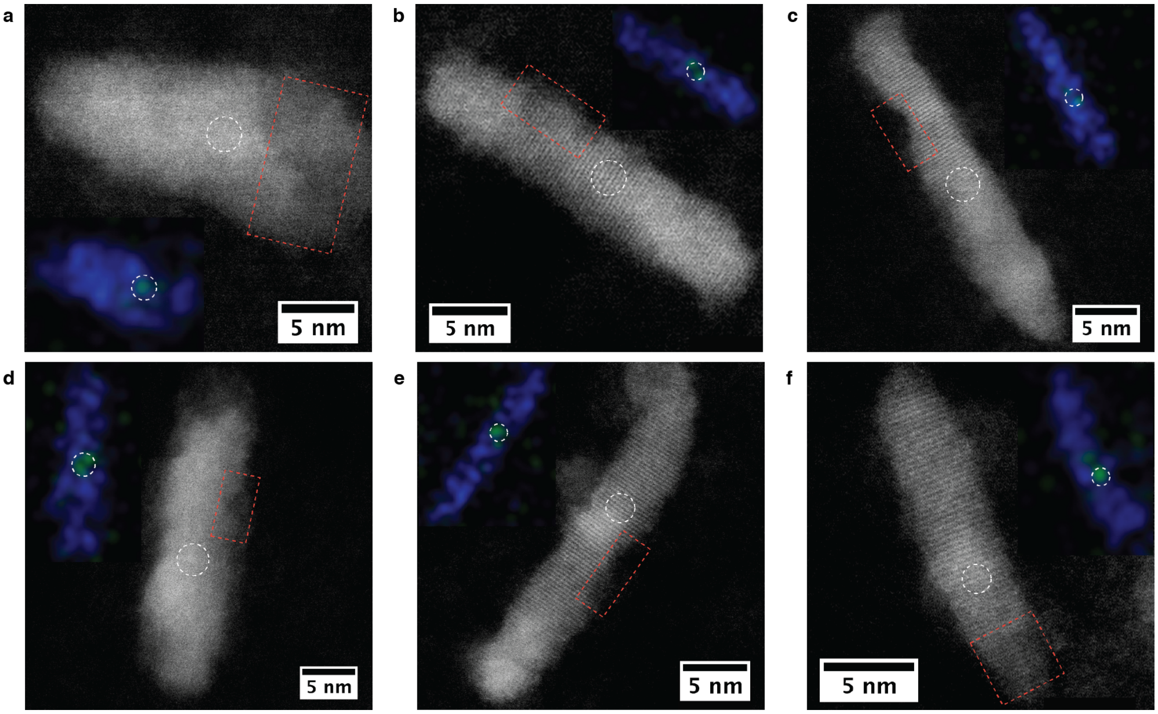

Figure 5.7: Additional charged DiR structures. (a-f) HAADF-STEM images of the DiRs. STEM-EDS chemical map in inset: blue (S), green (Se). Dotted box(red) outlines defect region of the DiRs. Dotted circle (white) denotes approximate location of the CdSe core.

5.6.2 B-type Quantum Dot-in-Rods

The same irregularities and imperfections were also observed in dim (B-type) DiRs (*n*=6). Figure 5.8a shows the time-dependent PL intensity trace for one of them ($f(X_D) = 0.6$). The predominance of emission from the dim exciton state is evident from the FLID plot in Figure 5.8b. The structure of the DiR is presented in Figure 5.8c. A dip in the thickness of a region of the CdS shell is highlighted (indicated by the circle). Otherwise, the shell appears mostly uniform. Interestingly, the location of the CdSe core (inset Figure 5.8c) is correlated to the position of the defect. A line scan of the DiR (Figure 5.8d) illustrates this point more clearly. Both the HAADF intensity profile of the DiR along the *c*-axis and the STEM-EDS Se signal from the core are overlaid in the line scan. A notable drop in the HAADF intensity, which corresponds to a large and sharp dip in the thickness of the CdS DiR, is located in the same region as the CdSe core. This indicates that the

CdSe core has minimal shell coverage or may have exposed surface atoms in this region.

Four of the other DiRs in the dim fraction also clearly exhibited defect shell regions that potentially expose or have minimally passivated core facets (Figure 5.9a-d). In general, the defects appear to localize more closely to the CdSe core in comparison to strongly charged DiRs. Previous work shows that the surfaces of CdSe QDs are characterized by stoichiometrically distinct facets.[130] Preferential epitaxial deposition of the CdS shell on Se-rich and chemically neutral facets of the core may explain the growth observed in dim DiRs. If core facets are indeed exposed, they are likely not completely bare as passivating organic ligands should provide some coverage. Organic passivation, however, typically results in low surface coverage and poor environmental stability, ultimately leaving some surface sites under-coordinated.[13] These unbonded surface sites introduce a distribution of localized sites capable of trapping charge carriers at the surface and, in this case, facilitate trap-assisted non-radiative recombination as indicated from analysis of single DiR time-resolved fluorescence.

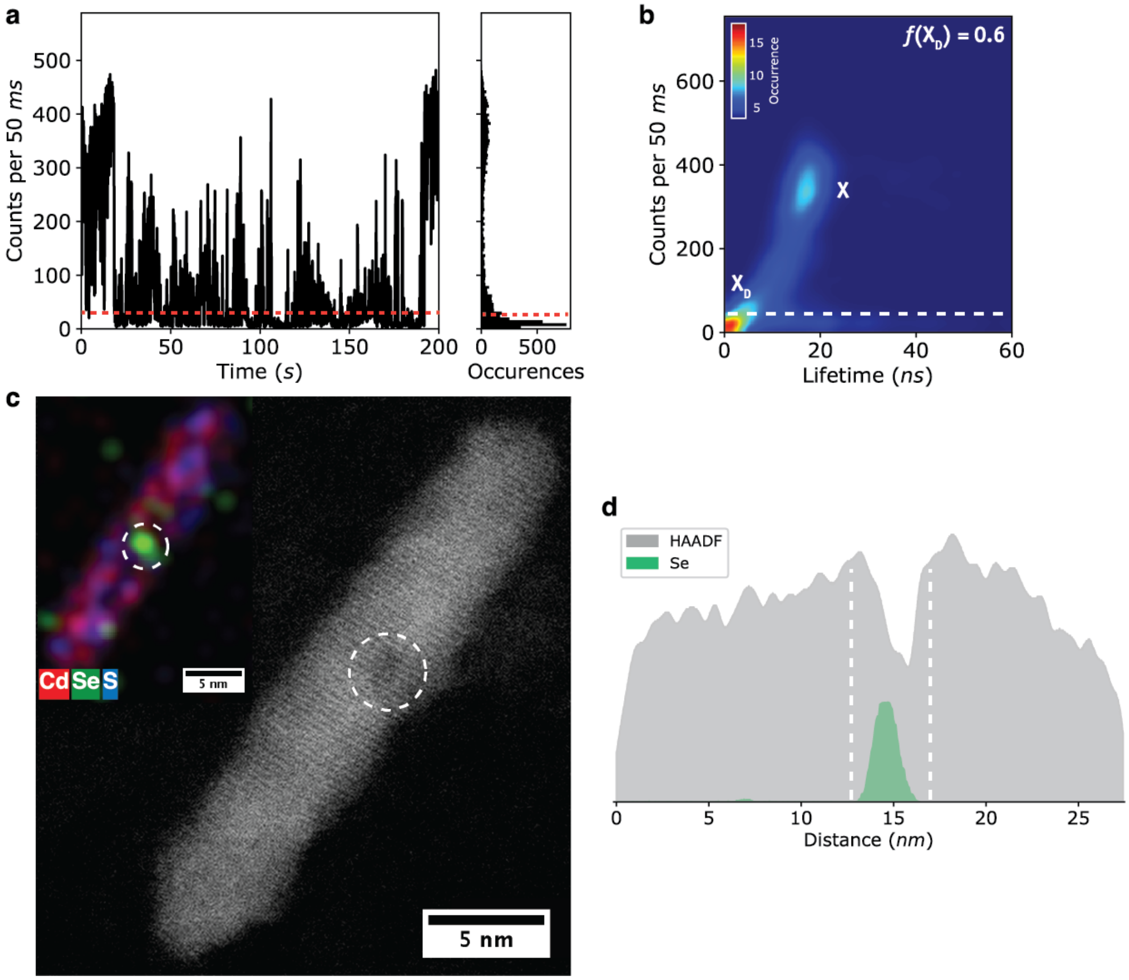

Figure 5.8: Dim DiRs.(a) Time-dependent PL intensity trace (left) and corresponding intensity distribution (right) of a DiR displaying strong B-type behavior. Dotted red line represents the chosen dim state threshold. (b) Associated FLID, showing that a dim exciton (X_D) state dominates the recombination dynamics of the DiR. (c) High-resolution HAADF-STEM structure of the same DiR, inset: spatially-resolved EDS chemical map of the heterostructure. Circle denotes the location of the CdSe core. (d) Intensity profile of the particle in c along the *c*-axis overlaid with the STEM-EDS Se signal, highlighting shell defect within core region of the DiR.

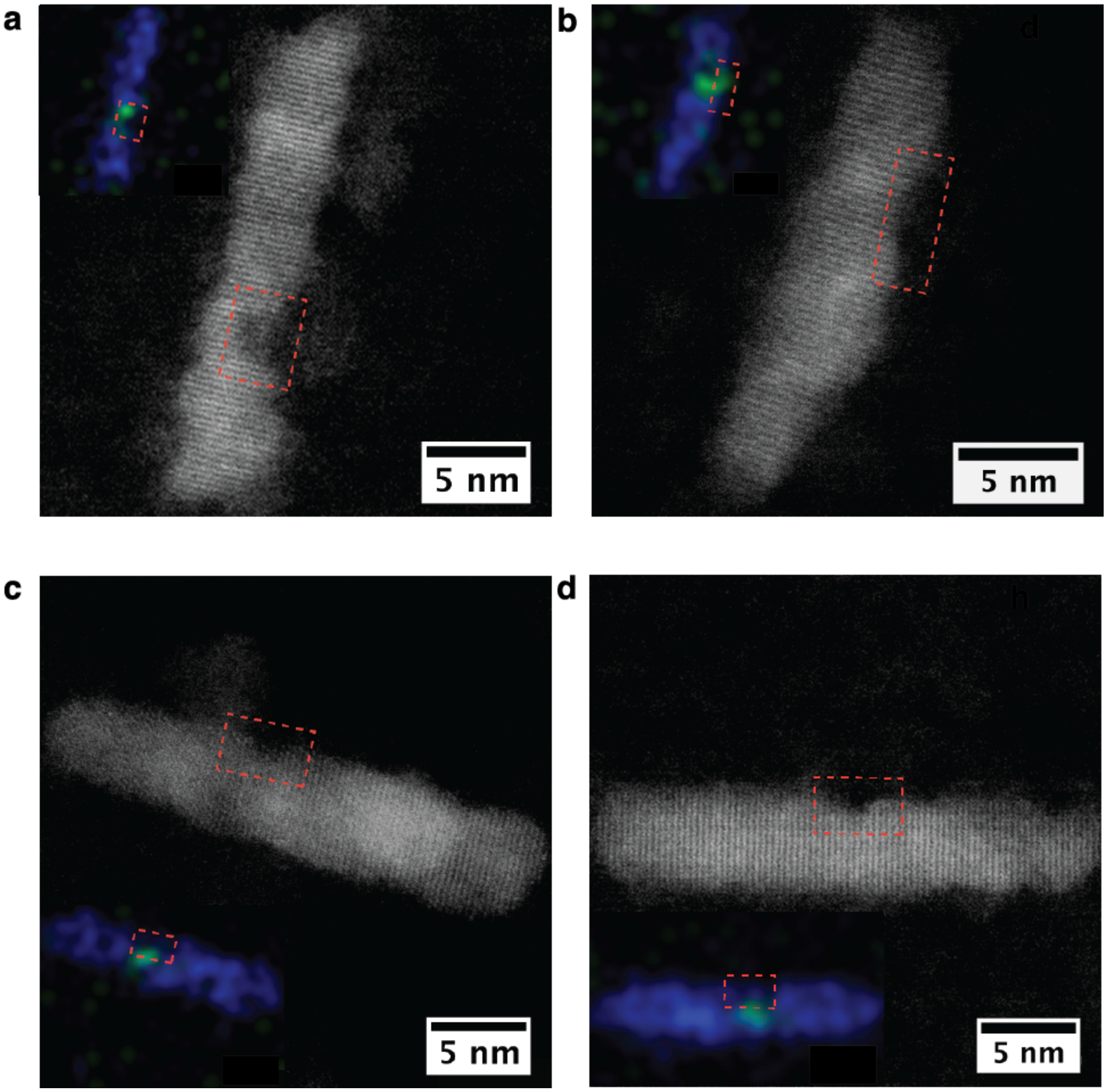

Figure 5.9: Additional dim DiR structures. (a-d) HAADF-STEM images of the DiRs. STEM-EDS chemical map in inset: blue (S), green (Se). Dotted box(red) outlines defect region of the DiRs.

5.6.3 High Efficiency Quantum Dot-in-Rods

Unsurprisingly, in contrast to strongly charged or dim structures, DiRs with high efficiencies of the radiative channel (display minimal blinking) had good structural integrity. Representative structures are presented in Figure 5.10. FLID plots (Figure 5.10a,d,g) show that excitons generated in the DiRs primarily undergo radiative recombination—both A- and B-type non-radiative channels are suppressed. The structures of the DiRs feature crystalline shells and a notable absence of shell regions with high surface roughness (Figure 5.10b,e,h). Additionally, the CdSe cores of the DiRs are completely passivated by the inorganic CdS shell (Figure 5.10c,f,i). We remark that defects are likely still present in these structures but at low densities—unresolvable from visual inspection—explaining their high efficiencies. Nonetheless these results further confirm the structural dependence of A- and B-type processes in DiRs.

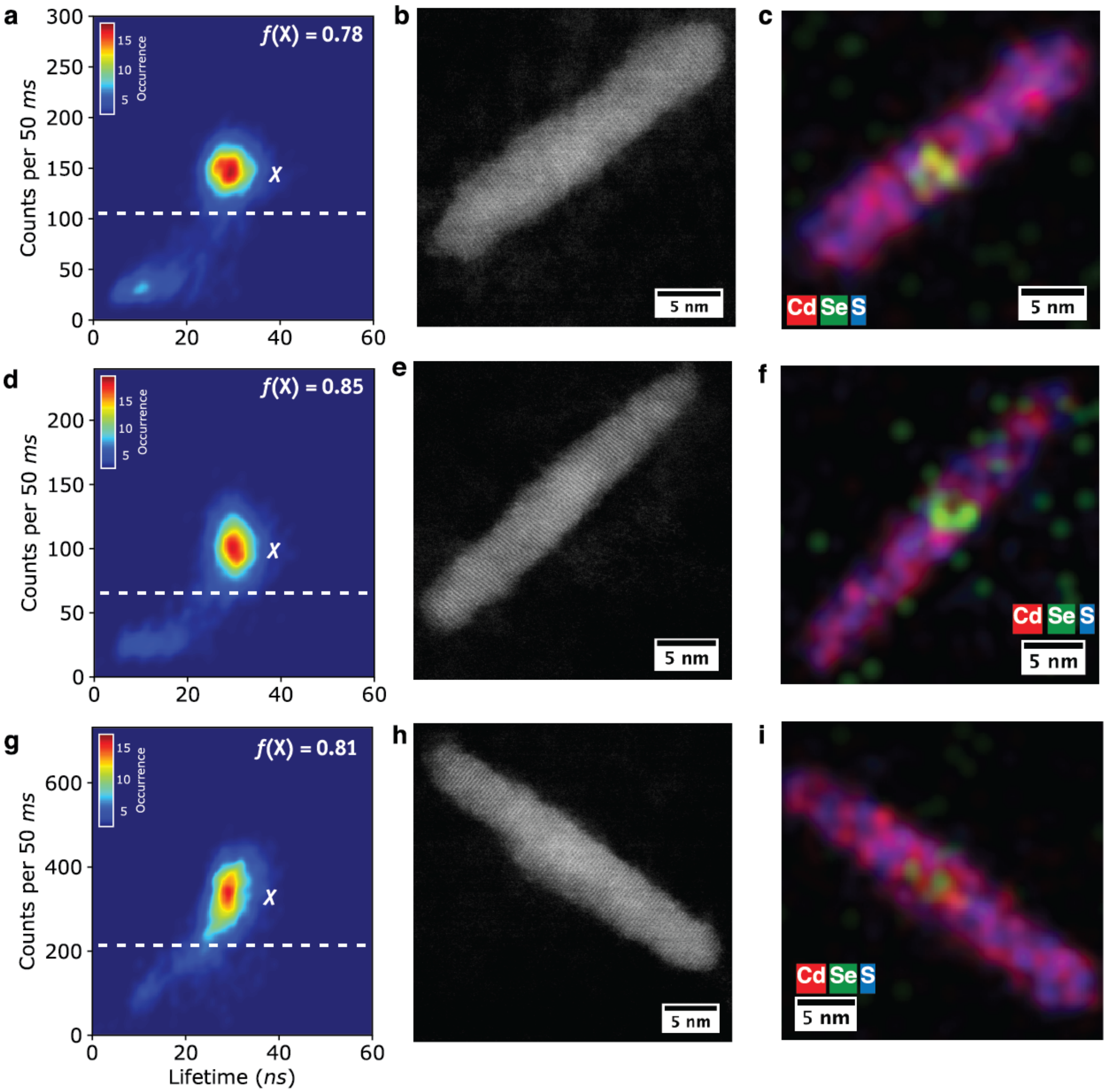

Figure 5.10: Bright DiRs. (a,d,g) FLID color plot, (b,e,h) high-resolution HAADF-STEM images and (c,f,i) spatially-resolved EDS chemical maps for three representative high efficiency DiR. The FLIDs show that radiative exciton recombination (X) dominates the fluorescence of these DiRs. Structurally, the DiRs feature crystalline shells and a notable lack of highly irregular shell regions.

5.7 Implications

Interestingly, we observed distinct structural features that influence A- and B-type non-radiative exciton processes in individual DiRs. The potential defects that trigger both mechanisms are correlated to irregular surfaces of the DiRs. However, in charged structures the associated trap sites are localized at the outer surface of the CdS shell and further from the photo-active CdSe core. In dim structures the traps may be situated at the core surface or separated from the core by a thin inorganic shell layer. In any case the surface acceptor sites are situated in closer proximity to the core of the DiRs. These observations indicate that the separation between the core and trap sites at the surface play an important role in governing the likelihood of A- and B-type transitions.

This idea becomes more intriguing upon further contemplation of each process. In A-type blinking, when a photo-generated carrier is transferred to an acceptor site, the resulting trap (charge-separated) state—where one carrier is localized in a trap site and the other remains delocalized—is long-lived.[123] Subsequent excitation creates another electron-hole pair that must recombine in the presence of an additional charge and opens the Auger channel. Recovery of the neutral (uncharged) exciton state occurs when the trapped carrier returns to the QD core or otherwise recombines with the excess carrier. In contrast, in B-type processes, trap states are short-lived and relax non-radiatively before the next excitation event—leaving a neutral QD behind.[24] In this view, the occurrence of charged state (A-type) recombination then depends on the time-scale of recovery of the trap state. Therefore, one can envision the existence of trap sites that either promote charging or support trap-assisted non-radiative recombination.[131]

Although the dynamics of charge-carrier trapping and trap state recombination in QDs are not fully understood, charge-separated states are known to exist in QDs over a wide dynamic range, spanning femtosecond to millisecond timescales.[85, 132] In fact, trap states may be involved in the majority of emission events from some QD nanostructures.[133–137] Distributions in the lifetimes of trap states in QDs have been motivated in several ways but are mainly thought to reflect the coupling between the trapped carrier and remaining delocalized charge as well as the presence of activation or tunneling barriers between QD states and trap sites.[123, 131, 138] These factors are in turn influenced by the location and also the nature of the trap sites involved.

As it pertains to the nature of traps, trap sites characterized by different electronic energies, for example, have been linked to changes in trap state lifetimes in QDs.[138, 139] In this picture, large potential barriers for recovery from an energetically deep trap give rise to long-lived trap states whereas energetically shallow traps recover on shorter timescales. Indeed, shallow and deep traps have been suggested as a possible source of A- and B-type blinking in QDs.[28] Dynamic fluctuations in the energy of a single trap site that are associated to light-induced conformational changes may also contribute long- and short-lived trap states.[36, 140] In addition, the chemical origin of trap sites has been suggested to influence coupling to the QD states and may also determine the preferred recovery channel of trap states.[141, 142] While we cannot rule out the possibility of these effects; the trap sites in the DiRs studied here likely have similar origins and energetic dynamics. As holes constitute the predominately trapped carrier in cadmium chalcogenide nanocrystals, we suspect that trap sites are mainly situated at S shell surface atoms and possibly Se sites in the case of DiRs that may have partially unpassivated CdSe cores. Both trap sites have been shown, for example, to have similar energetic depths.[141, 143]

Now taking into account the location of trap sites, as demonstrated from structural interrogation of the DiRs, traps are located at different distances from the CdSe core of the DiRs. Differences in spatial proximity likely influence coupling strengths between the trap sites and the CdSe core states and therefore the lifetime of trap states. Early blinking models, for example, suggest that a wide range of trap state recovery rates could result from distributions in back-tunneling rates of the trapped carrier that vary exponentially with the distance of trap sites around a QD emitter.[144] Perhaps more interesting, recent transient absorption experiments on CdS and CdSe nanorods by Utterback *et al.*[145, 146] indicate that surface-trapped holes recombine with delocalized electrons in the bulk of the rod on timescales that depend on the spatial overlap of the wave function of the electron and trapped hole. Slow recombination times were attributed to diffusion of trapped holes that weakly overlapped with delocalized electrons in the nanorods. Faster trap state recovery times were observed in cases where the wave function of the electron and trapped hole remained spatially coupled. These results support our observations in strongly charged and dim DiRs. Additionally, the proposal of slowly diffusing trapped holes implies that carriers do not have to be localized very far from the DiR core to generate long recovery times that trigger charging processes. Distance-related coupling involving trap states may also explain observations in other QD nanostructures, such as the shell thickness dependence of A- and B-type blinking reported by Galland *et al.* in spherical shell QDs.[26] In the future atomistic simulations of DiRs may unravel the exact mechanisms of recovery of trap states and the influence of spatial coupling on recovery times.[147, 148]

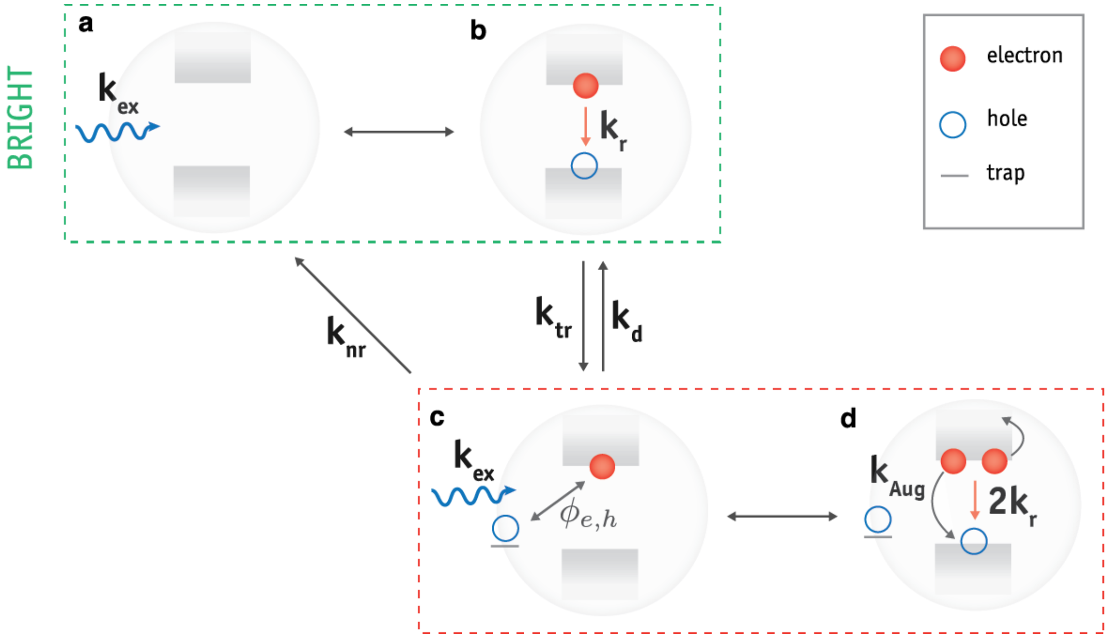

Figure 5.11: Description of exciton recombination dynamics in DiRs incorporating distance-related coupling. (a) When a DiR is excited, radiative recombination (k_r) of the generated exciton dominates the high efficiency channel. (b) Alternatively, one of the generated carriers may be captured by a trap site at the surface of the particle with a trapping rate (k_{tr}) that depends on the density and accessibility of the traps. (c) The lifetime of the trap state depends in part on the spatial overlap (coupling) of the wave function of the trapped and remaining delocalized carrier. If the photo-excitation rate (k_{ex}) is greater than the rates of recovery of the trap state (k_{nr} and k_d: detrapping rate), the particle becomes charged and (d) non-radiative Auger decay (k_{Aug}) dominates the recombination dynamics. When the trap states are short-lived the PL is quenched predominantly *via* trap-assisted non-radiative processes (k_{nr}).

In Figure 5.11 we present a simple model summarizing the dynamics of exciton recombination in DiRs incorporating observations from our correlative investigation. Following photo-illumination of the DiRs an electron-hole pair is generated. This occurs predominantly in the CdS shell, given the energy (3.1 eV) of the excitation source. Both the electron and hole can localize in the CdSe core and recombine radiatively. Alternatively, one of the generated carriers may become captured at a charge-trapping center at the surface, creating a charge-separated trap state. After sometime T, the separated carriers may recover the band-edge exciton state and recombine radiatively. As noted, diffusive motion and tunneling of the trapped carrier have been invoked to explain recovery of the trap state.

In addition to radiative exciton recombination, non-radiative relaxation channels are also accessible to the separated carriers—possibly *via* movement of the delocalized carrier to the surface of the DiR. If recovery from the trap state is slower than the excitation rate, then a second generated electron-hole pair has to recombine in the presence of an excess charge, triggering Auger processes (A-type) that compete with radiative exciton recombination. On the other hand, if the recovery time is on the order of the excitation rate, the charging channel is blocked and trap-assisted non-radiative decay (B-type) becomes the dominant non-radiative relaxation channel. While changes in the distribution and dynamic fluctuation of trap energies have been suggested to explain variations in the recovery times of trap states, our observations indicate that trap state lifetimes are also connected to the spatial coupling of the trapped and delocalized carriers.

5.8 Conclusion

To our knowledge the optical, structural and chemical information presented in this work represents the most complete description reported for a single DiR core-shell nanostructure. Using time-resolved single QD fluorescence spectroscopy we found two non-radiative exciton processes responsible for moderating photoluminescence efficiencies in DiRs: charging (A-type) and trap-assisted non-radiative (B-type) processes. This observation is in agreement with previous studies that indicate that a combination of the two mechanisms account for fluorescence blinking in QDs.[26, 28]

Direct correlation of the structures of the DiRs with their fluorescence show that A- and B-type processes are both linked to increased roughness at the surface of the nanostructures. Further, we show that spatial proximity of the surface irregularities to the core of the DiRs influences the likelihood of charging or trap-assisted non-radiative recombination. We remark that the asymmetric structure of the DiRs facilitated clear visualization of the surface imperfections under structural imaging conditions. However, these defects are not restricted to DiRs, thereby extending the proposed mechanism to other QD nanostructures. For example, thick spherical shell QDs exhibit shell-thickness variations but these can be difficult to visualize due to the large shell volume.[93] Our work highlights surface roughness as a crucial parameter when designing QD nanostructures with specific excitonic fates.

5.9 Experimental Methods

Materials

Selenium powder (99.99%) and cadmium oxide (99.99%) were purchased from Strem Chemicals Inc. Trioctylphosphine (TOP, 90%), trioctylphosphine oxide (TOPO, 99%), and sulfur, were purchased from Sigma-Aldrich. HPLC grade toluene was purchased from Fisher Scientific. Octadecylphosphonic acid and hexylphosphonic acid were purchased from PCI Synthesis. All chemicals were used without further purification unless otherwise noted.

Synthesis of CdSe Nanoparticles

Preparation of Se Precursor: In a glove box, Se (0.058 g, 0.734 mmol) was added to a 1 dram vial containing TOP (0.430 mL, 0.964 mmol) and a stir bar. The Se was dissolved with heat and stirring. Prior to injection, the optically clear, colorless solution was drawn into a 10 mL polypropylene syringe with an 18 gauge needle and plugged into a septa for removal from the glove box.

In a typical synthesis, TOPO (3.0 g, 7.76 mmol), ODPA (0.28 g, 0.84 mmol), and CdO (0.06 g, 0.47 mmol) were added to a 25 mL three-neck round bottom flask equipped with a stir bar, two rubber septa, condenser, and inlet adapter attached to a schlenk line. The mixture was degassed at 150 °C under vigorous stirring for 1 hour. The reaction was then flushed with Ar and heated to 310 °C where the CdO dissolved to form an optically clear, colorless solution. TOP (1.8 mL, 4.03 mmol) was injected into the flask, and the reaction was heated to 380 °C. The heating mantle was removed and replaced by an evaporating dish. As the temperature fell past 370 °C, the Se precursor was injected. The flask was immediately sprayed with acetone until the temperature fell below 200 °C, and 10 mL of toluene were injected. The solution was split between two 6 dram vials and particles cleaned *via* three successive crashes using ethanol as an anti-solvent and toluene for particle dispersion (centrifugation for 5 minutes at 4400 rpm).

Synthesis of CdSe-CdS DiRs

Preparation of Seed/Sulfur Precursor: Sulfur (0.06 g, 1.87 mmol) was added to a 1 dram vial, followed by 8 x 10^{-8} mol of CdSe seeds, as determined by the absorbance of the stock seed solution at the first absorption peak.[71] The solution was evacuated and flushed with Ar 3 times on a schlenk line, and then TOP was added (1.8 mL, 4.03 mmol). The sulfur was dissolved with vortexing.

In a typical synthesis, TOPO (3.0 g, 7.76 mmol), ODPA (0.29 g, 0.67 mmol), and CdO (0.075 g, 0.584 mmol) were added to a 25 mL three-neck round bottom flask equipped with a stir bar, two rubber septa, condenser, and inlet adapter attached to a schlenk line. The reaction was degassed at 150 °C for 30 minutes. The flask was then flushed with Ar and heated to 355 °C. A clear, colorless solution was observed. TOP (1.8 mL, 4.03 mmol) was injected and the temperature was allowed to recover. The aluminum foil was removed and cotton wrapped around the glass wool (cotton was necessary for quick temperature recovery, but was watched closely as it was an inherent fire hazard). The reaction was allowed to equilibrate for 5 minutes past the cotton swaddling. The seed/sulfur solution was then quickly injected into the flask. Temperature recovery above 350 °C was observed within 90 seconds of injection. After 6 minutes of growth time, the heating mantle was removed and reaction allowed to cool. At 100 °C 10 mL of toluene was injected. The solution was split between two 6 dram vials and precipitated *via* three successive crashes using ethanol as an anti-solvent and toluene for particle dispersion (centrifugation for 5 minutes at 4400 rpm).

Sample Preparation

In a typical sample preparation, 1 micron sized polystyrene latex spheres (fiduciary markers) was drop-cast onto silicon dioxide support grids (Ted Pella, PELCO 8 nm Ultra-Flat Silicon Dioxide Support Film) and the excess suspension wicked away with a KimWipe®. Subsequent to the polystyrene deposition a dilute solution of DiRs ($\sim$ 1 nM) dispersed in hexanes was drop-cast onto the grid and allowed to dry. The prepared grid was placed face down on a quartz substrate and mounted onto a home-built inverted optical microscope. The polystyrene beads and grid bars of the support film were used for recording positional information on a CCD camera.

Single QD Fluorescence Spectroscopy

A home-built confocal microscope modified from Dukes *et al.*[49] was used to investigate the optical properties of single DiRs. The excitation source was a 405 nm PicoQuant pulsed diode laser with a repetition rate of 2.5 MHz. The average excitonic occupancies per pulse, $\langle N \rangle \sim 0.2$, was estimated from the absorption cross-section of the DiRs ($\sigma_{abs} \sim 10^{-13}$ cm^2 at 405 nm).[149] The polarization of the laser was rendered circular using a quarter-wave plate to ensure uniform excitation of the DiRs. The beam was then reflected from a 420 nm long pass (LP) dichroic filter (Omega Optics, 3RD410LP) into an inverted objective (Olympus UPLSAPO, apochromatic, water immersion, 1.2 N.A., 60x) and brought into focus at the sample. Fluorescence from the focal region was collected by the same objective, passed through the dichroic filter and was focused through a 150 um aperture onto two single photon avalanche photodiodes (SPAD, Micro Photon Devices $PD-050-0TC) in a Hanbury-Brown Twiss interferometric configuration. In this setup photons emitted from individual QDs were recorded with a series of tags using a time-correlated single photon counting (TCSPC, Picoharp 300) unit.

All analysis including the generation of the FLIDs was done with custom routines written in the Python programming language.

Electron Microscopy

After all relevant fluorescence data had been collected; support films were stored in a grid holder and transferred to an electron microscope. Scanning transmission electron microscopy images were obtained using a Tecnai Osiris operating at 200 kV, with a spot size set to 10 (to reduce charging effects) and a camera length of 220 mm for HAADF imaging. HAADF-STEM imaging was chosen over HRTEM imaging since the white-on-dark-contrast for STEM greatly facilitates the location of individual quantum dots at low magnifications. Patterns of polystyrene were used to align the STEM image and distances measured from the optical microscope were used to identify regions of interest. After obtaining a high resolution STEM image of a particle, the spot size was lowered to 4 yielding $\sim$ 1.5 nA of beam current with a probe size on the order of 0.5 nm. These conditions, in conjunction with a highly efficient Super-X EDS detection system, enabled rapid collection of EDS spectrum maps with a minimal number of scans ($\sim$ 30 s total acquisition time). EDS hypermaps were collected using Bruker's Esprit 1.9 software.

Chapter 6

Conclusion

In this work, the need for a comprehensive understanding of the interplay between the physical structure and photophysics of QDs was demonstrated by a set of experiments carried out on several QD nanostructures. Throughout, we reflect on how the inherent complexity of QDs and the heterogeneity of colloidal QD samples warrant the assembly of tools to examine QDs one by one in order to parse and decode this information. In particular, the illustrated strategy for the correlation of single QD optical and structural properties is exceptionally valuable for establishing detailed structure-property connections. It is anticipated that continued effort to unravel precise relations between synthesized QD structures and expressed behaviors using this approach will further challenge and advance our understanding of these nanostructured materials. Applied to QD design, insights acquired will in turn provide a clear road map for the development of synthetic schemes to completely tune and optimize the performance of QD nanostructures. This achievement would truly unlock the technological benefits of QD nanostructures.

6.1 Overall Conclusions

In Chapter 3, the optical properties of single CdSe-CdS QD nanostructures with a built-in anisotropic biaxial strain were investigated. The high quantum yield of the synthesized structures and use of strain to achieve a high spectral purity in ensemble, reflect the ingenuity of chemists to design tailored nanostructures—a feat made possible by the strong connection between QD physical structure and optical behavior and also by advances in synthetic control. Single QD optical measurements demonstrated that the spectral line widths of individual QDs were reduced two-fold compared to conventionally synthesized structures where the built-in strain is uniformly applied. This supported the hypothesis that narrow single QD lineshapes of the anisotropically strained QDs were responsible for narrow ensemble PL peaks as opposed to an unusually high structural uniformity of the QD sample. The detection and collection of the PL from single biaxially strained QDs was also instrumental in revealing appreciable heterogeneity in the sample otherwise masked in measurements performed in ensemble. The apparent divergence in measured single QD optical properties suggests that the synthesis of the QDs maybe further refined to achieve an optimized sample. It also signals that an in-depth understanding of the structural factors responsible for the heterogeneity in optical performance of QDs is crucial in order to guide rational improvements in synthetic methodologies.

Work in Chapter 4 demonstrated the development of environmentally stable InP-ZnSe core-shell QD structures as a 'greener' alternative to prototypical CdSe-based QDs, such as those studied in Chapters 3 and 5. A slow, high temperature shell growth procedure was used to grow a thick ZnSe shell and control the uniformity at the surface of the QDs. Optical spectroscopy on individual InP nanostructures showed that blinking of the PL can be strongly suppressed—attributable to the presence of a voluminous shell that restricts interactions of excited carriers with the surrounding environment and a uniform surface morphology. The achieved blinking suppression—and improved PL efficiency—is a key step in enabling InP based QDs for application in challenging biological settings such as particle tracking. However, despite successful growth of a large protective shell, the optical measurements on single InP heterostructures, also reveal variable levels of QD-to-QD blinking suppression. Additionally, the ensemble PL quantum yield of the sample was low. Structural characterization of the sample revealed morphological defects in the shell of a subpopulation of QDs, indicating a potential structural factor limiting the performance of the QD nanostructures. With this new chemistry, future endeavors to establish direct relations between the structural and optical properties of the InP QDs *via* correlation at the single QD level is expected to provide valuable feedback to further advance the development of this non-toxic material.

Finally, work presented in Chapter 5 details the use of a recently developed strategy to establish such structure-property relationships at the single QD level. The technique uses unique polystyrene formations as placement markers such that the position of individual nanostructures can be precisely determined in both optical and electron microscopes. This facilitates instrument relocation and fast acquisition of correlated measurements of optical and structural information from the same colloidal QD. The approach is simple, unambiguous, reproducibly and can be used to investigate the interplay between structure and function in a range of colloidal nanostructured systems. Applied to CdSe-CdS quantum dot-in-rods (DiRs), this technique enabled the identification of surface roughness as a crucial structural factor to consider when engineering QDs with specific excited state outcomes. Specifically, by directly correlating the atomic and chemical structure of individual DiRs with time-resolved optical measurements on the same structures, morphological imperfections at their surfaces, detrimental to PL efficiency were determined. It was further observed that the proximity of the surface irregularities to the core of the core-shell QD nanostrucutures influenced the excited state behavior—providing key mechanistic insight into exciton recombination. This study also demonstrates the utility of the correlation approach to inform material improvements. Control over the surface morphology of QDs is an often overlooked factor that presents unique opportunities to tailor the performance of QDs.

6.2 Future Direction

6.2.1 Correlation of Cadmium-free InP QD Nanostructures

It would be advantageous to utilize the single QD correlation methodology to study the InP QDs developed in Chapter 4. In addition to variably shell roughness between individual structures, advanced structural and chemical imaging of the sample revealed that indium from the InP core is distributed into the shell in some structures—possibly *via* a cation exchange with zinc in the ZnSe shell. A recent report by Talapin *et al.*[150] indicates that such an exchange likely creates structural disorder in the InP lattice by introducing interstitial point defects (e.g. vacancies) that mitigate PL quantum yields and broaden emission lineshapes. However, at the same time alloying maybe necessary to grow large uniform shells by minimizing lattice strain at the core-shell interface. Using the correlation strategy, the potential effect of compositional alloying and surface morphology variations on the optical performance of the InP QD core-shell nanostructures can be explored in greater detail. Understanding these effects could potentially inform synthetic methods to improve the optical properties of the material. However, a foreseen challenge in obtaining the related correlation data is that a significant fraction of the thick-shell InP core-shell QDs are prone to photobleaching under standard single QD optical excitation flux—despite a general enhancement in photostability afforded by the thick-shell growth. Furthermore, the electron beam in STEM is known to quench the fluorescence of QDs. As a result, in order to carry out this correlation, it is necessary to record the QD structure after the optical data is acquired. Consequently, if the damage sustained by the QDs results in any appreciable structural change, the acquired electron micrographs may differ from those of the native structure. In order to further improve the stability of the InP core-shell nanostructures, the growth of a thin secondary ZnS is proposed. ZnS has been shown to be more photostable[80] than ZnSe and can be grown epitaxially due to the relatively low lattice mismatch (3.4%) between the two materials.[11]

6.2.2 Advancing the Structural Characterization of QD Nanostructures

The single QD structural and optical correlation utilizes STEM to capture the structure of QDs which provides several distinctive advantages to conventional TEM methods. However, as presently implemented the technique suffers inherent aberrations—in particular, spherical aberrations (C_s)—that limit the detail with which QD structures can be acquired. Implemented with an aberration corrected microscope, structures maybe elucidated with full arrangement of their atoms.[43] An understanding of the precise crystal and surface structure of individual QDs would facilitate a thorough description of the effects of subtle structural variations on single QD optical properties. For example, in Chapter 5, it was unclear if increased morphological roughness was associated with the presence of atomic vacancies or dangling bonds at the surface of the QD nanostructures as a result of the limited resolution of the STEM micrographs. By revealing the atomic scale nature of the surface, aberration-corrected STEM may address this quandary. Even so, it should be noted that STEM is a projection technique in which valuable information is lost in one direction (i.e., in the direction of the electron beam). Instead, a three-dimensional (3D) atomic structure characterization of QD nanostructures should yield additional structural insights. Fortunately, with advances in image processing it is now possible to reconstruct a high quality 3D structure of a QD from a tilt series of STEM micrographs.[151] Once constructed, important information such as volume, surface roughness and core location could be accurately measured. This structural detail is invaluable in work towards a deeper understanding of QDs.

6.2.3 Enhancing Single QD Spectroscopy Capabilities

Along the same line, the single QD spectroscopic methods could be augmented to expand the utility of the correlation methodology. For example, while single QD studies are typically conducted at room temperature, operating at cryogenic temperatures would enhance the detail of many spectroscopic signatures by eliminating excited state phonon interactions.[16] This gives the possibility of revealing QD properties otherwise obscured in room temperature measurements. In addition, spectroscopy of single QDs has so far primarily benefited the study of QD nanostructures emitting in the visible where detectors with high quantum efficiencies are readily available. However, recent advances in single-photon detectors and CCD technology should expand the reach of the correlation to cover QD materials emitting in the near-infrared. These materials can be routinely synthesized with superior quantum yields[152] in comparison to their organic dye counterparts and are of great interest in applications such as biological imaging of deep tissue.[153] It is expected that single QD correlation studies will benefit further development and widespread use of these infrared QD nanostructures.

Appendix A

Structural, Chemical and Optical Data for Studied CdSe-CdS Core-Shell Quantum Dot-in-Rod Nanostrutures

What follows are all the structural, chemical and optical data acquired for the DiRs presented in the work in Chapter 5.

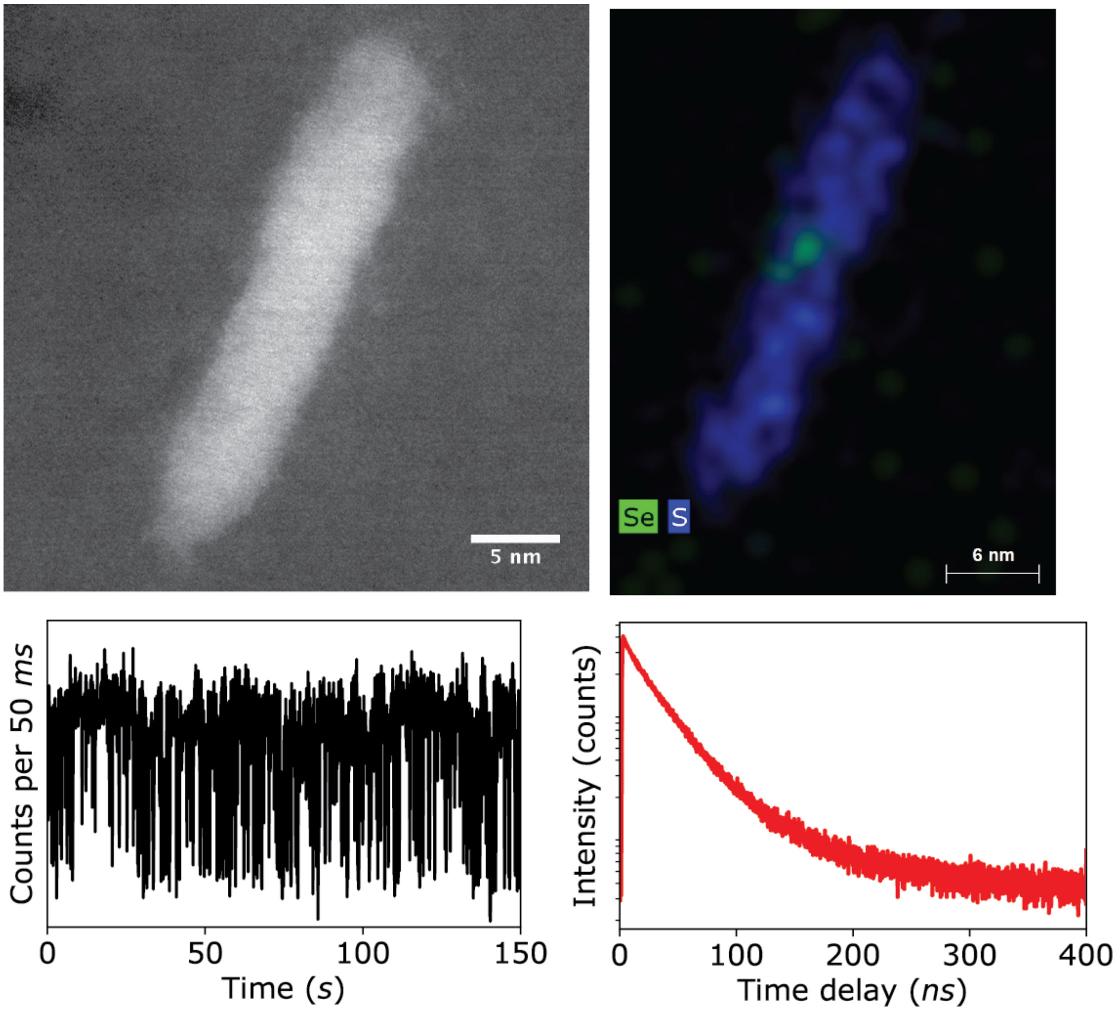
5 nm
Se
S
6 nm
Counts per 50 *ms*
0
50
100
150
Time (*s*)
Intensity (counts)
0
100
200
300
400
Time delay (*ns*)

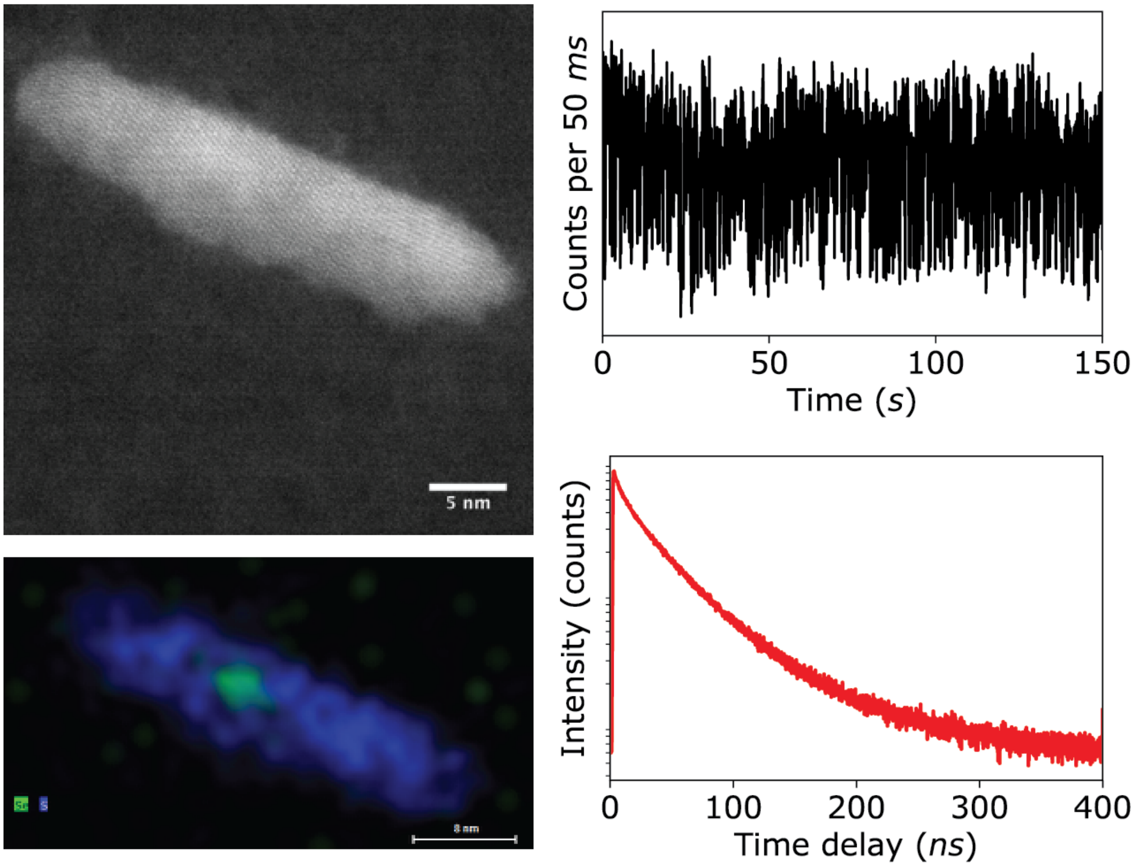
5 nm
Sn
S
8 nm
Counts per 50 ms
Time (s)
0
50
100
150
Intensity (counts)
Time delay (ns)
0
100
200
300
400

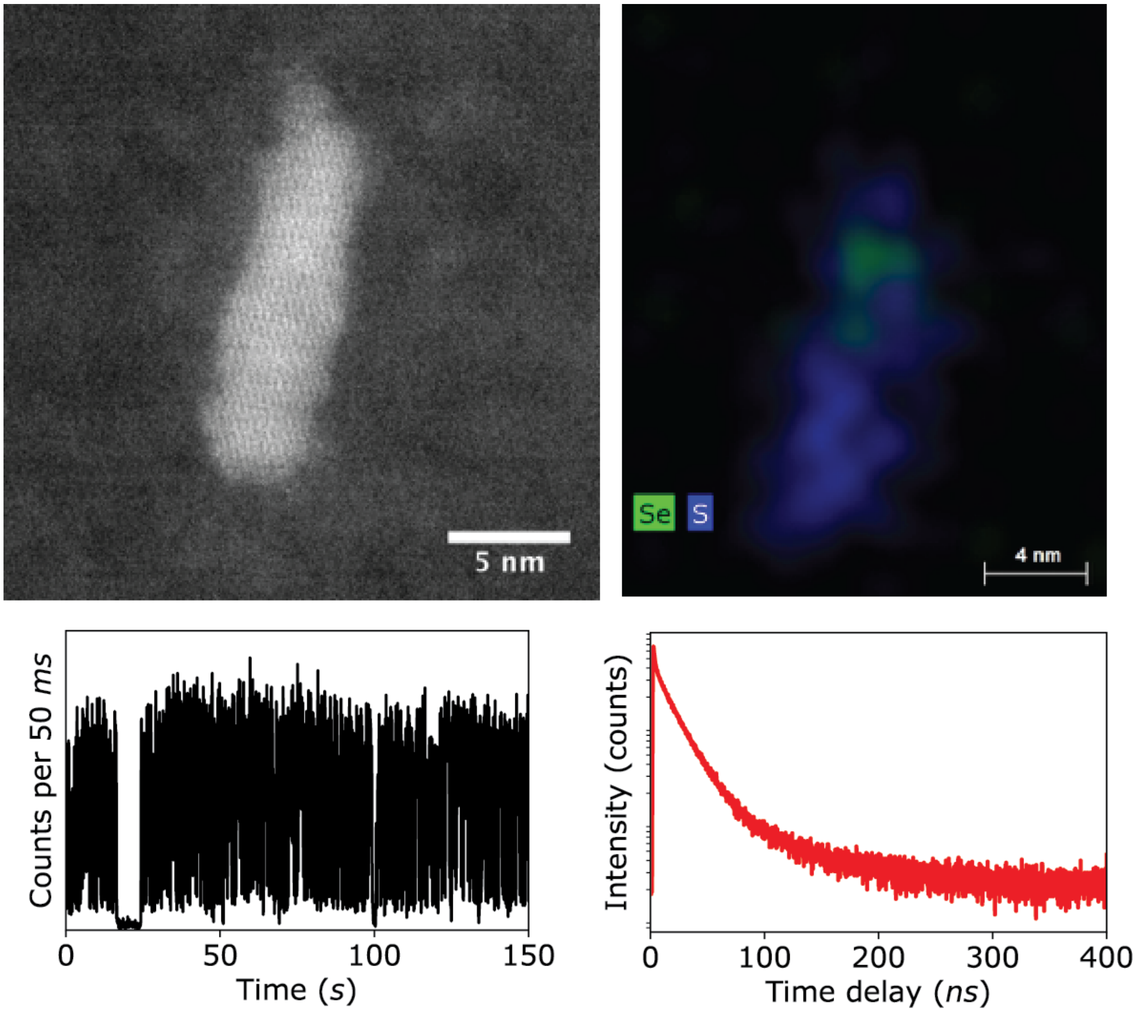
5 nm
Se
S
4 nm
Counts per 50 ms
0
50
100
150
Time (s)
Intensity (counts)
0
100
200
300
400
Time delay (ns)

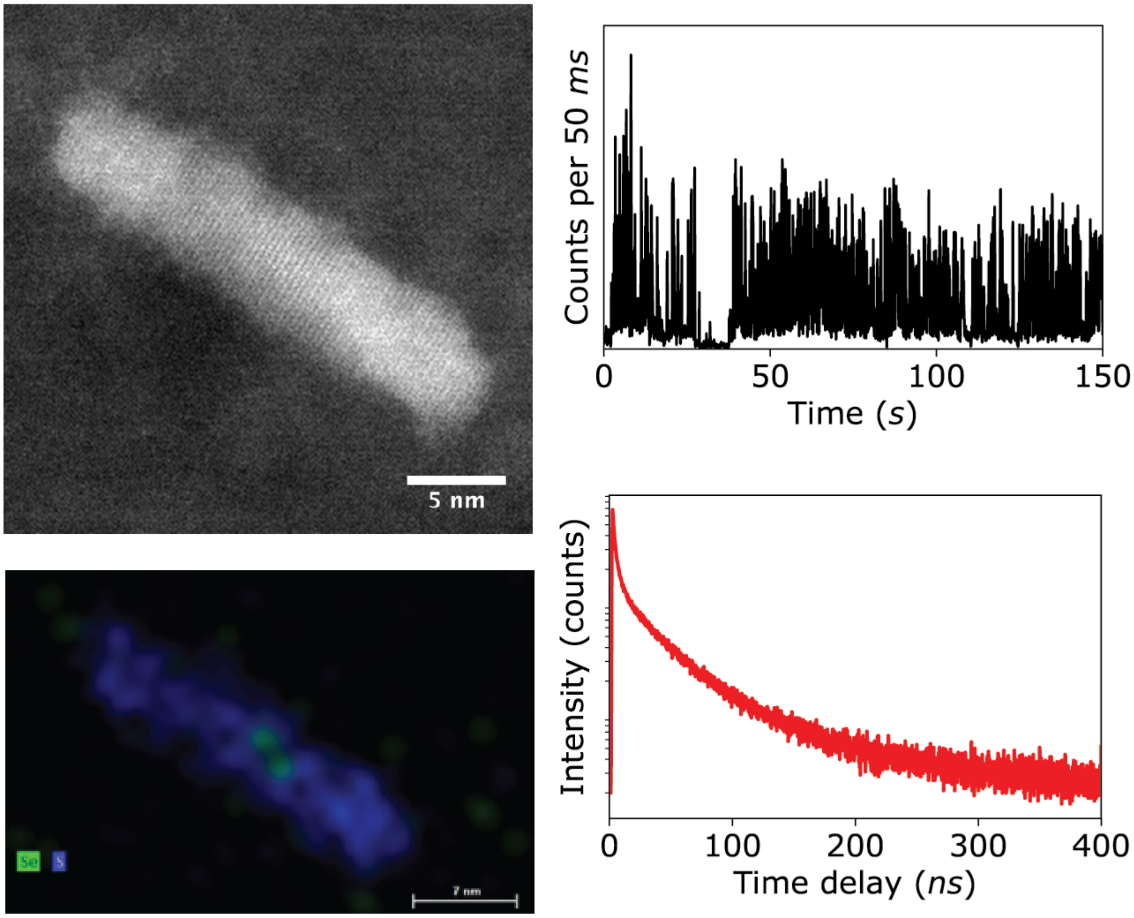
5 nm
Se
S
7 nm
Counts per 50 ms
Time (s)
0
50
100
150
Intensity (counts)
Time delay (ns)
0
100
200
300
400

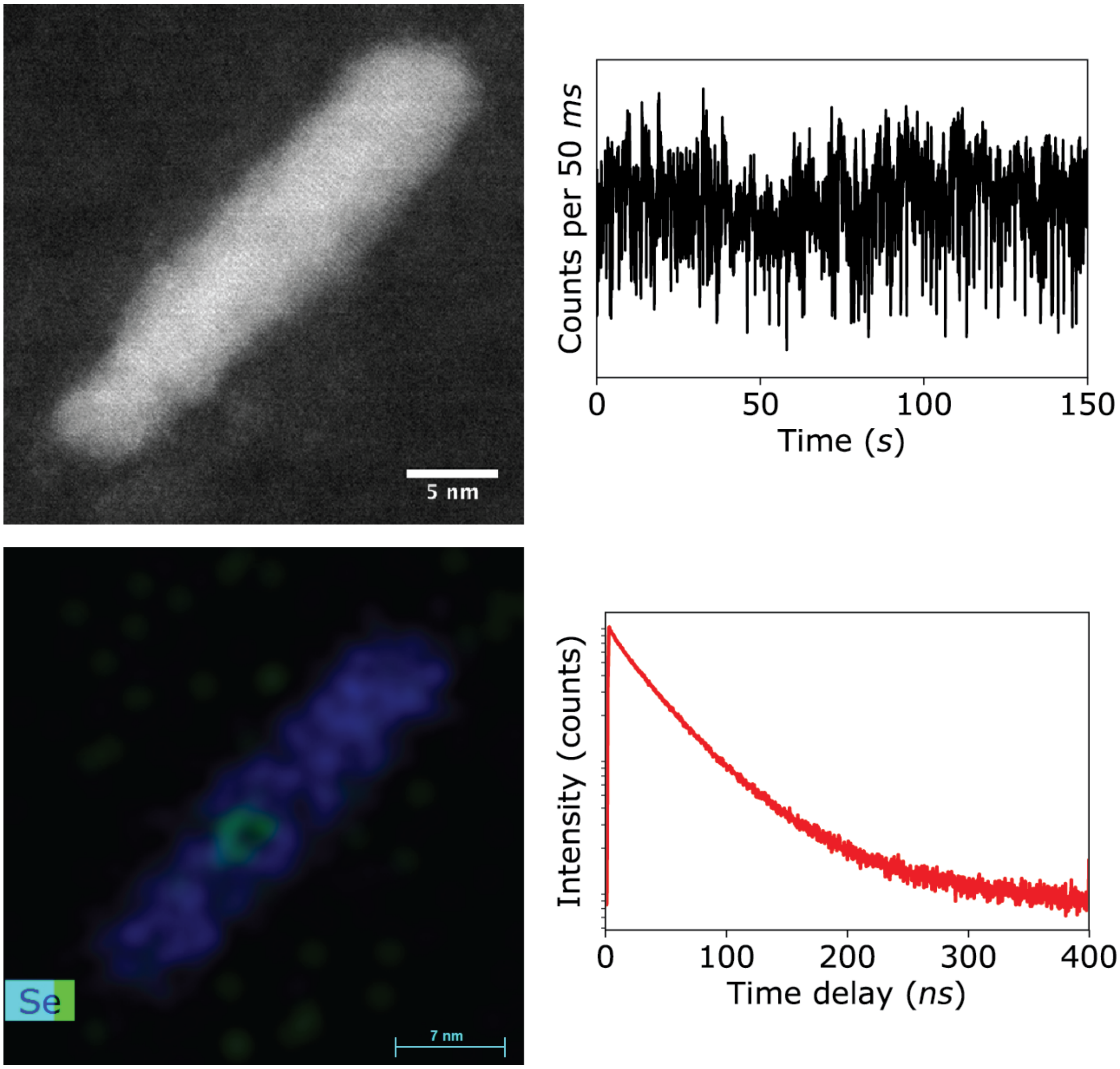
5 nm
Counts per 50 *ms*
0
50
100
150
Time (*s*)
Se
7 nm
Intensity (counts)
0
100
200
300
400
Time delay (*ns*)

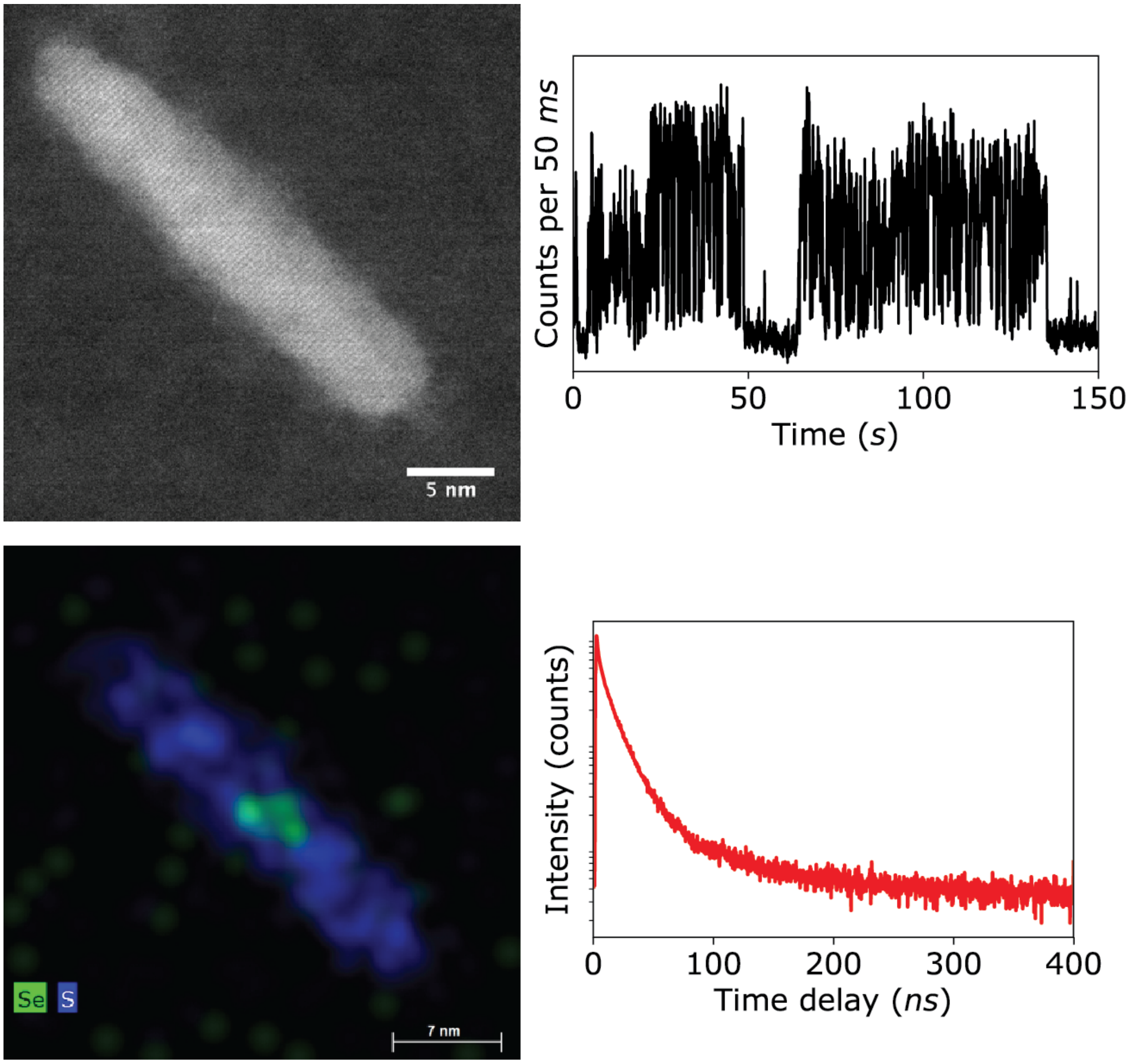
5 nm
Counts per 50 ms
0
50
100
150
Time (s)
Se
S
7 nm
Intensity (counts)
0
100
200
300
400
Time delay (ns)

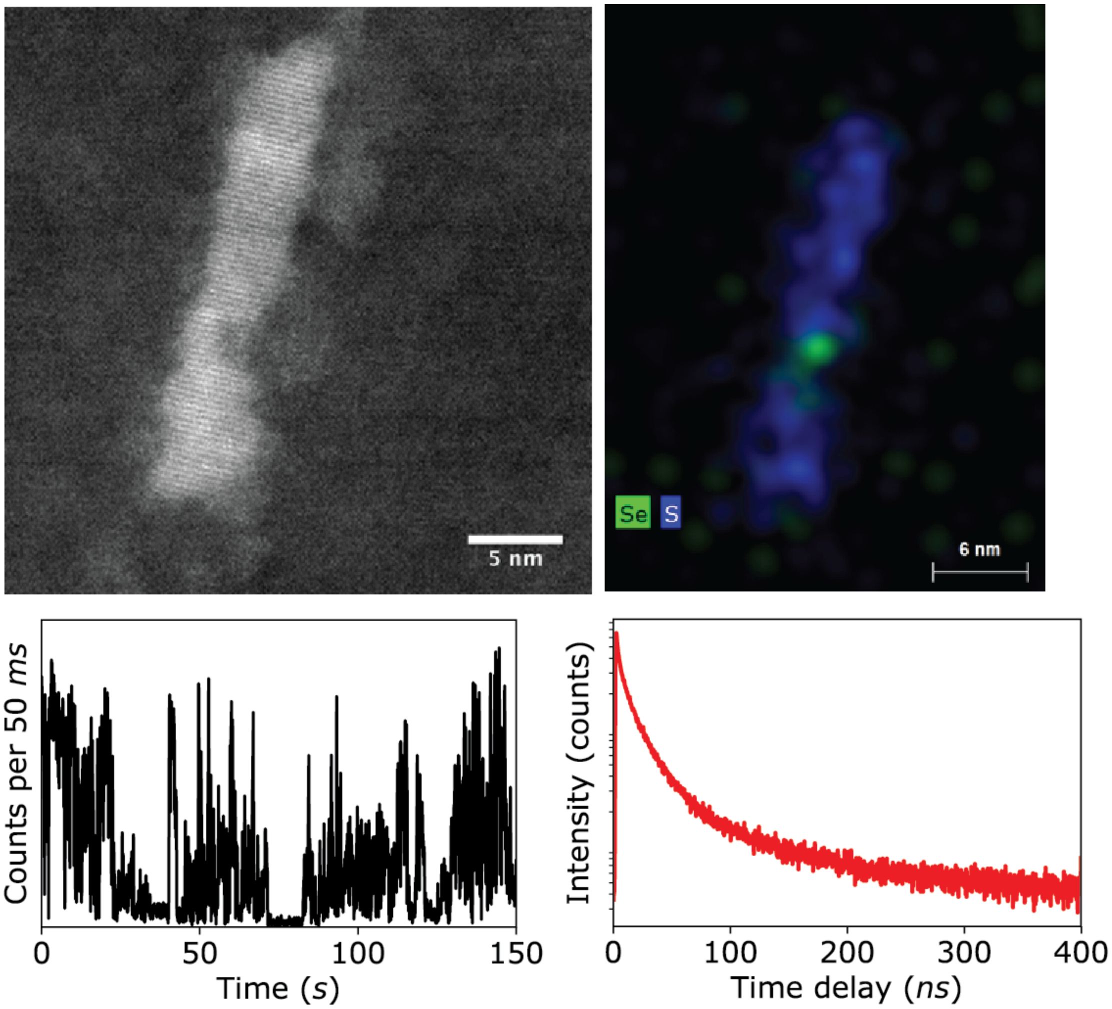
5 nm
Se
S
6 nm
Counts per 50 ms
0
50
100
150
Time (s)
Intensity (counts)
0
100
200
300
400
Time delay (ns)

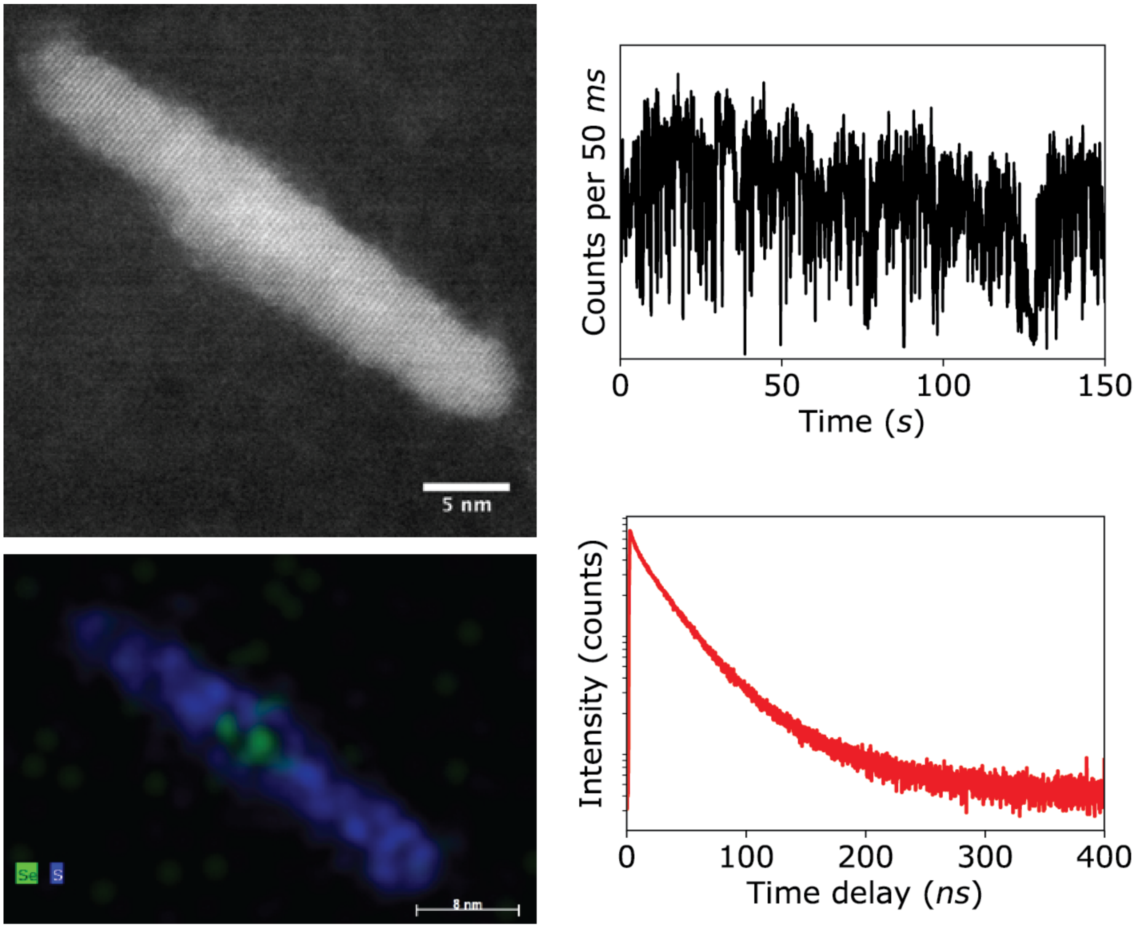
5 nm
Se
S
8 nm
Counts per 50 *ms*
Time (*s*)
0
50
100
150
Intensity (counts)
Time delay (*ns*)
0
100
200
300
400

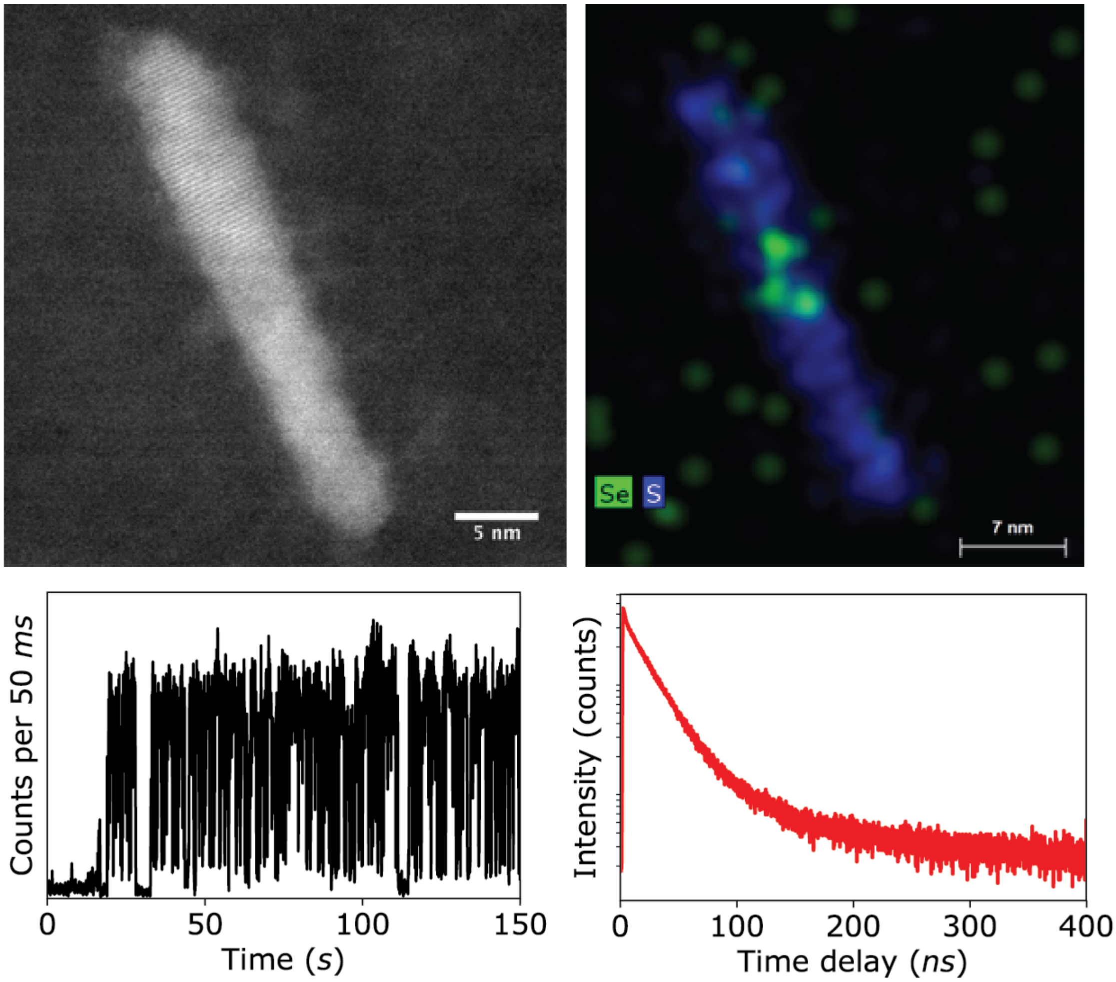
5 nm
Se
S
7 nm
Counts per 50 *ms*
0
50
100
150
Time (*s*)
Intensity (counts)
0
100
200
300
400
Time delay (*ns*)

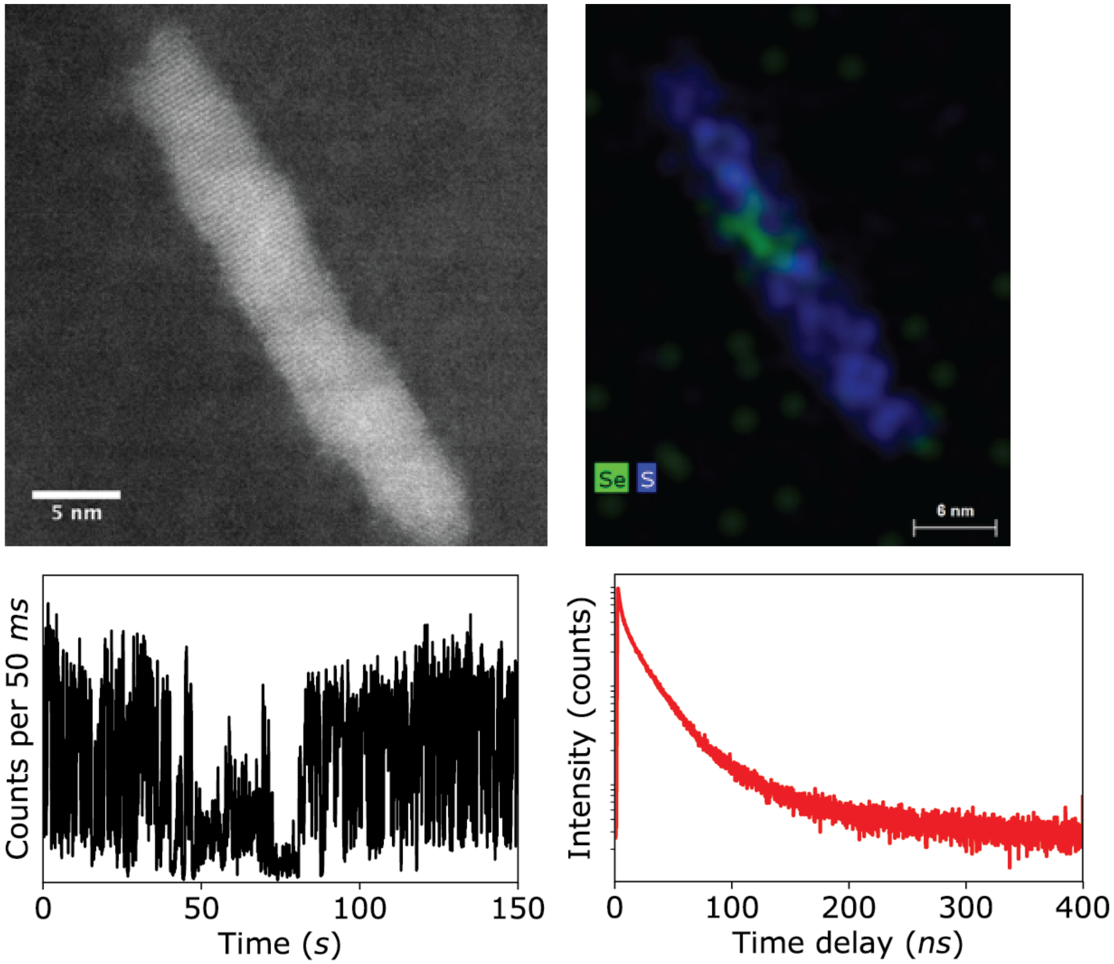
5 nm
Se
S
6 nm
Counts per 50 *ms*
0
50
100
150
Time (*s*)
Intensity (counts)
0
100
200
300
400
Time delay (*ns*)

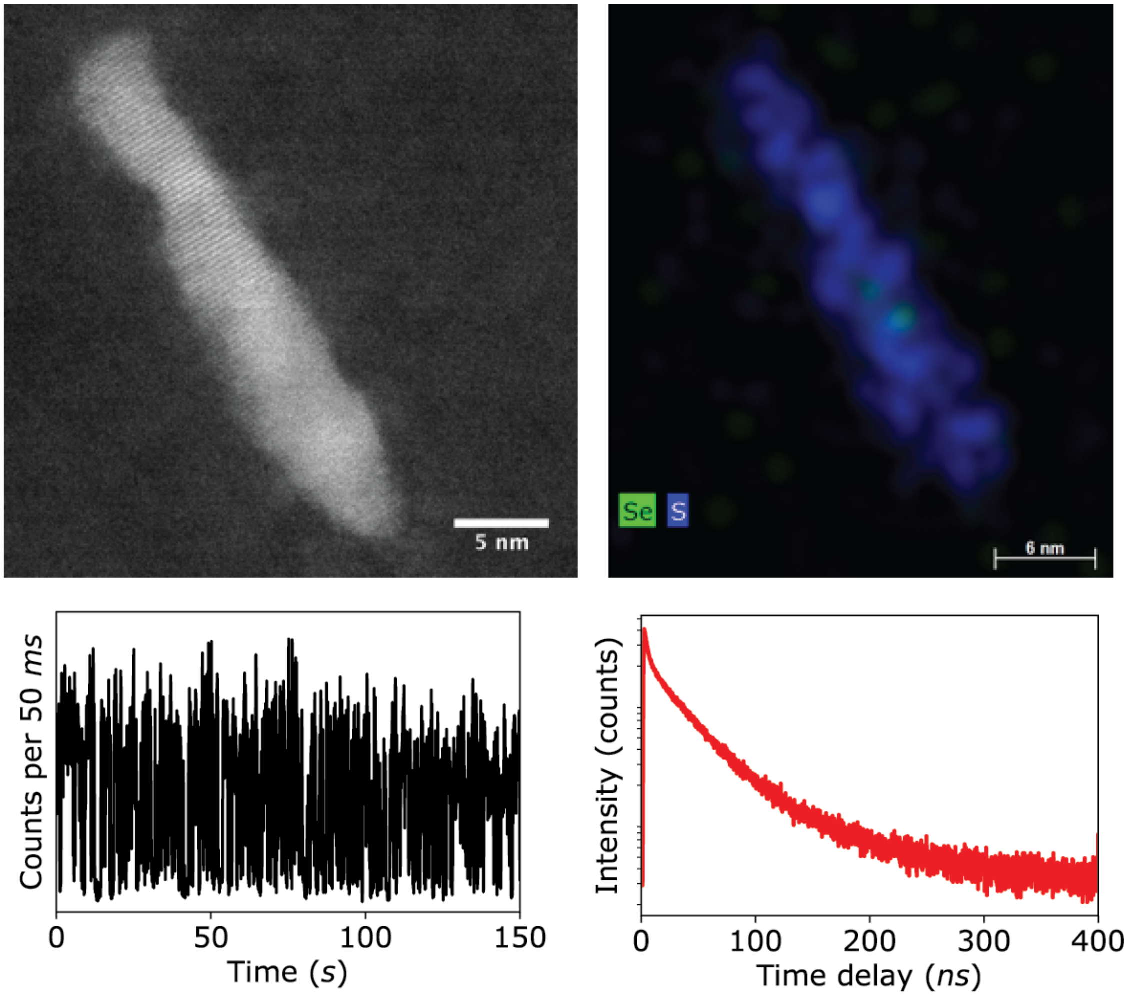
5 nm
Se
S
6 nm
Counts per 50 ms
0
50
100
150
Time (s)
Intensity (counts)
0
100
200
300
400
Time delay (ns)

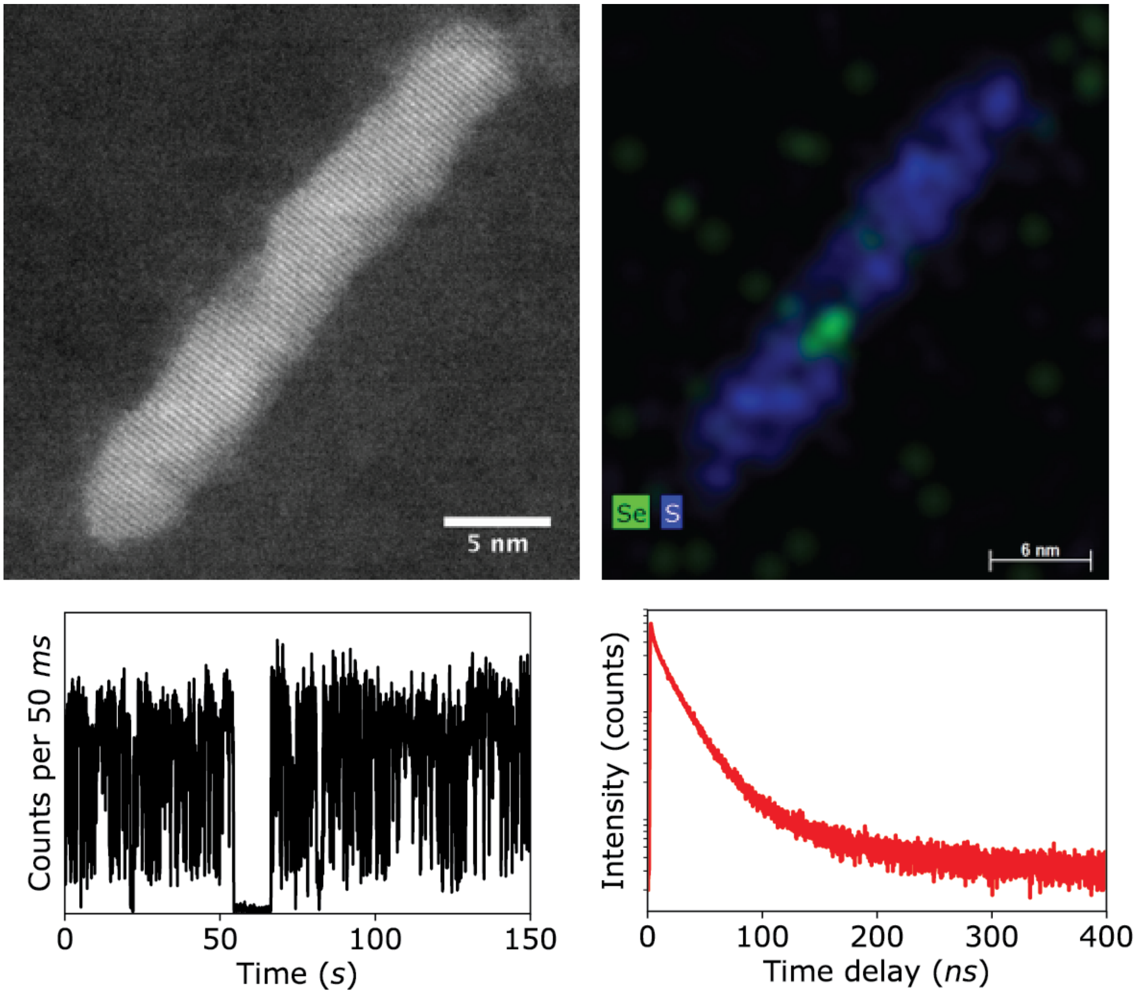
5 nm
Se
S
6 nm
Counts per 50 ms
0
50
100
150
Time (s)
Intensity (counts)
0
100
200
300
400
Time delay (ns)

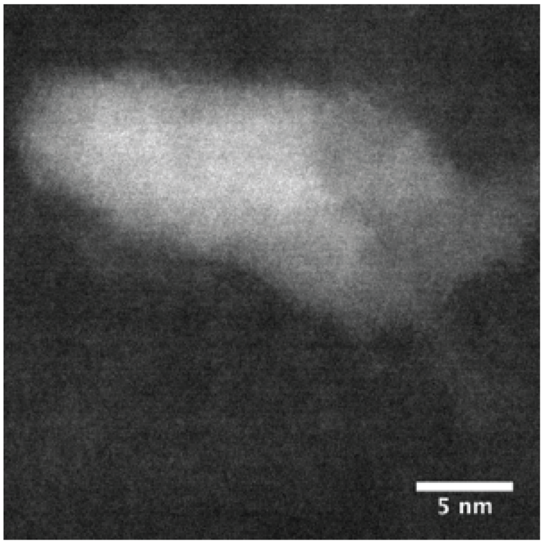
5 nm

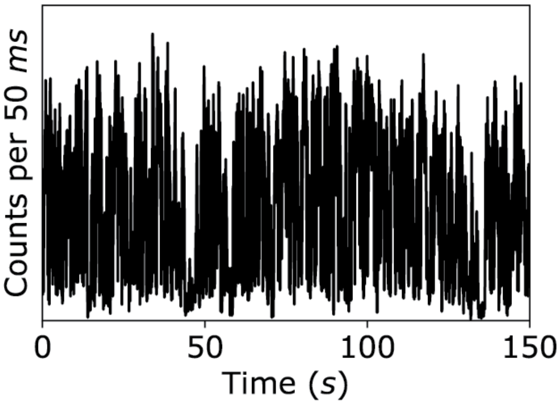
Counts per 50 ms
0
50
100
150
Time (s)

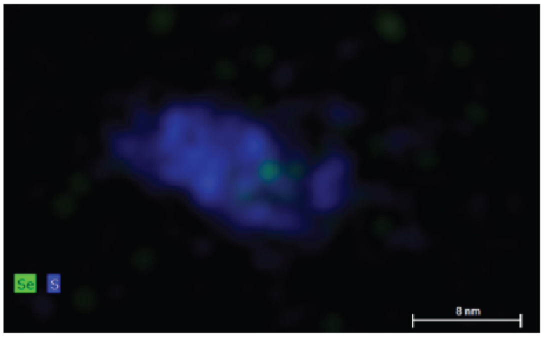
Se
S
8 nm

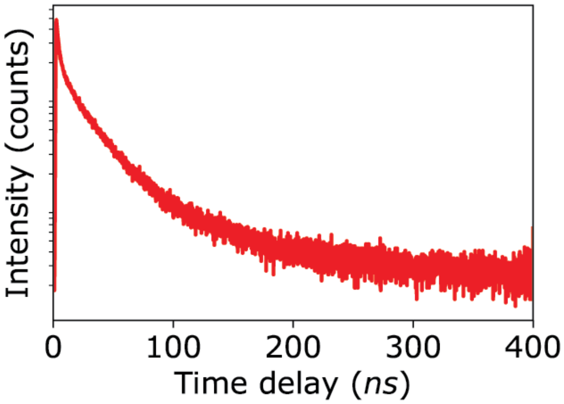
Intensity (counts)
0
100
200
300
400
Time delay (ns)

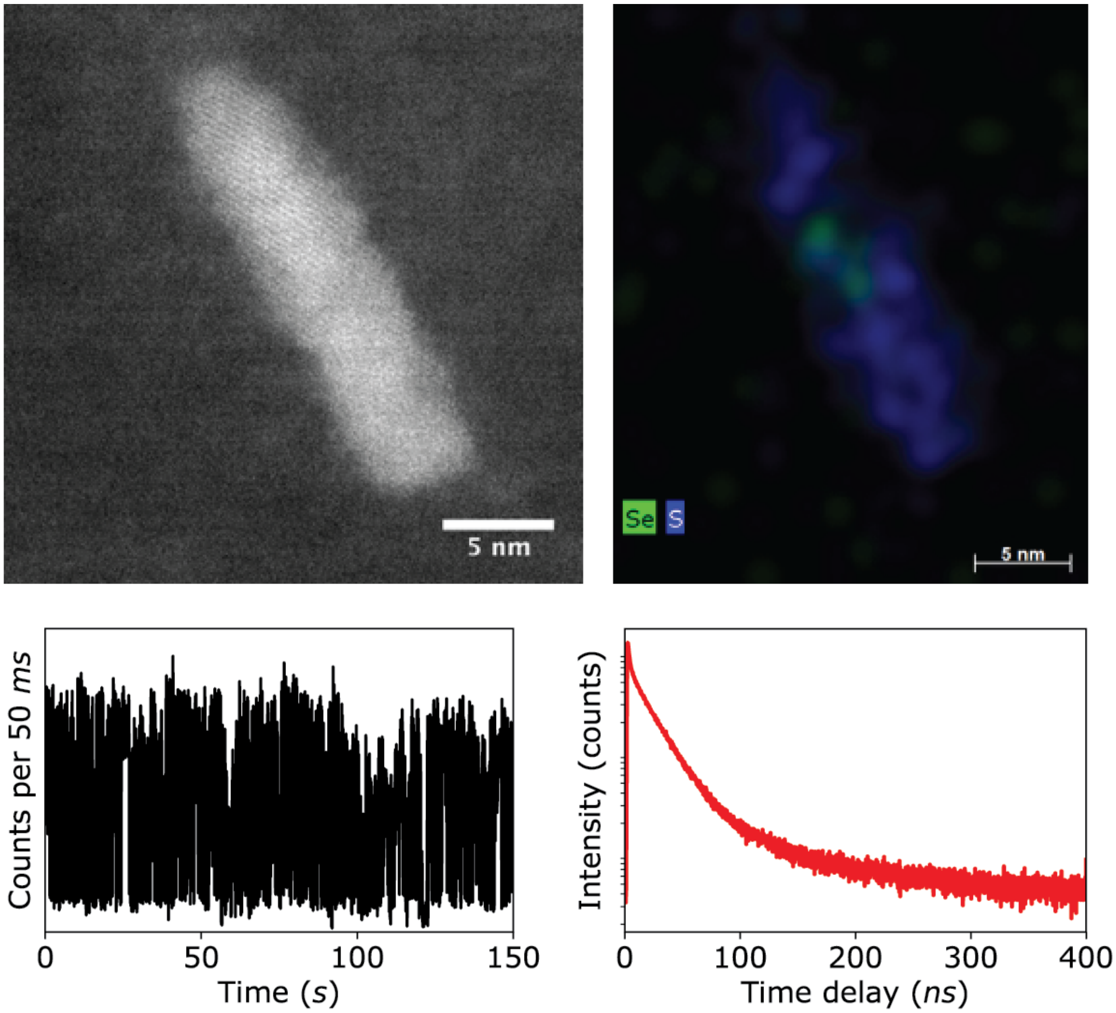
5 nm
Se
S
5 nm
Counts per 50 ms
0
50
100
150
Time (s)
Intensity (counts)
0
100
200
300
400
Time delay (ns)

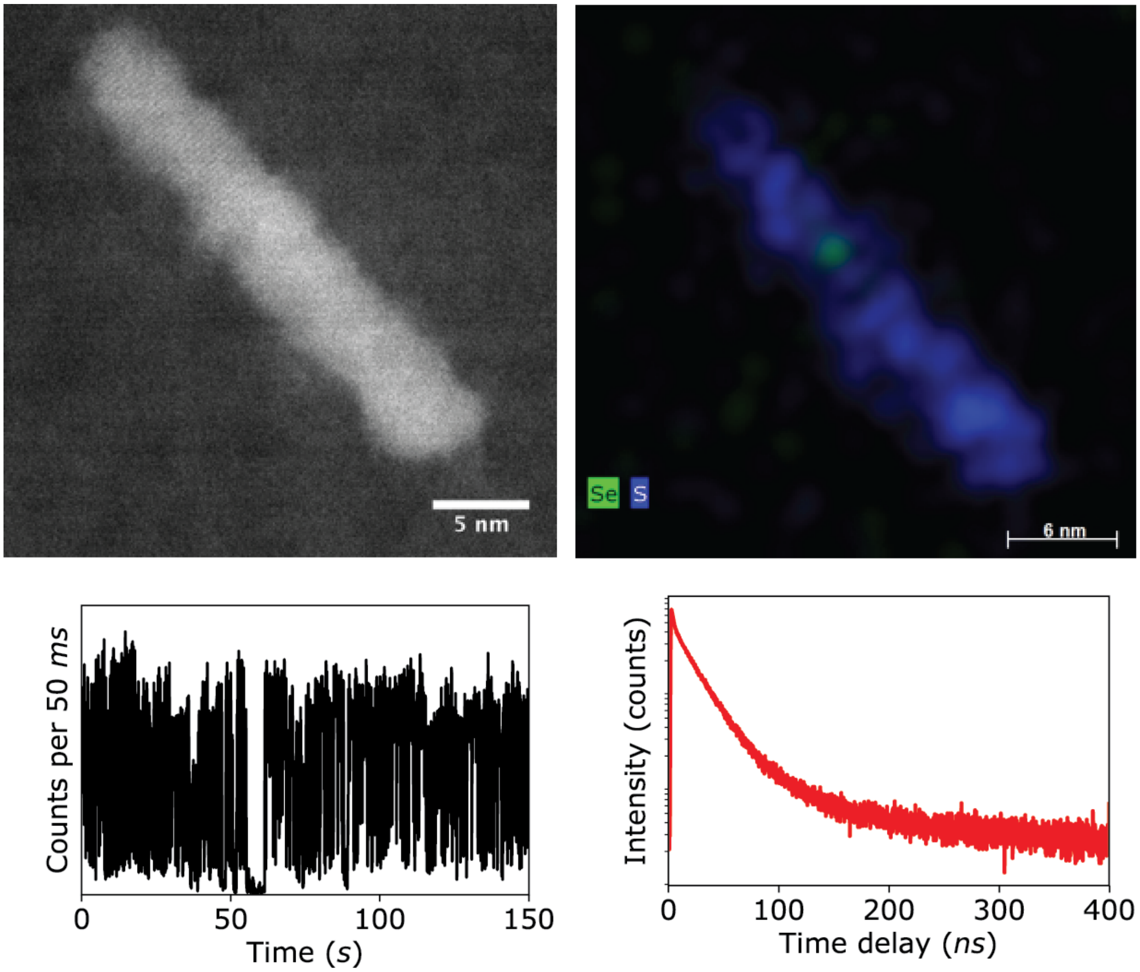
5 nm
Se
S
6 nm
Counts per 50 *ms*
0
50
100
150
Time (*s*)
Intensity (counts)
0
100
200
300
400
Time delay (*ns*)

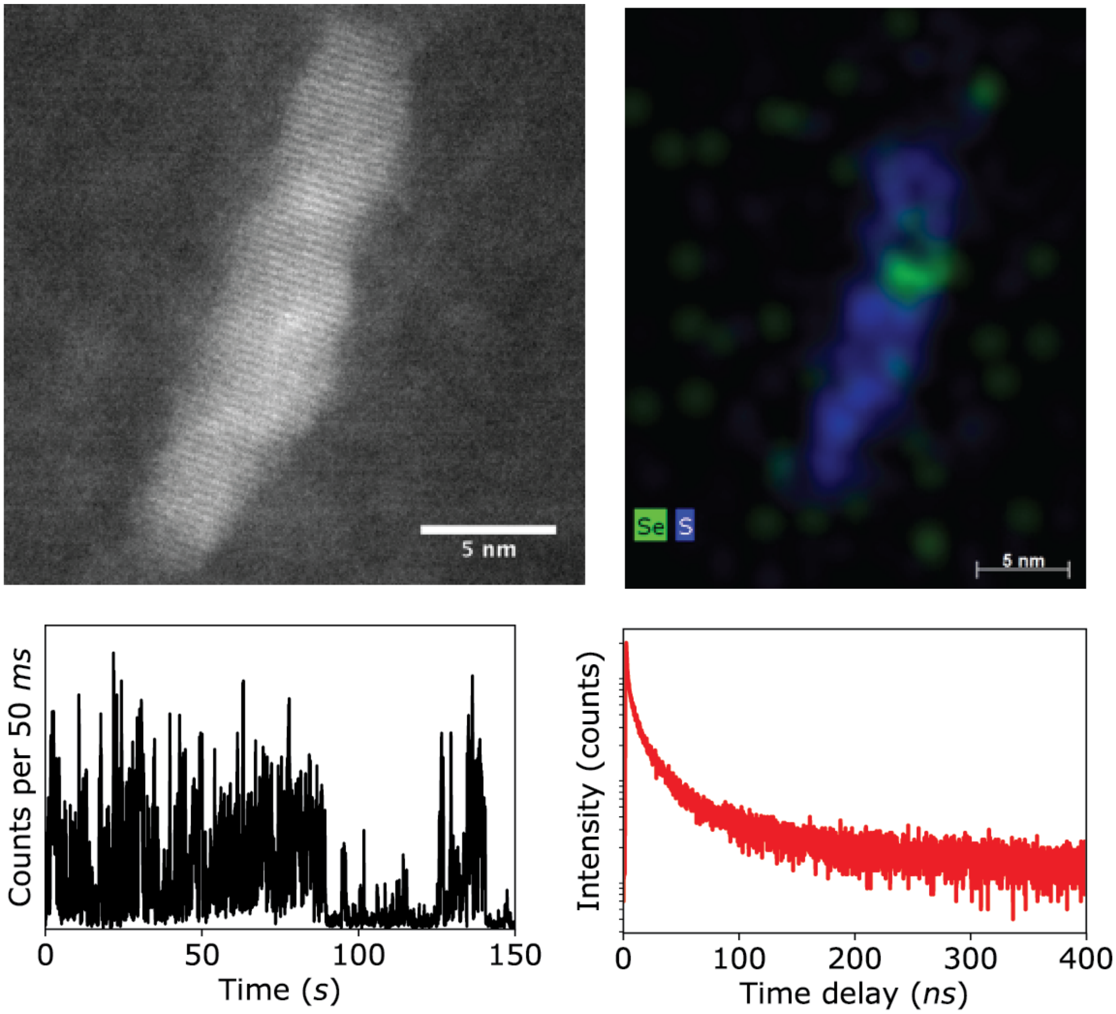
5 nm
Se
S
5 nm
Counts per 50 ms
0
50
100
150
Time (s)
Intensity (counts)
0
100
200
300
400
Time delay (ns)

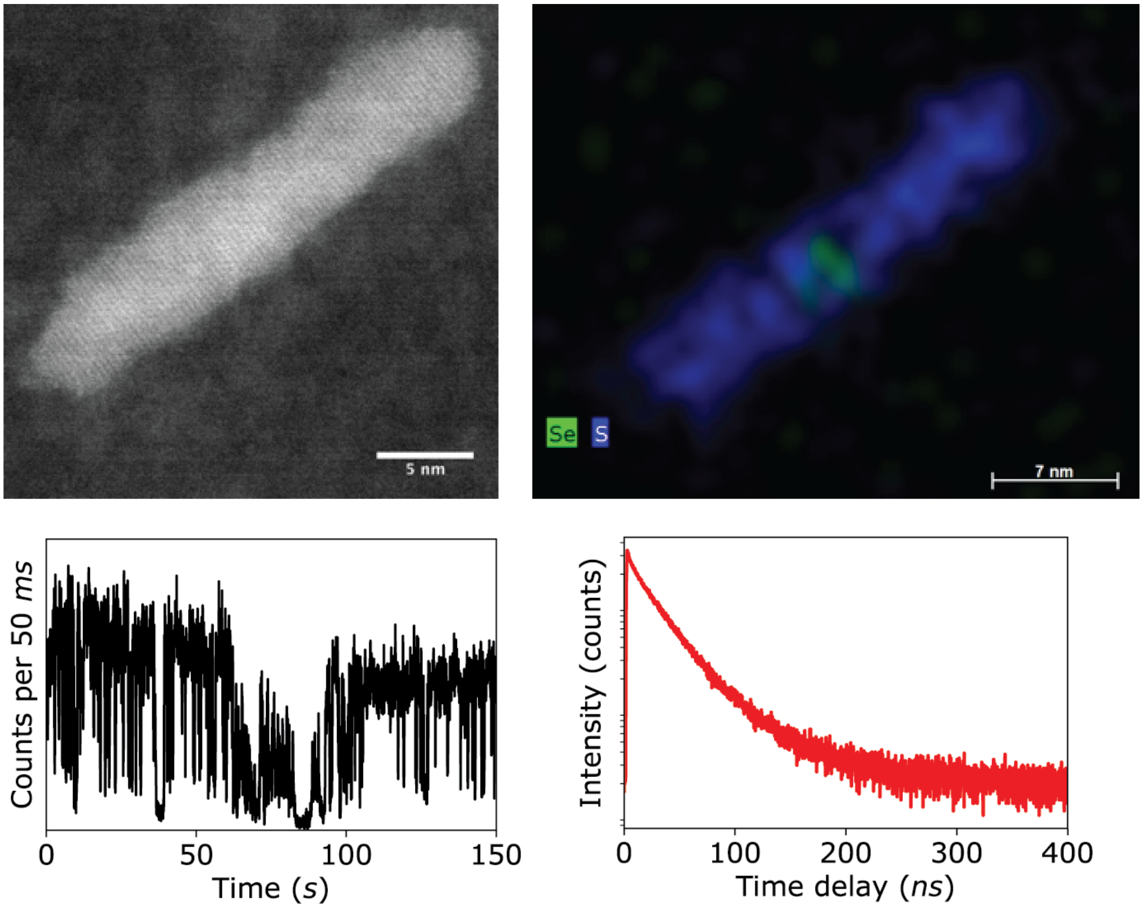
5 nm
Se
S
7 nm
Counts per 50 ms
0
50
100
150
Time (s)
Intensity (counts)
0
100
200
300
400
Time delay (ns)

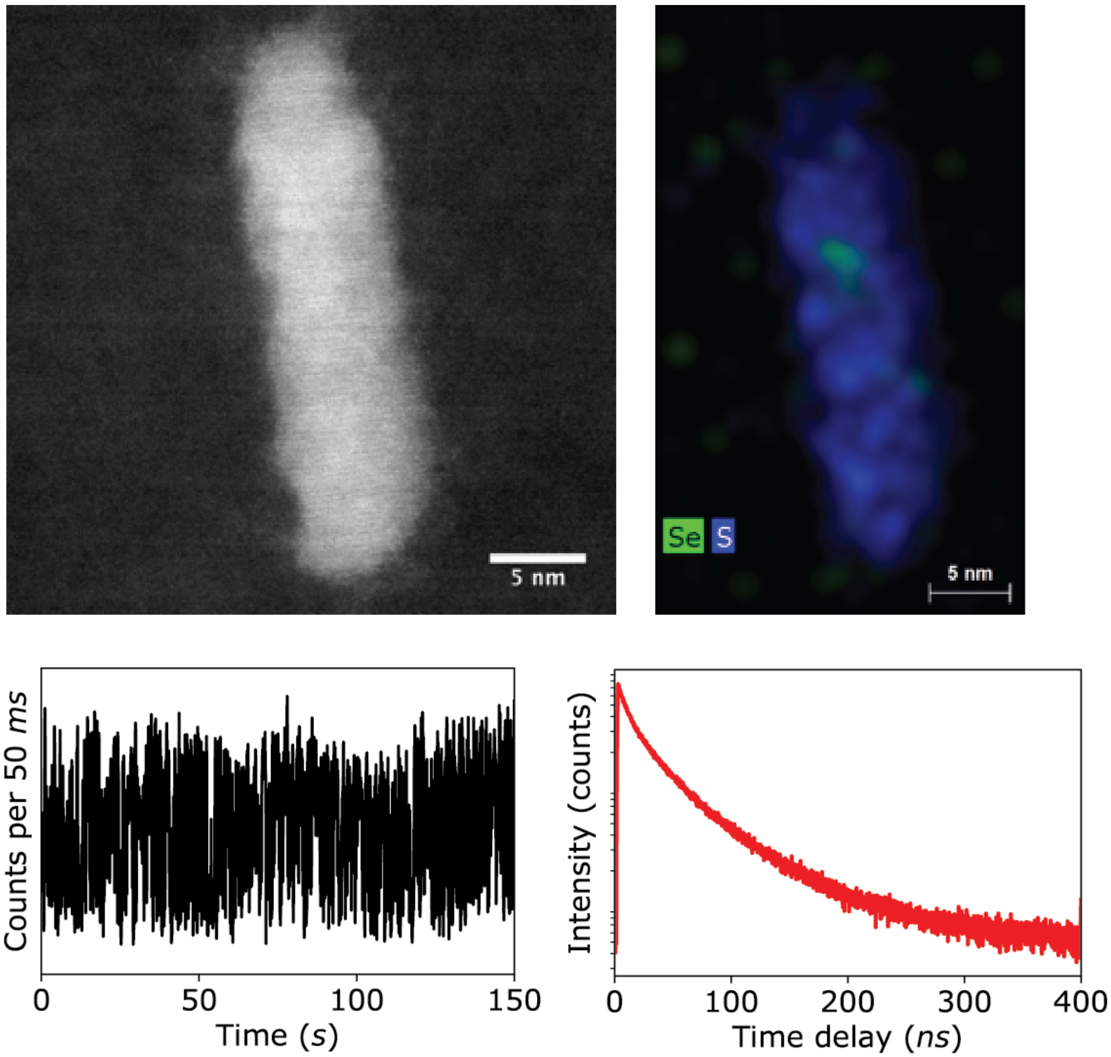
5 nm
Se
S
5 nm
Counts per 50 ms
0
50
100
150
Time (s)
Intensity (counts)
0
100
200
300
400
Time delay (ns)

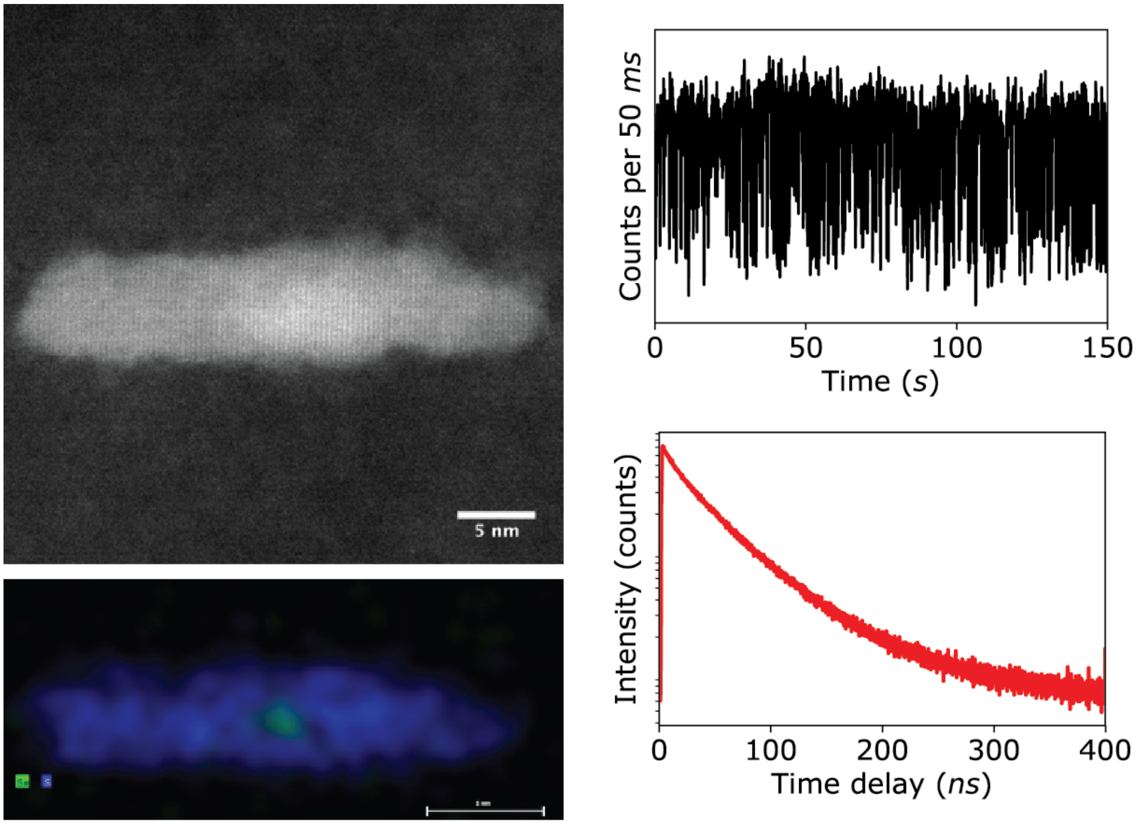
5 nm
S
Counts per 50 *ms*
Time (*s*)
0
50
100
150
Intensity (counts)
Time delay (*ns*)
0
100
200
300
400

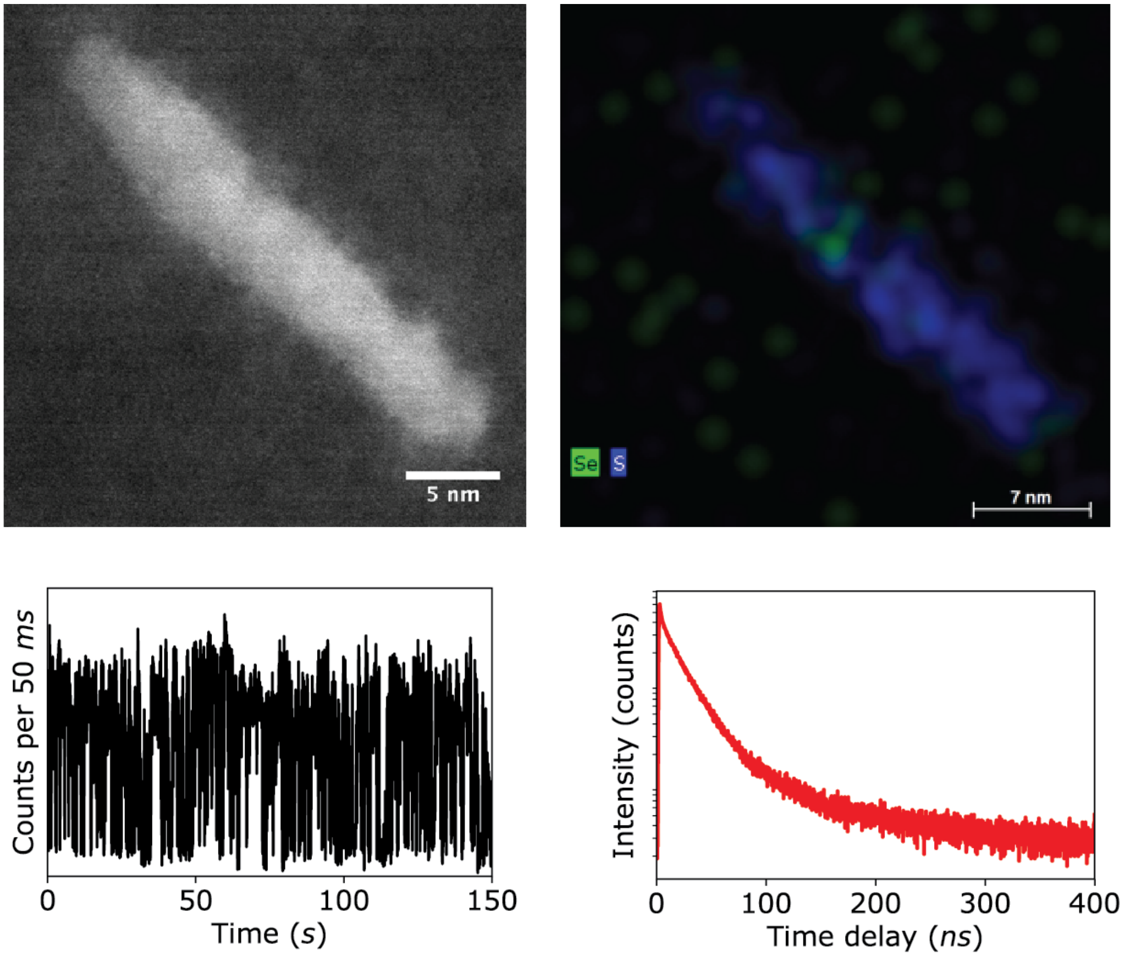
5 nm
Se
S
7 nm
Counts per 50 ms
0
50
100
150
Time (s)
Intensity (counts)
0
100
200
300
400
Time delay (ns)

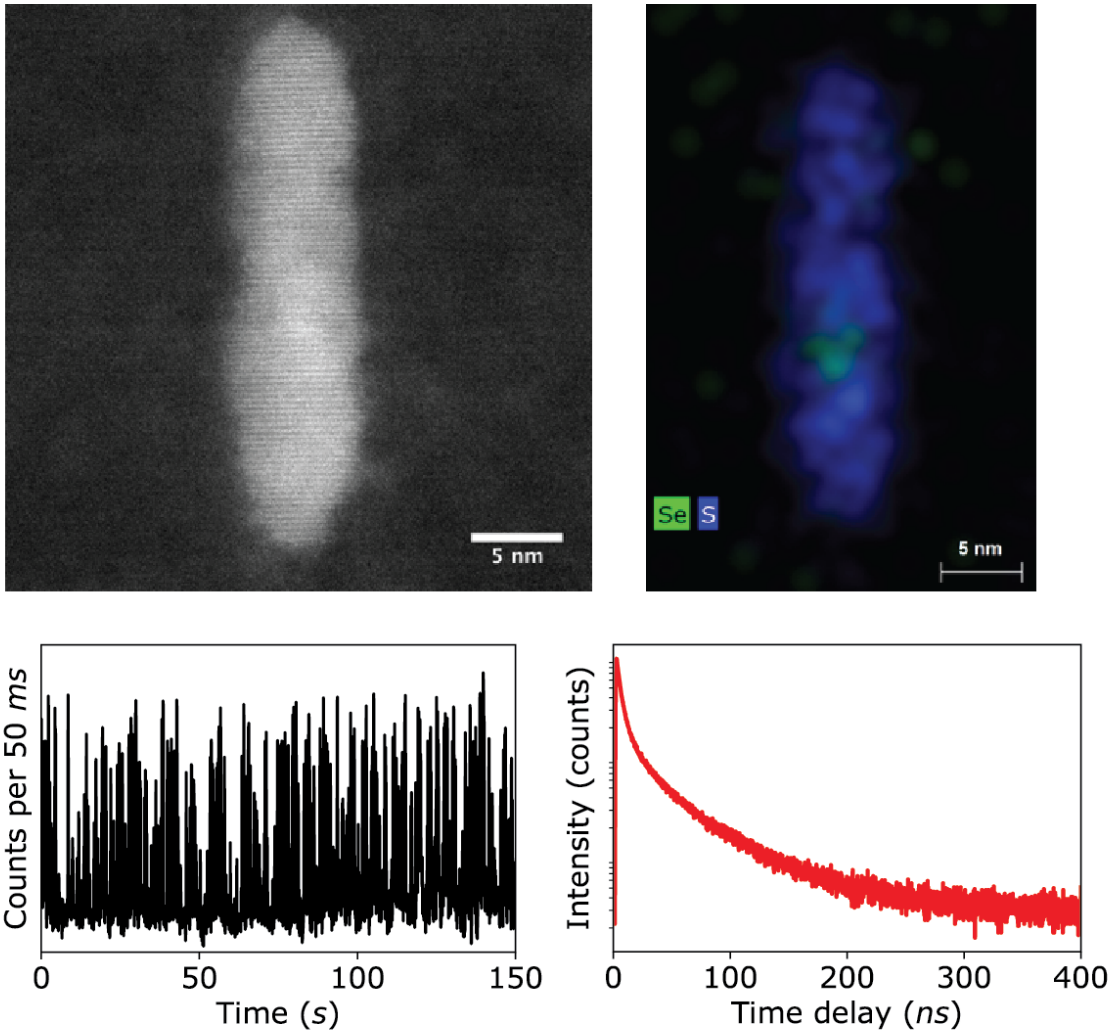
5 nm
Se
S
5 nm
Counts per 50 ms
0
50
100
150
Time (s)
Intensity (counts)
0
100
200
300
400
Time delay (ns)

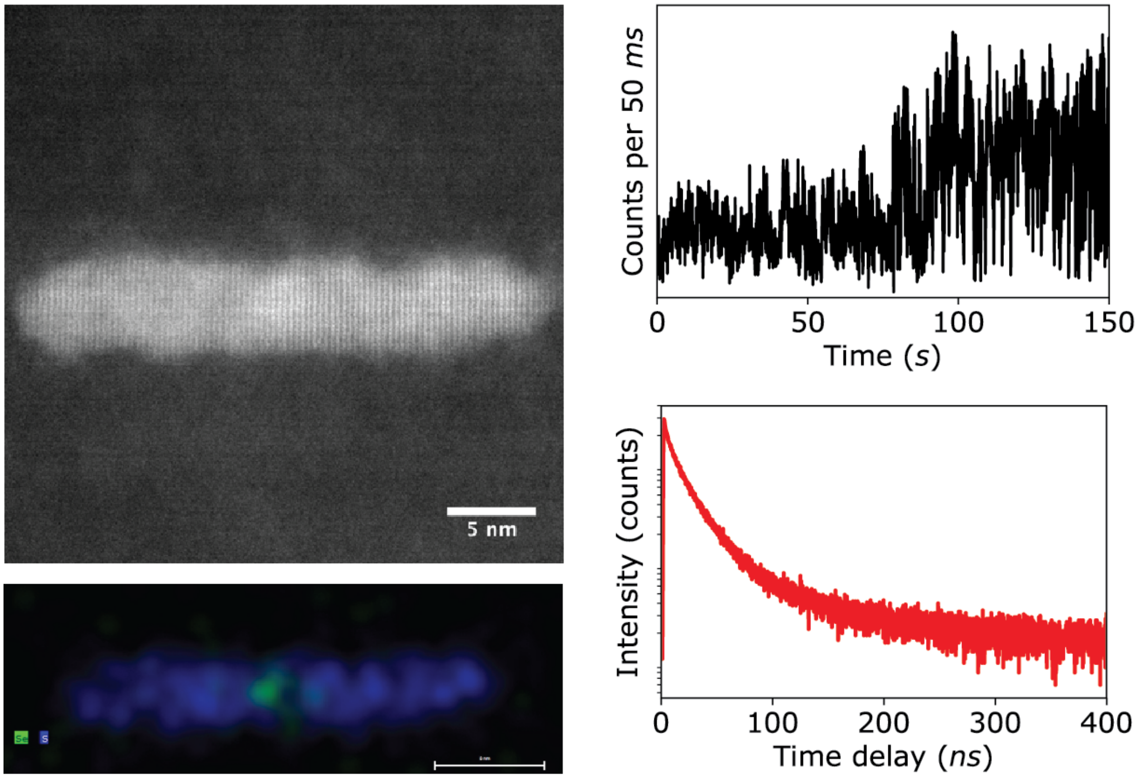
5 nm
Se
S
Counts per 50 *ms*
0
50
100
150
Time (*s*)
Intensity (counts)
0
100
200
300
400
Time delay (*ns*)

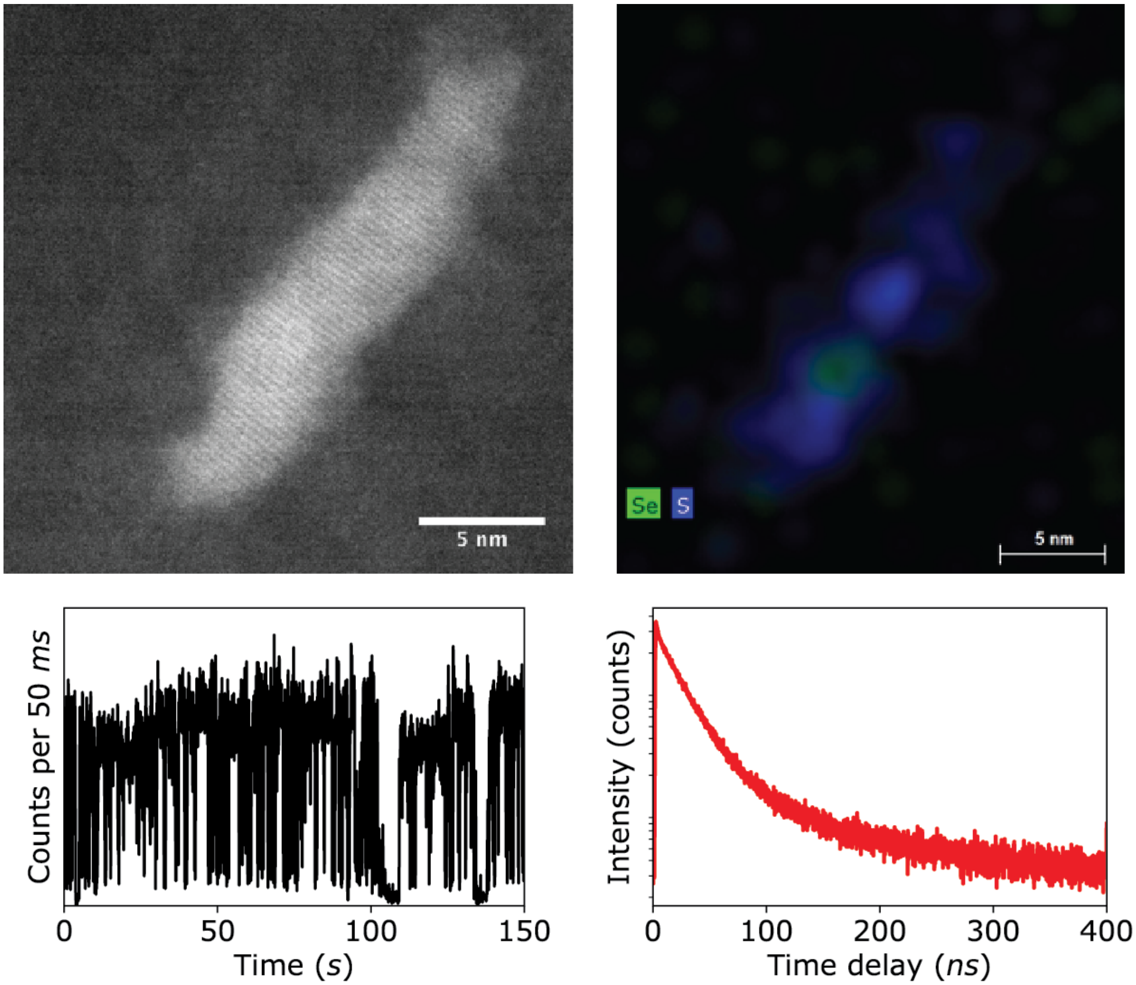
5 nm
Se
S
5 nm
Counts per 50 ms
0
50
100
150
Time (s)
Intensity (counts)
0
100
200
300
400
Time delay (ns)

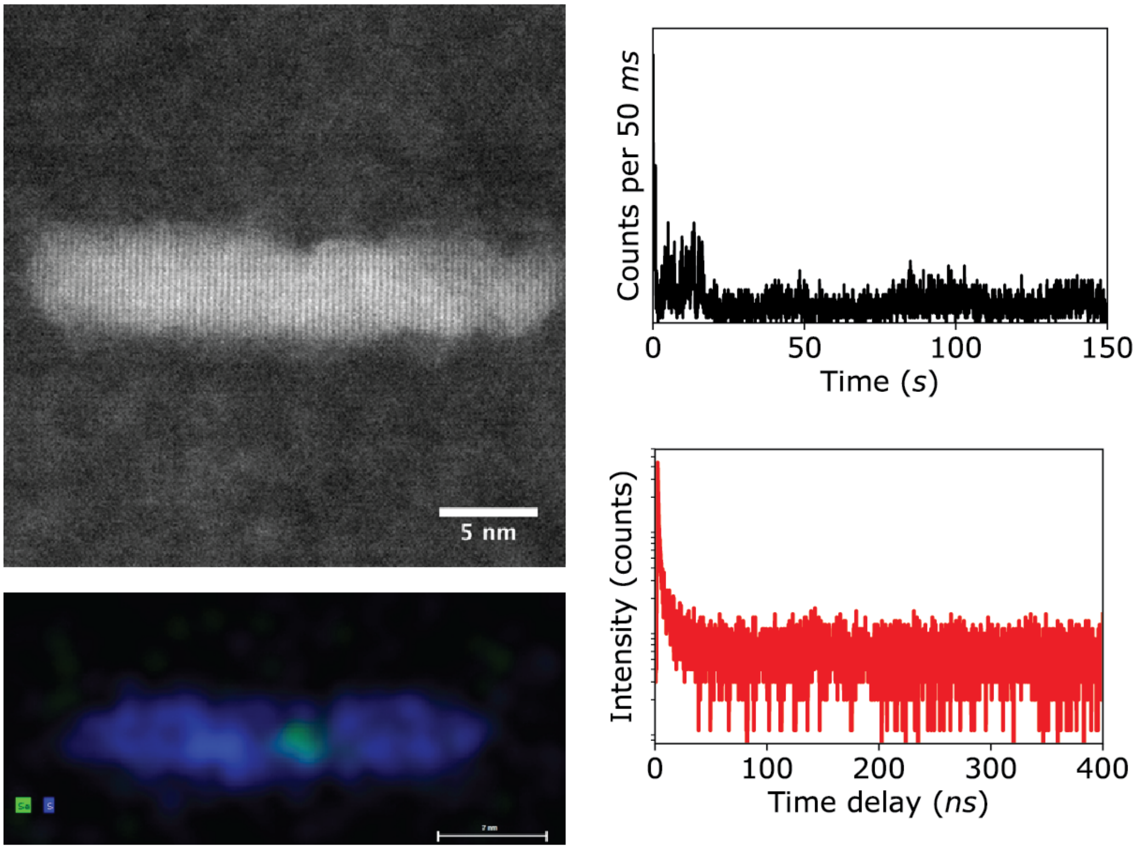
5 nm
Se
S
7 nm
Counts per 50 ms
0
50
100
150
Time (s)
Intensity (counts)
0
100
200
300
400
Time delay (ns)

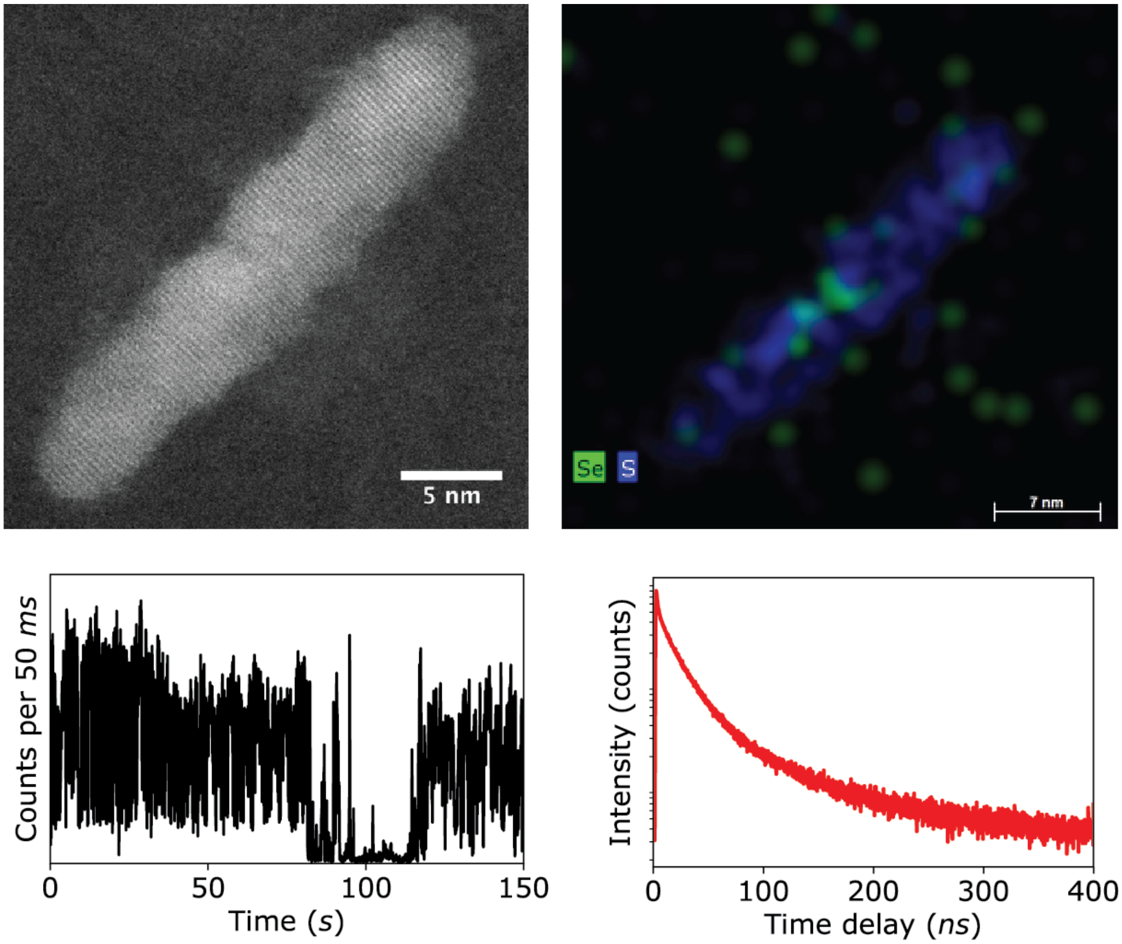
5 nm
Se
S
7 nm
Counts per 50 *ms*
Time (*s*)
0
50
100
150
Intensity (counts)
Time delay (*ns*)
0
100
200
300
400

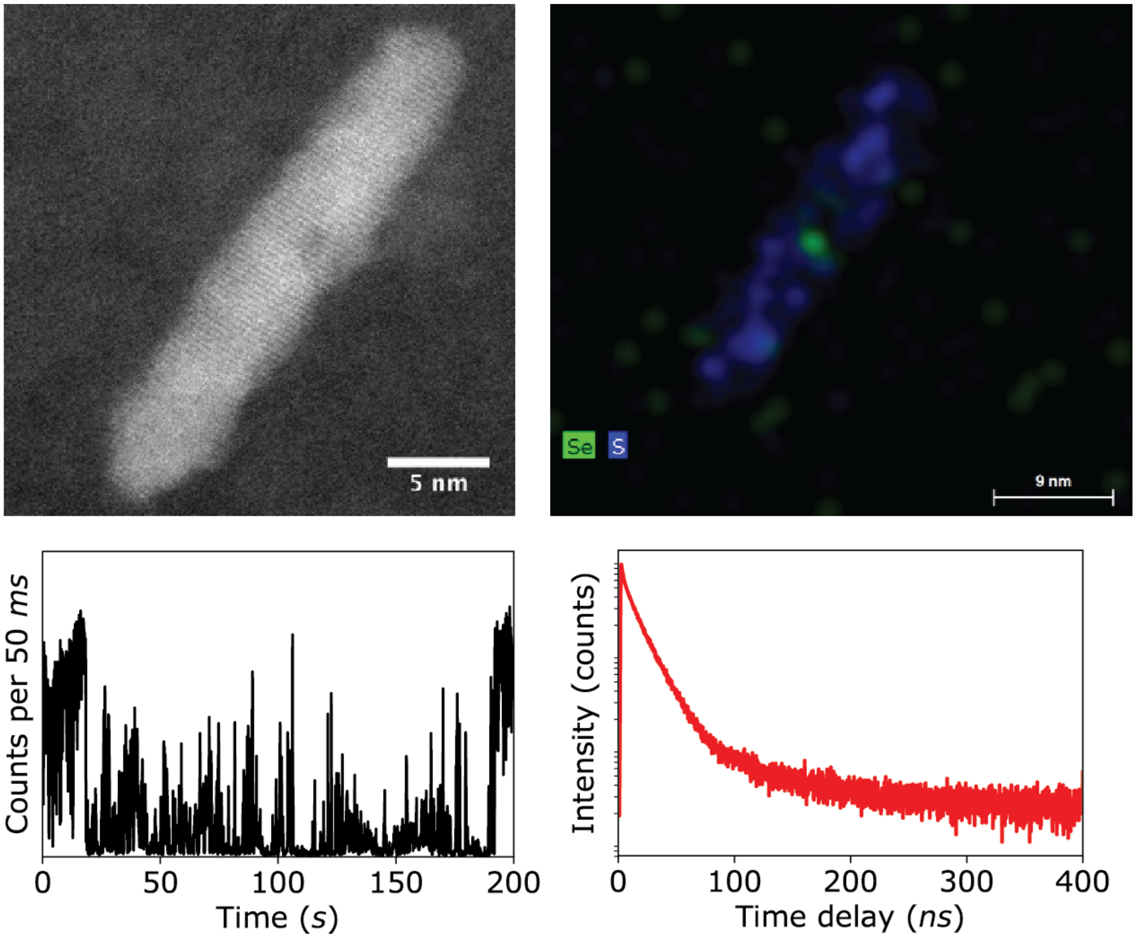
5 nm
Se
S
9 nm
Counts per 50 *ms*
0
50
100
150
200
Time (*s*)
Intensity (counts)
0
100
200
300
400
Time delay (*ns*)

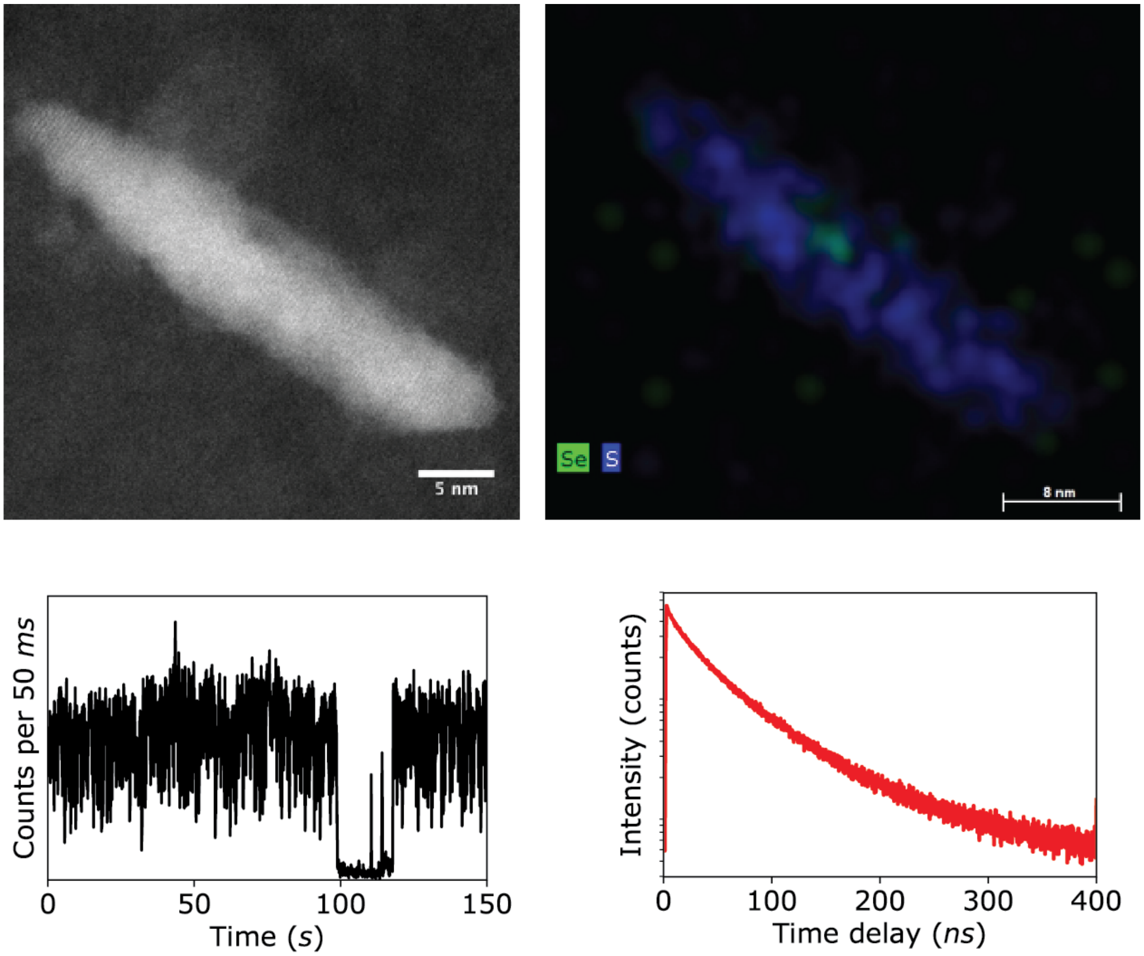
5 nm
Se
S
8 nm
Counts per 50 ms
0
50
100
150
Time (s)
Intensity (counts)
0
100
200
300
400
Time delay (ns)

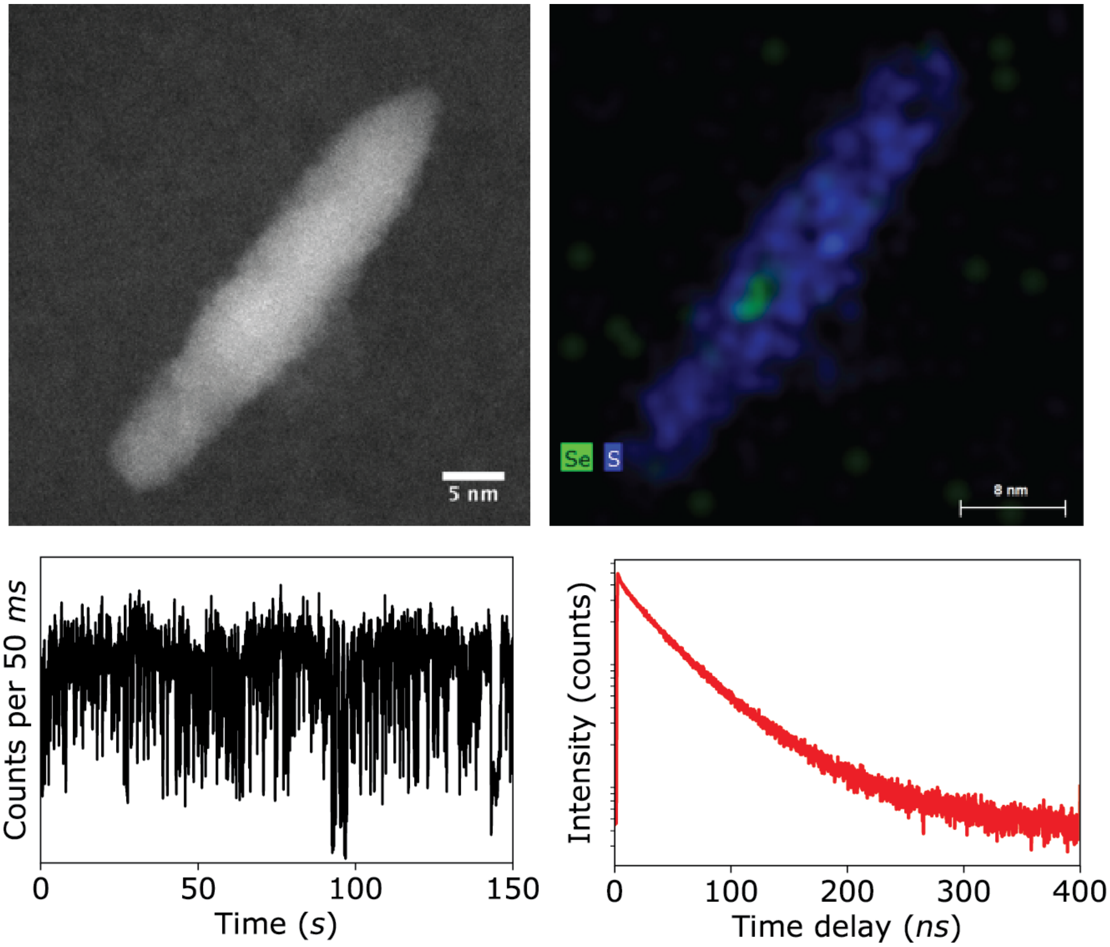
5 nm
Se
S
8 nm
Counts per 50 ms
0
50
100
150
Time (s)
Intensity (counts)
0
100
200
300
400
Time delay (ns)

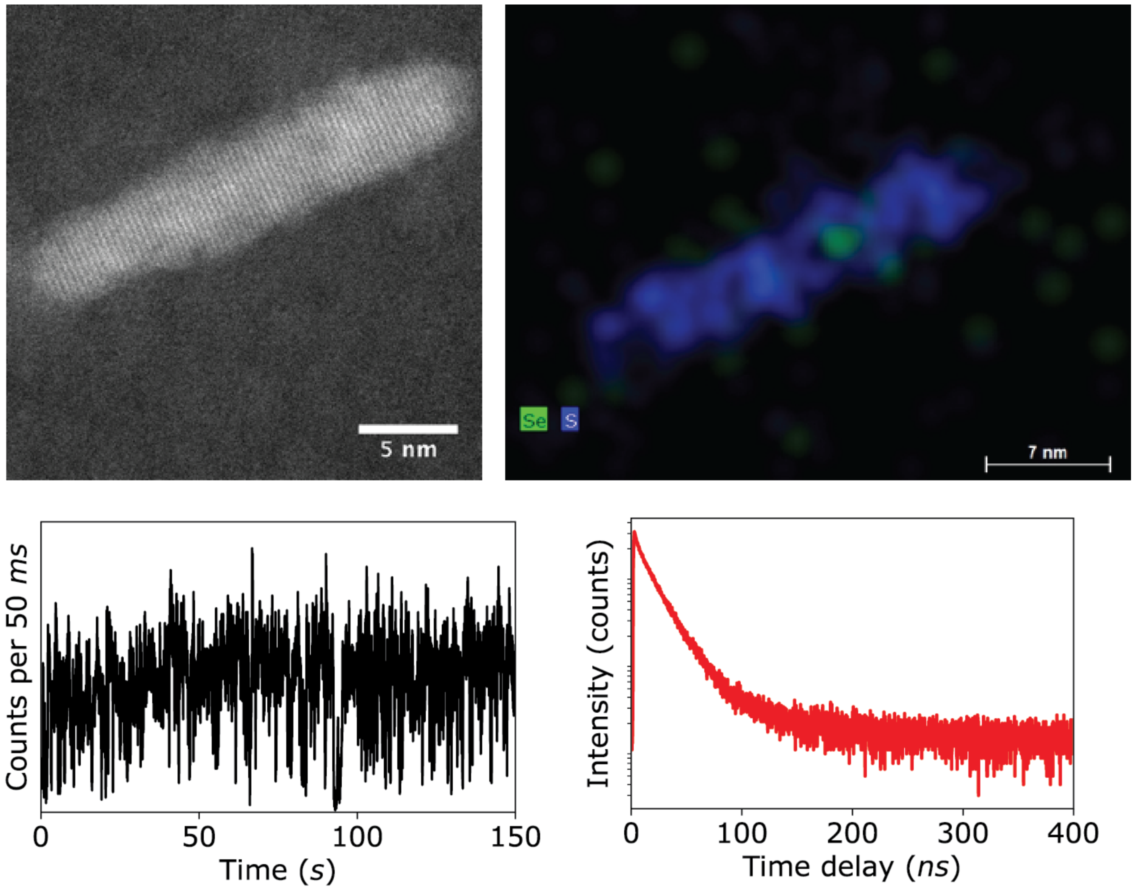
5 nm
Se
S
7 nm
Counts per 50 *ms*
Time (*s*)
0
50
100
150
Intensity (counts)
Time delay (*ns*)
0
100
200
300
400

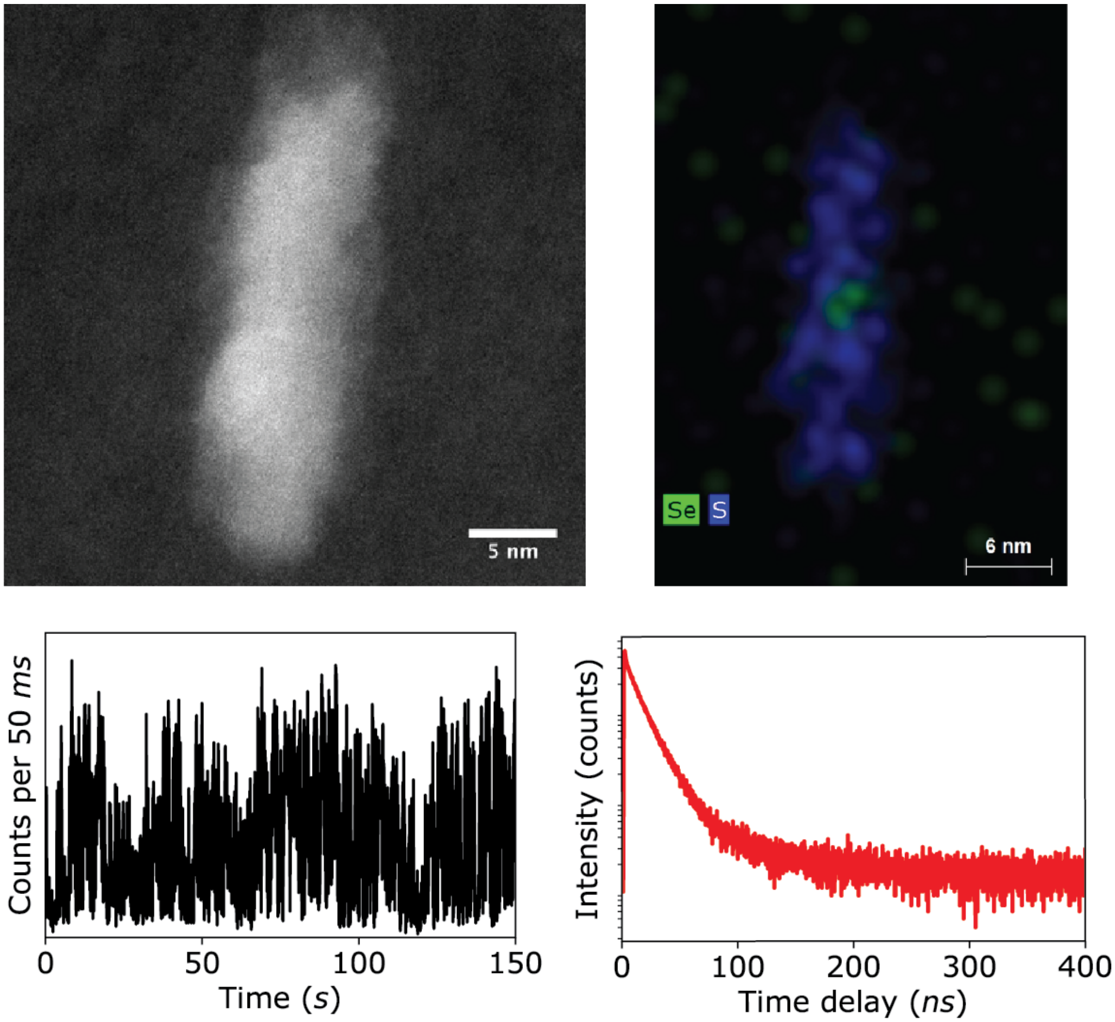
5 nm
Se
S
6 nm
Counts per 50 *ms*
0
50
100
150
Time (*s*)
Intensity (counts)
0
100
200
300
400
Time delay (*ns*)

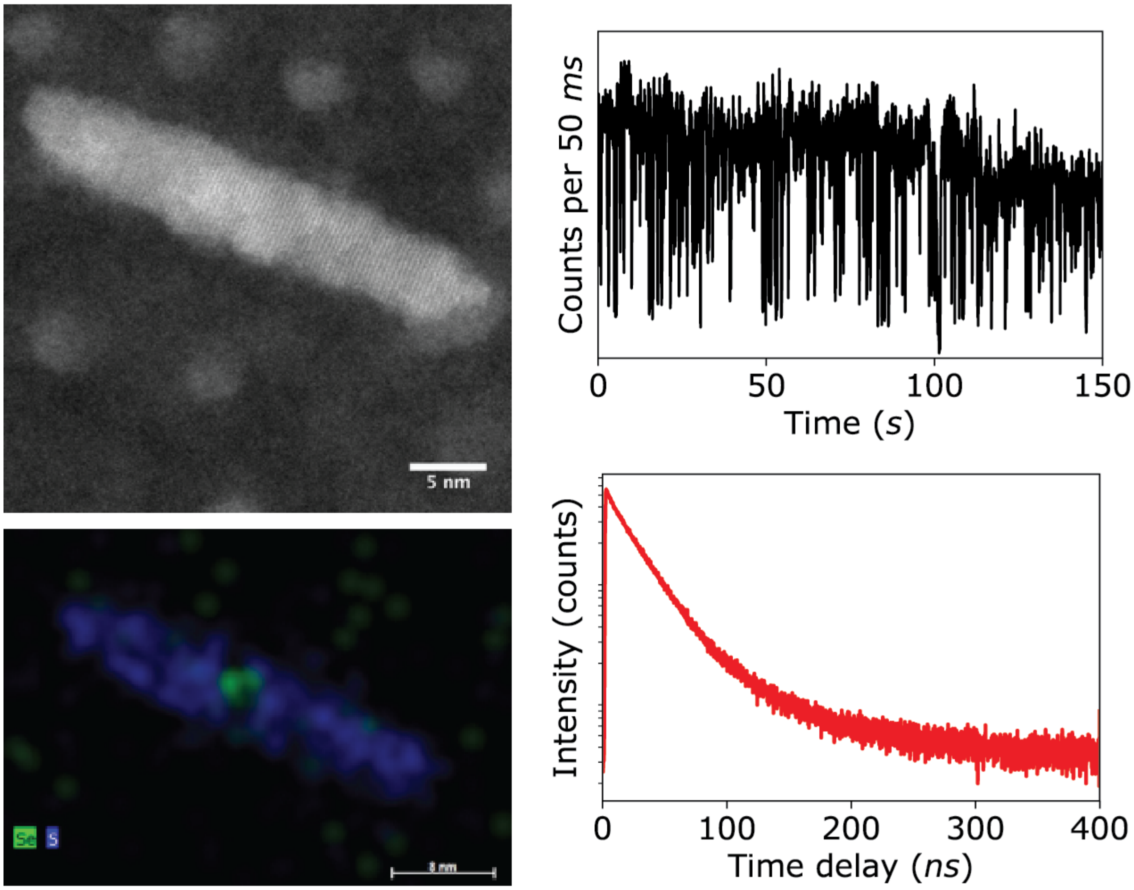
5 nm
Se
S
8 nm
Counts per 50 ms
0
50
100
150
Time (s)
Intensity (counts)
0
100
200
300
400
Time delay (ns)

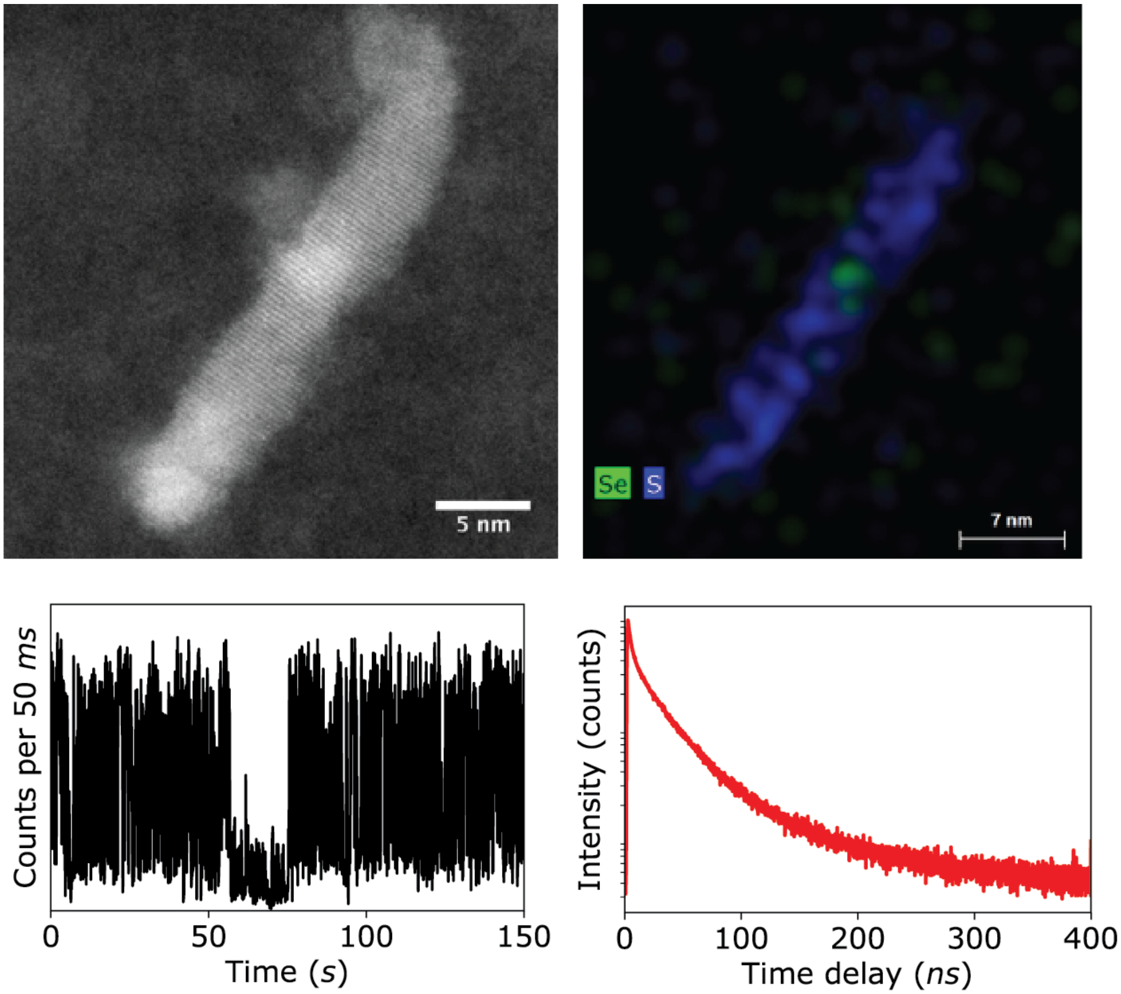
5 nm
Se
S
7 nm
Counts per 50 ms
Time (s)
0
50
100
150
Intensity (counts)
Time delay (ns)
0
100
200
300
400

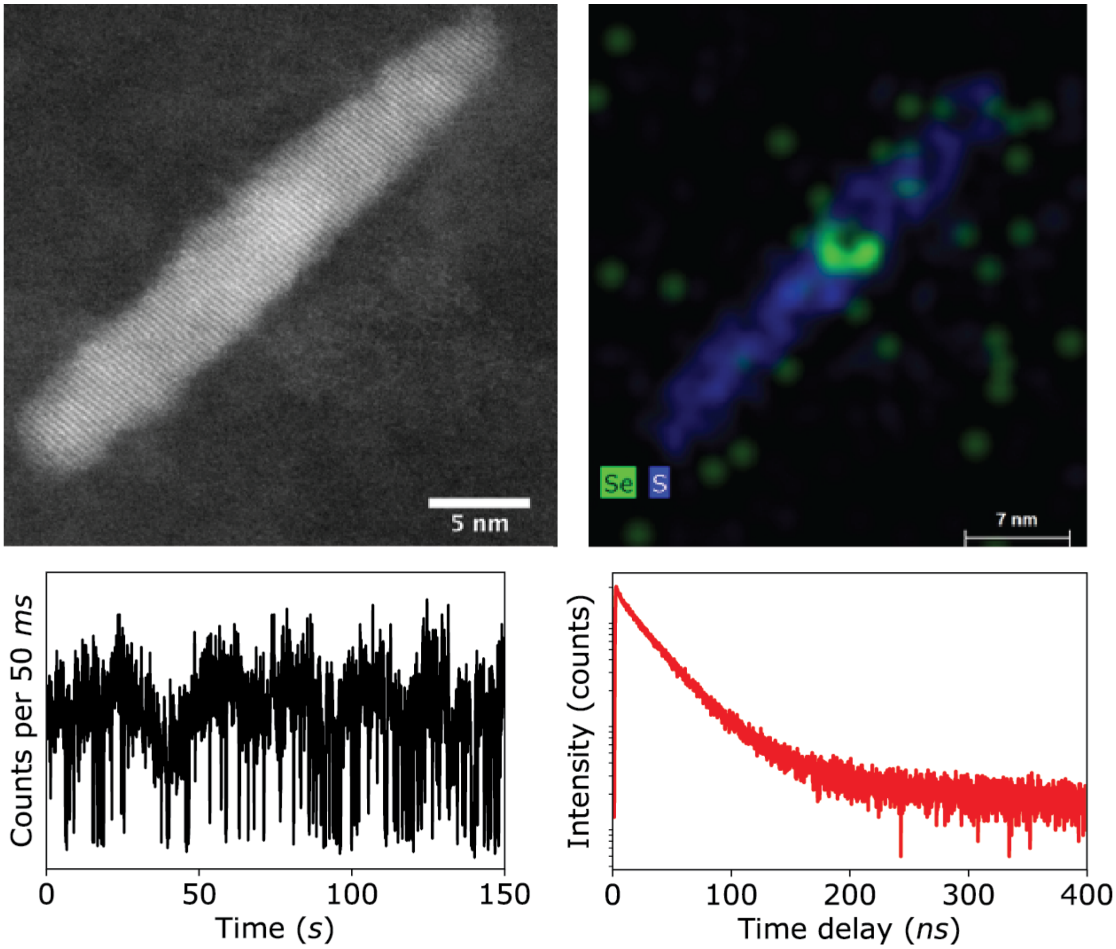
5 nm
Se
S
7 nm
Counts per 50 *ms*
0
50
100
150
Time (*s*)
Intensity (counts)
0
100
200
300
400
Time delay (*ns*)

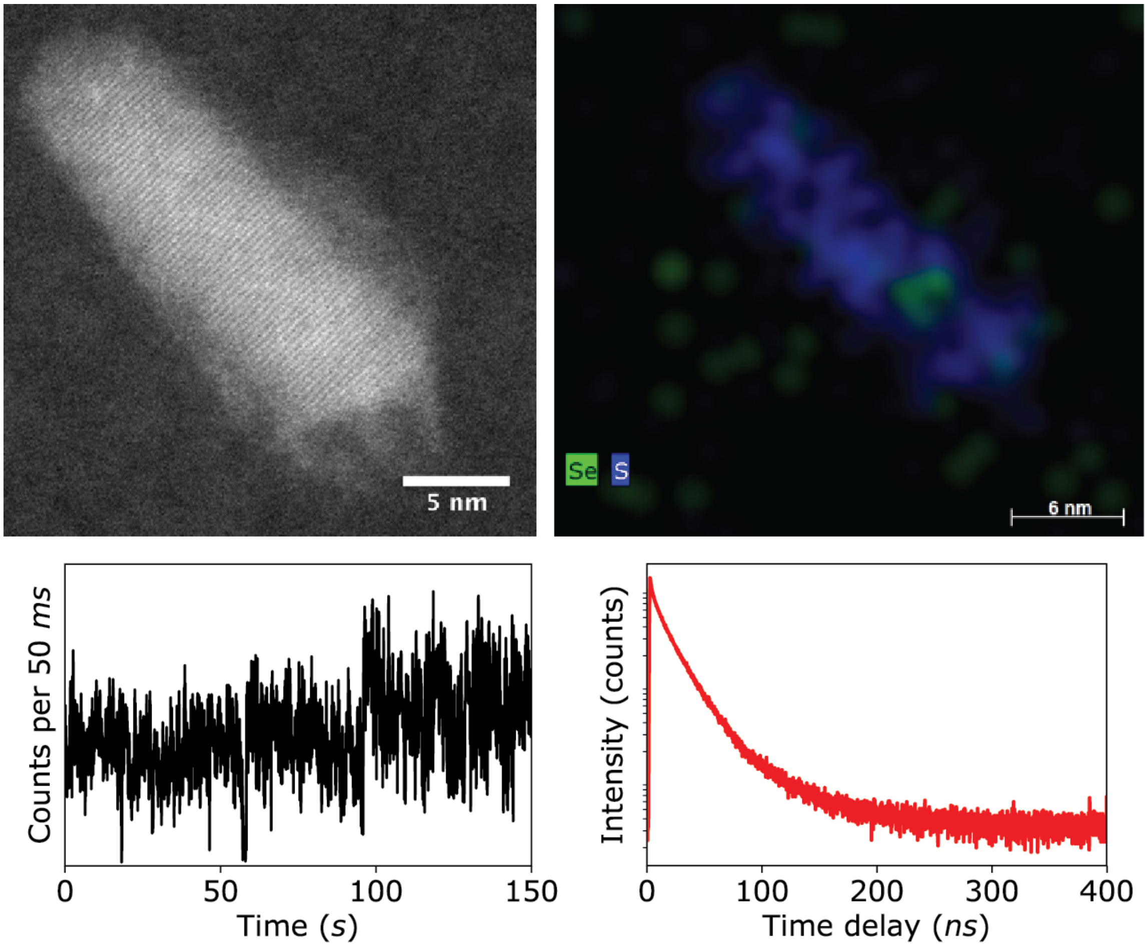
5 nm
Se
S
6 nm
Counts per 50 ms
0
50
100
150
Time (s)
Intensity (counts)
0
100
200
300
400
Time delay (ns)

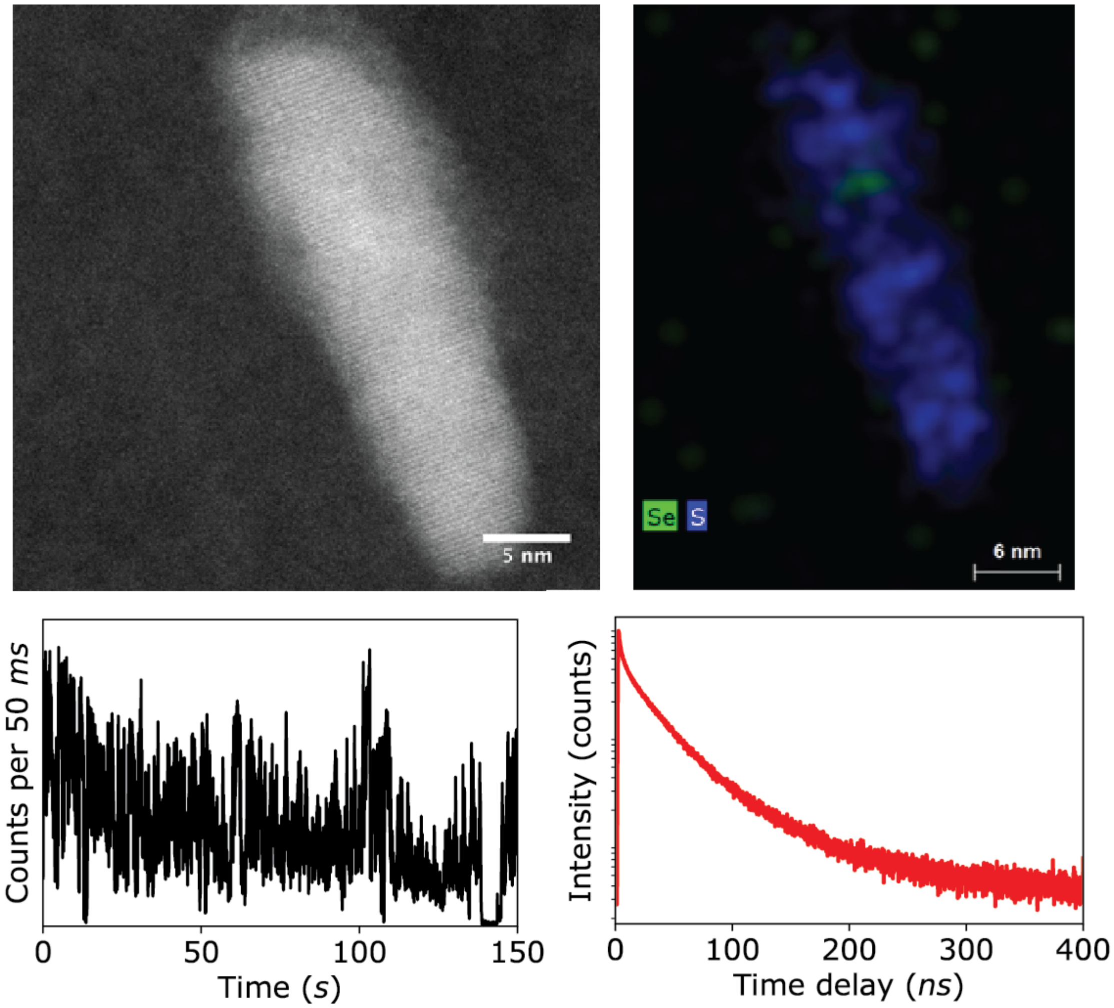
5 nm
Se
S
6 nm
Counts per 50 ms
0
50
100
150
Time (s)
Intensity (counts)
0
100
200
300
400
Time delay (ns)

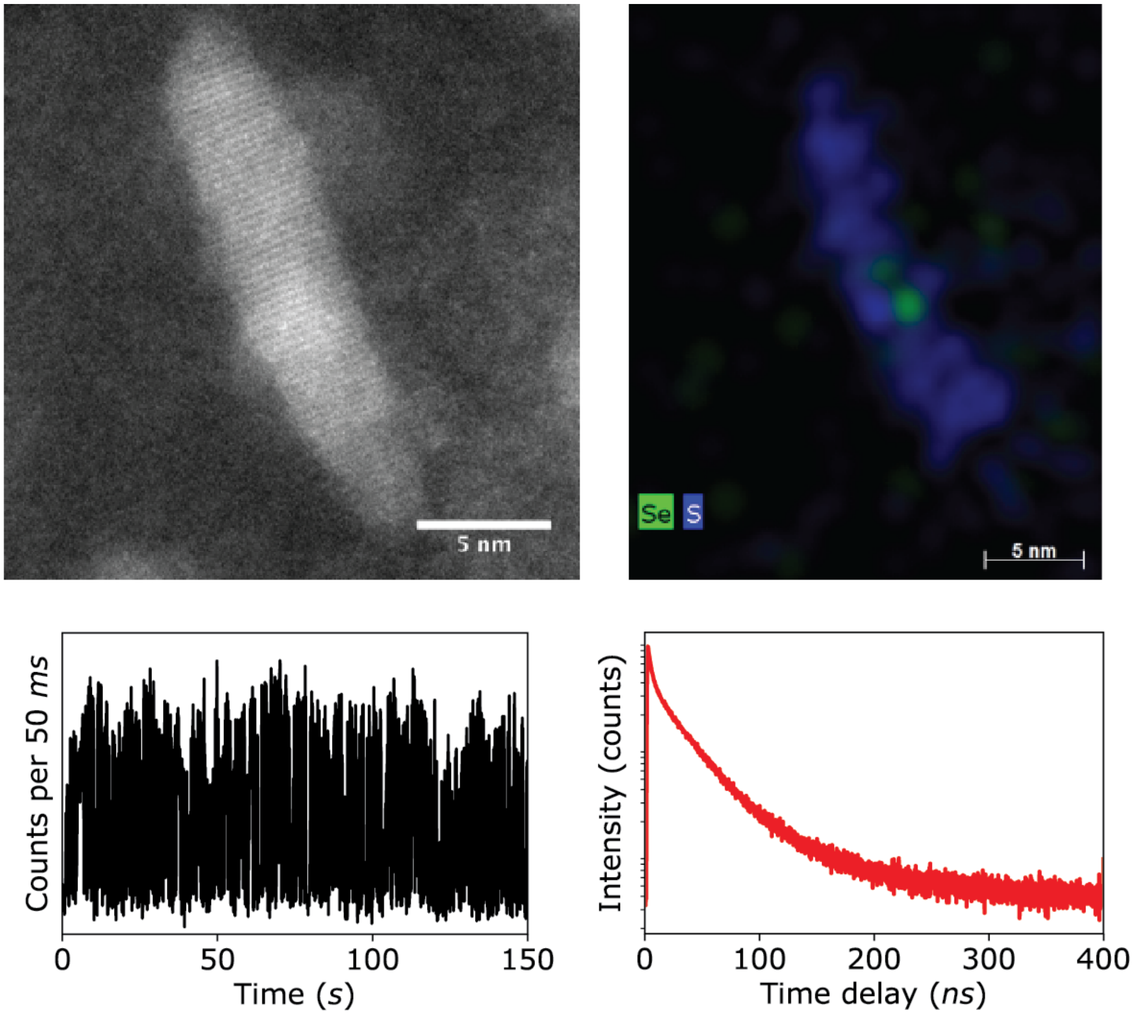
5 nm
Se
S
5 nm
Counts per 50 ms
0
50
100
150
Time (s)
Intensity (counts)
0
100
200
300
400
Time delay (ns)

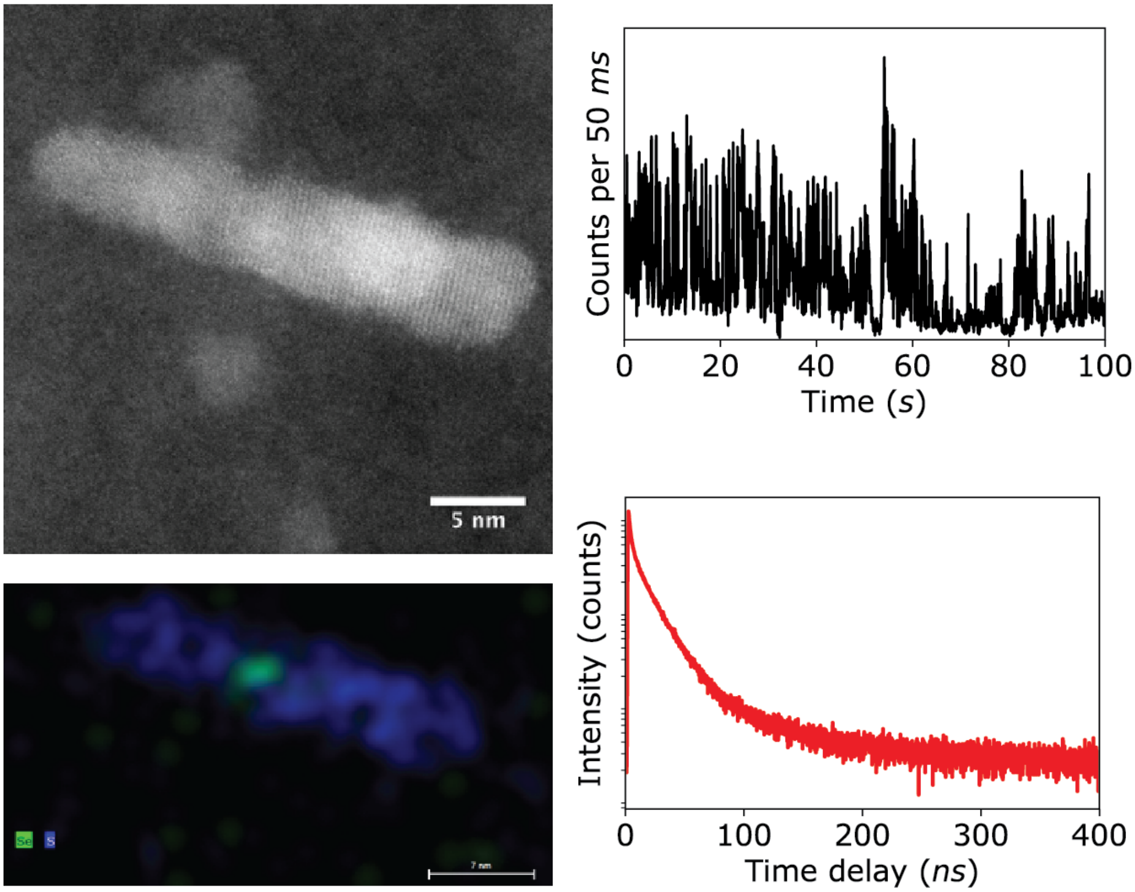
5 nm
Se
S
7 nm
Counts per 50 ms
0
20
40
60
80
100
Time (s)
Intensity (counts)
0
100
200
300
400
Time delay (ns)

References

(1) Brus, L. E. *J. Chem. Phys.* **1984**, *80*, 4403–4409, DOI: 10.1063/1.447218.

(2) Ekimov, A. I.; Onushchenko, A. A. *JETP Lett.* **1981**, *34*, 345.

(3) Ekimov, A. I.; Efros, A. L.; Onushchenko, A. A. *Solid State Communications* **1985**, *56*, 921–924, DOI: 10.1016/S0038-1098(85)80025-9.

(4) Caruge, J. M.; Halpert, J. E.; Wood, V.; Bulović, V.; Bawendi, M. G. *Nature Photonics* **2008**, *2*, 247–250, DOI: 10.1038/nphoton.2008.34.

(5) Meinardi, F.; McDaniel, H.; Carulli, F.; Colombo, A.; Velizhanin, K. A.; Makarov, N. S.; Simonutti, R.; Klimov, V. I.; Brovelli, S. *Nat Nano* **2015**, *10*, 878–885, DOI: 10.1038/nnano.2015.178.

(6) Fan, F. et al. *Nature* **2017**, *544*, 75–79, DOI: 10.1038/nature21424.

(7) Kim, T.-H.; Cho, K.-S.; Lee, E. K.; Lee, S. J.; Chae, J.; Kim, J. W.; Kim, D. H.; Kwon, J.-Y.; Amaratunga, G.; Lee, S. Y.; Choi, B. L.; Kuk, Y.; Kim, J. M.; Kim, K. *Nat Photon* **2011**, *5*, 176–182, DOI: 10.1038/nphoton.2011.12.

(8) Rosenthal, S. J.; Chang, J. C.; Kovtun, O.; McBride, J. R.; Tomlinson, I. D. *Chemistry & Biology* **2011**, *18*, 10–24, DOI: 10.1016/j.chembiol.2010.11.013.

(9) Efros, A. L.; Rosen, M. *Annual Review of Materials Science* **2000**, *30*, 475–521, DOI: 10.1146/annurev.matsci.30.1.475.

(10) Pennycook, T. J.; McBride, J. R.; Rosenthal, S. J.; Pennycook, S. J.; Pantelides, S. T. *Nano Lett.* **2012**, *12*, 3038–3042, DOI: 10.1021/nl3008727.

(11) Reiss, P.; Protière, M.; Li, L. *Small* **2009**, *5*, 154–168, DOI: 10.1002/smll.200800841.

(12) Smith, A. M.; Mohs, A. M.; Nie, S. *Nature Nanotechnology* **2009**, *4*, 56–63, DOI: 10.1038/nnano.2008.360.

(13) Boles, M. A.; Ling, D.; Hyeon, T.; Talapin, D. V. *Nat. Mater.* **2016**, *15*, 141–153, DOI: 10.1038/nmat4526.

(14) Rabouw, F. T.; Donega, C. d. M. *Top Curr Chem (Z)* **2016**, *374*, 58, DOI: 10.1007/s41061-016-0060-0.

(15) Park, Y.-S.; Bae, W. K.; Baker, T.; Lim, J.; Klimov, V. I. *Nano Lett.* **2015**, *15*, 7319–7328, DOI: 10.1021/acs.nanolett.5b02595.

(16) Fernée, M. J.; Tamarat, P.; Lounis, B. *Chem. Soc. Rev.* **2014**, *43*, 1311–1337, DOI: 10.1039/C3CS60209E.

(17) Pal, B. N.; Ghosh, Y.; Brovelli, S.; Laocharoensuk, R.; Klimov, V. I.; Hollingsworth, J. A.; Htoon, H. *Nano Lett.* **2012**, *12*, 331–336, DOI: 10.1021/nl203620f.

(18) La Croix, A. D.; O'Hara, A.; Reid, K. R.; Orfield, N. J.; Pantelides, S. T.; Rosenthal, S. J.; Macdonald, J. E. *Nano Lett.* **2017**, *17*, 909–914, DOI: 10.1021/acs.nanolett.6b04213.

(19) Nirmal, M.; Dabbousi, B. O.; Bawendi, M. G.; Macklin, J. J.; Trautman, J. K.; Harris, T. D.; Brus, L. E. *Nature* **1996**, *383*, 802–804, DOI: 10.1038/383802a0.

(20) Kuno, M.; Fromm, D. P.; Gallagher, A.; Nesbitt, D. J.; Micic, O. I.; Nozik, A. J. *Nano Lett.* **2001**, *1*, 557–564, DOI: 10.1021/nl010049i.

(21) Efros, A. L.; Rosen, M. *Phys. Rev. Lett.* **1997**, *78*, 1110–1113, DOI: 10.1103/PhysRevLett.78.1110.

(22) Rosen, S.; Schwartz, O.; Oron, D. *Phys. Rev. Lett.* **2010**, *104*, 157404, DOI: 10.1103/PhysRevLett.104.157404.

(23) Zhao, J.; Nair, G.; Fisher, B. R.; Bawendi, M. G. *Phys. Rev. Lett.* **2010**, *104*, 157403, DOI: 10.1103/PhysRevLett.104.157403.

(24) Frantsuzov, P. A.; Volkán-Kacsó, S.; Jankó, B. *Phys. Rev. Lett.* **2009**, *103*, 207402, DOI: 10.1103/PhysRevLett.103.207402.

(25) Frantsuzov, P. A.; Volkán-Kacsó, S.; Jankó, B. *Nano Lett.* **2013**, *13*, 402–408, DOI: 10.1021/nl3035674.

(26) Galland, C.; Ghosh, Y.; Steinbrück, A.; Sykora, M.; Hollingsworth, J. A.; Klimov, V. I.; Htoon, H. *Nature* **2011**, *479*, 203–207, DOI: 10.1038/nature10569.

(27) Tenne, R.; Teitelboim, A.; Rukenstein, P.; Dyshel, M.; Mokari, T.; Oron, D. *ACS Nano* **2013**, *7*, 5084–5090, DOI: 10.1021/nn4017845.

(28) Yuan, G.; Gómez, D. E.; Kirkwood, N.; Boldt, K.; Mulvaney, P. *ACS Nano* **2018**, *12*, 3397–3405, DOI: 10.1021/acsnano.7b09052.

(29) Efros, A. L.; Nesbitt, D. J. *Nat. Nanotechnol.* **2016**, *11*, 661–671, DOI: 10.1038/nnano.2016.140.

(30) Brokmann, X.; Coolen, L.; Dahan, M.; Hermier, J. P. *Phys. Rev. Lett.* **2004**, *93*, 107403, DOI: 10.1103/PhysRevLett.93.107403.

(31) Brokmann, X.; Hermier, J.-P.; Messin, G.; Desbiolles, P.; Bouchaud, J.-P.; Dahan, M. *Phys. Rev. Lett.* **2003**, *90*, 120601, DOI: 10.1103/PhysRevLett.90.120601.

(32) Empedocles, S. A.; Norris, D. J.; Bawendi, M. G. *Phys. Rev. Lett.* **1996**, *77*, 3873–3876, DOI: 10.1103/PhysRevLett.77.3873.

(33) Empedocles, S. A.; Neuhauser, R.; Shimizu, K.; Bawendi, M. G. *Advanced Materials* **1999**, *11*, 1243–1256, DOI: 10.1002/(SICI)1521-4095(199910)11:15<1243::AID-ADMA1243>3.0.CO;2-2.

(34) Cui, J.; Beyler, A. P.; Coropceanu, I.; Cleary, L.; Avila, T. R.; Chen, Y.; Cordero, J. M.; Heathcote, S. L.; Harris, D. K.; Chen, O.; Cao, J.; Bawendi, M. G. *Nano Lett.* **2016**, *16*, 289–296, DOI: 10.1021/acs.nanolett.5b03790.

(35) Empedocles, S. A.; Bawendi, M. G. *Science* **1997**, *278*, 2114–2117, DOI: 10.1126/science.278.5346.2114.

(36) McBride, J. R.; Pennycook, T. J.; Pennycook, S. J.; Rosenthal, S. J. *ACS Nano* **2013**, *7*, 8358–8365, DOI: 10.1021/nn403478h.

(37) Schlegel, G.; Bohnenberger, J.; Potapova, I.; Mews, A. *Phys. Rev. Lett.* **2002**, *88*, 137401, DOI: 10.1103/PhysRevLett.88.137401.

(38) Zhang, K.; Chang, H.; Fu, A.; Alivisatos, A. P.; Yang, H. *Nano Lett.* **2006**, *6*, 843–847, DOI: 10.1021/nl060483q.

(39) Nair, G.; Zhao, J.; Bawendi, M. G. *Nano Lett.* **2011**, *11*, 1136–1140, DOI: 10.1021/nl104054t.

(40) Murray, C. B.; Norris, D. J.; Bawendi, M. G. *J. Am. Chem. Soc.* **1993**, *115*, 8706–8715, DOI: 10.1021/ja00072a025.

(41) van Embden, J.; Jasieniak, J.; Mulvaney, P. *J. Am. Chem. Soc.* **2009**, *131*, 14299–14309, DOI: 10.1021/ja9030209.

(42) Williams, D. B.; Carter, C. B., *Transmission Electron Microscopy: A Textbook for Materials Science*, 2nd ed.; Springer US: 2009.

(43) McBride, J. R.; Kippeny, T. C.; Pennycook, S. J.; Rosenthal, S. J. *Nano Lett.* **2004**, *4*, 1279–1283, DOI: 10.1021/nl049406q.

(44) McBride, J.; Treadway, J.; Feldman, L. C.; Pennycook, S. J.; Rosenthal, S. J. *Nano Lett.* **2006**, *6*, 1496–1501, DOI: 10.1021/nl060993k.

(45) Phillips, P. J.; Paulauskas, T.; Rowlands, N.; Nicholls, A. W.; Low, K.-B.; Bhadare, S.; Klie, R. F. *Microscopy and Microanalysis* **2014**, *20*, 1046–1052, DOI: 10.1017/S1431927614001639.

(46) Ebenstein, Y.; Mokari, T.; Banin, U. *Appl. Phys. Lett.* **2002**, *80*, 4033–4035, DOI: 10.1063/1.1482785.

(47) Koberling, F.; Mews, A.; Philipp, G.; Kolb, U.; Potapova, I.; Burghard, M.; Basché, T. *Appl. Phys. Lett.* **2002**, *81*, 1116–1118, DOI: 10.1063/1.1499221.

(48) Orfield, N. J.; McBride, J. R.; Keene, J. D.; Davis, L. M.; Rosenthal, S. J. *ACS Nano* **2015**, *9*, 831–839, DOI: 10.1021/nn506420w.

(49) Dukes, A. D.; Samson, P. C.; Keene, J. D.; Davis, L. M.; Wikswo, J. P.; Rosenthal, S. J. *J. Phys. Chem. A* **2011**, *115*, 4076–4081, DOI: 10.1021/jp1109509.

(50) Michler, P.; Imamoğlu, A.; Mason, M. D.; Carson, P. J.; Strouse, G. F.; Buratto, S. K. *Nature* **2000**, *406*, 968–970, DOI: 10.1038/35023100.

(51) Fox, M., *Quantum Optics: An Introduction*; OUP Oxford: 2006.

(52) Alivisatos, A. P. *J. Phys. Chem.* **1996**, *100*, 13226–13239, DOI: 10.1021/jp9535506.

(53) Chen, O.; Zhao, J.; Chauhan, V. P.; Cui, J.; Wong, C.; Harris, D. K.; Wei, H.; Han, H.-S.; Fukumura, D.; Jain, R. K.; Bawendi, M. G. *Nat Mater* **2013**, *12*, 445–451, DOI: 10.1038/nmat3539.

(54) Chen, Y.; Vela, J.; Htoon, H.; Casson, J. L.; Werder, D. J.; Bussian, D. A.; Klimov, V. I.; Hollingsworth, J. A. *J. Am. Chem. Soc.* **2008**, *130*, 5026–5027, DOI: 10.1021/ja711379k.

(55) Shirasaki, Y.; Supran, G. J.; Bawendi, M. G.; Bulović, V. *Nat Photon* **2013**, *7*, 13–23, DOI: 10.1038/nphoton.2012.328.

(56) Dang, C.; Lee, J.; Breen, C.; Steckel, J. S.; Coe-Sullivan, S.; Nurmikko, A. *Nature Nanotechnology* **2012**, *7*, 335–339, DOI: 10.1038/nnano.2012.61.

(57) Lin, X.; Dai, X.; Pu, C.; Deng, Y.; Niu, Y.; Tong, L.; Fang, W.; Jin, Y.; Peng, X. *Nature Communications* **2017**, *8*, 1132, DOI: 10.1038/s41467-017-01379-6.

(58) Efros, A. L.; Rosen, M.; Kuno, M.; Nirmal, M.; Norris, D. J.; Bawendi, M. *Phys. Rev. B* **1996**, *54*, 4843–4856, DOI: 10.1103/PhysRevB.54.4843.

(59) Korkusinski, M.; Voznyy, O.; Hawrylak, P. *Phys. Rev. B* **2010**, *82*, 245304, DOI: 10.1103/PhysRevB.82.245304.

(60) Christodoulou, S.; Rajadell, F.; Casu, A.; Vaccaro, G.; Grim, J. Q.; Genovese, A.; Manna, L.; Climente, J. I.; Meinardi, F.; Rainò, G.; Stöferle, T.; Mahrt, R. F.; Planelles, J.; Brovelli, S.; Moreels, I. *Nature Communications* **2015**, *6*, 7905, DOI: 10.1038/ncomms8905.

(61) Yin, Y.; Alivisatos, A. P. *Nature* **2005**, *437*, 664–670, DOI: 10.1038/nature04165.

(62) Reiss, P.; Protière, M.; Li, L. *Small* **2009**, *5*, 154–168, DOI: 10.1002/smll.200800841.

(63) Chuang, S. L.; Chang, C. S. *Phys. Rev. B* **1996**, *54*, 2491–2504, DOI: 10.1103/PhysRevB.54.2491.

(64) Cui, J.; Beyler, A. P.; Bischof, T. S.; Wilson, M. W. B.; Bawendi, M. G. *Chem. Soc. Rev.* **2014**, *43*, 1287–1310, DOI: 10.1039/C3CS60330J.

(65) Pietryga, J. M.; Park, Y.-S.; Lim, J.; Fidler, A. F.; Bae, W. K.; Brovelli, S.; Klimov, V. I. *Chem. Rev.* **2016**, *116*, 10513–10622, DOI: 10.1021/acs.chemrev.6b00169.

(66) Akopian, N.; Lindner, N. H.; Poem, E.; Berlatzky, Y.; Avron, J.; Gershoni, D.; Gerardot, B. D.; Petroff, P. M. *physica status solidi (b)* **2006**, *243*, 3900–3904, DOI: 10.1002/pssb.200671523.

(67) Park, Y.-S.; Malko, A. V.; Vela, J.; Chen, Y.; Ghosh, Y.; García-Santamaría, F.; Hollingsworth, J. A.; Klimov, V. I.; Htoon, H. *Phys. Rev. Lett.* **2011**, *106*, 187401, DOI: 10.1103/PhysRevLett.106.187401.

(68) Zhao, J.; Chen, O.; Strasfeld, D. B.; Bawendi, M. G. *Nano Lett.* **2012**, *12*, 4477–4483, DOI: 10.1021/nl3013727.

(69) Klimov, V. I.; Mikhailovsky, A. A.; McBranch, D. W.; Leatherdale, C. A.; Bawendi, M. G. *Science* **2000**, *287*, 1011–1013, DOI: 10.1126/science.287.5455.1011.

(70) Carbone, L. et al. *Nano Lett.* **2007**, *7*, 2942–2950, DOI: 10.1021/nl0717661.

(71) Yu, W. W.; Qu, L.; Guo, W.; Peng, X. *Chem. Mater.* **2003**, *15*, 2854–2860, DOI: 10.1021/cm034081k.

(72) Kim, T.-H.; Jun, S.; Cho, K.-S.; Choi, B. L.; Jang, E. *MRS Bulletin* **2013**, *38*, 712–720, DOI: 10.1557/mrs.2013.184.

(73) Chang, J. C.; Rosenthal, S. J. *J. Phys. Chem. Lett.* **2013**, *4*, 2858–2866, DOI: 10.1021/jz401071g.

(74) Schreuder, M. A.; Xiao, K.; Ivanov, I. N.; Weiss, S. M.; Rosenthal, S. J. *Nano Lett.* **2010**, *10*, 573–576, DOI: 10.1021/nl903515g.

(75) Takata, H.; Naiki, H.; Wang, L.; Fujiwara, H.; Sasaki, K.; Tamai, N.; Masuo, S. *Nano Lett.* **2016**, *16*, 5770–5778, DOI: 10.1021/acs.nanolett.6b02479.

(76) Derfus, A. M.; Chan, W. C. W.; Bhatia, S. N. *Nano Lett.* **2004**, *4*, 11–18, DOI: 10.1021/nl0347334.

(77) Xie, R.; Battaglia, D.; Peng, X. *J. Am. Chem. Soc.* **2007**, *129*, 15432–15433, DOI: 10.1021/ja076363h.

(78) Tamang, S.; Lincheneau, C.; Hermans, Y.; Jeong, S.; Reiss, P. *Chem. Mater.* **2016**, *28*, 2491–2506, DOI: 10.1021/acs.chemmater.5b05044.

(79) Gary, D. C.; Terban, M. W.; Billinge, S. J. L.; Cossairt, B. M. *Chem. Mater.* **2015**, *27*, 1432–1441, DOI: 10.1021/acs.chemmater.5b00286.

(80) Lim, J.; Bae, W. K.; Lee, D.; Nam, M. K.; Jung, J.; Lee, C.; Char, K.; Lee, S. *Chem. Mater.* **2011**, *23*, 4459–4463, DOI: 10.1021/cm201550w.

(81) Kim, K.; Lee, H.; Ahn, J.; Jeong, S. *Appl. Phys. Lett.* **2012**, *101*, 073107, DOI: 10.1063/1.4745844.

(82) Mahler, B.; Spinicelli, P.; Buil, S.; Quelin, X.; Hermier, J.-P.; Dubertret, B. *Nat Mater* **2008**, *7*, 659–664, DOI: 10.1038/nmat2222.

(83) Hinuma, Y.; Grüneis, A.; Kresse, G.; Oba, F. *Phys. Rev. B* **2014**, *90*, 155405, DOI: 10.1103/PhysRevB.90.155405.

(84) Wei, S.-H.; Zhang, S. B.; Zunger, A. *Journal of Applied Physics* **2000**, *87*, 1304–1311, DOI: 10.1063/1.372014.

(85) Keene, J. D.; McBride, J. R.; Orfield, N. J.; Rosenthal, S. J. *ACS Nano* **2014**, *8*, 10665–10673, DOI: 10.1021/nn504235w.

(86) Lim, J.; Park, M.; Bae, W. K.; Lee, D.; Lee, S.; Lee, C.; Char, K. *ACS Nano* **2013**, *7*, 9019–9026, DOI: 10.1021/nn403594j.

(87) Yang, X.; Zhao, D.; Leck, K. S.; Tan, S. T.; Tang, Y. X.; Zhao, J.; Demir, H. V.; Sun, X. W. *Adv. Mater.* **2012**, *24*, 4180–4185, DOI: 10.1002/adma.201104990.

(88) Pietra, F.; De Trizio, L.; Hoekstra, A. W.; Renaud, N.; Prato, M.; Grozema, F. C.; Baesjou, P. J.; Koole, R.; Manna, L.; Houtepen, A. J. *ACS Nano* **2016**, *10*, 4754–4762, DOI: 10.1021/acsnano.6b01266.

(89) Bae, W. K.; Padilha, L. A.; Park, Y.-S.; McDaniel, H.; Robel, I.; Pietryga, J. M.; Klimov, V. I. *ACS Nano* **2013**, *7*, 3411–3419, DOI: 10.1021/nn4002825.

(90) Frantsuzov, P. A.; Volkán-Kacsó, S.; Jankó, B. *Phys. Rev. Lett.* **2009**, *103*, 207402, DOI: 10.1103/PhysRevLett.103.207402.

(91) Kuno, M.; Fromm, D. P.; Hamann, H. F.; Gallagher, A.; Nesbitt, D. J. *The Journal of Chemical Physics* **2000**, *112*, 3117–3120, DOI: 10.1063/1.480896.

(92) Frantsuzov, P.; Kuno, M.; Jankó, B.; Marcus, R. A. *Nat Phys* **2008**, *4*, 519–522, DOI: 10.1038/nphys1001.

(93) Orfield, N. J.; McBride, J. R.; Wang, F.; Buck, M. R.; Keene, J. D.; Reid, K. R.; Htoon, H.; Hollingsworth, J. A.; Rosenthal, S. J. *ACS Nano* **2016**, *10*, 1960–1968, DOI: 10.1021/acsnano.5b05876.

(94) Cros-Gagneux, A.; Delpech, F.; Nayral, C.; Cornejo, A.; Coppel, Y.; Chaudret, B. *J. Am. Chem. Soc.* **2010**, *132*, 18147–18157, DOI: 10.1021/ja104673y.

(95) Harris, D. K.; Bawendi, M. G. *J. Am. Chem. Soc.* **2012**, *134*, 20211–20213, DOI: 10.1021/ja309863n.

(96) Gary, D. C.; Cossairt, B. M. *Chem. Mater.* **2013**, *25*, 2463–2469, DOI: 10.1021/cm401289j.

(97) Scholes, G. D.; Rumbles, G. *Nat. Mater.* **2006**, *5*, 683–696, DOI: 10.1038/nmat1710.

(98) Frecker, T.; Bailey, D.; Arzeta-Ferrer, X.; McBride, J.; Rosenthal, S. J. *ECS J. Solid State Sci. Technol.* **2016**, *5*, R3019–R3031, DOI: 10.1149/2.0031601jss.

(99) Kagan, C. R.; Murray, C. B. *Nat. Nanotechnol.* **2015**, *10*, 1013–1026, DOI: 10.1038/nnano.2015.247.

(100) Reid, K. R.; McBride, J. R.; Freymeyer, N. J.; Thal, L. B.; Rosenthal, S. J. *Nano Lett.* **2018**, *18*, 709–716, DOI: 10.1021/acs.nanolett.7b03703.

(101) Niezgoda, J. S.; Harrison, M. A.; McBride, J. R.; Rosenthal, S. J. *Chem. Mater.* **2012**, *24*, 3294–3298, DOI: 10.1021/cm3021462.

(102) Vanmaekelbergh, D.; Casavola, M. *J. Phys. Chem. Lett.* **2011**, *2*, 2024–2031, DOI: 10.1021/jz200713j.

(103) Talapin, D. V.; Koeppe, R.; Götzinger, S.; Kornowski, A.; Lupton, J. M.; Rogach, A. L.; Benson, O.; Feldmann, J.; Weller, H. *Nano Lett.* **2003**, *3*, 1677–1681, DOI: 10.1021/nl034815s.

(104) Xing, G.; Chakrabortty, S.; Ngiam, S. W.; Chan, Y.; Sum, T. C. *J. Phys. Chem. C* **2011**, *115*, 17711–17716, DOI: 10.1021/jp205238q.

(105) Sitt, A.; Hadar, I.; Banin, U. *Nano Today* **2013**, *8*, 494–513, DOI: 10.1016/j.nantod.2013.08.002.

(106) Borys, N. J.; Walter, M. J.; Huang, J.; Talapin, D. V.; Lupton, J. M. *Science* **2010**, *330*, 1371–1374, DOI: 10.1126/science.1198070.

(107) Wu, K.; Hill, L. J.; Chen, J.; McBride, J. R.; Pavlopolous, N. G.; Richey, N. E.; Pyun, J.; Lian, T. *ACS Nano* **2015**, *9*, 4591–4599, DOI: 10.1021/acsnano.5b01245.

(108) Cunningham, P. D.; Souza, J. B.; Fedin, I.; She, C.; Lee, B.; Talapin, D. V. *ACS Nano* **2016**, *10*, 5769–5781, DOI: 10.1021/acsnano.5b07949.

(109) Castelli, A.; Meinardi, F.; Pasini, M.; Galeotti, F.; Pinchetti, V.; Lorenzon, M.; Manna, L.; Moreels, I.; Giovanella, U.; Brovelli, S. *Nano Lett.* **2015**, *15*, 5455–5464, DOI: 10.1021/acs.nanolett.5b01849.

(110) Yong, K.-T.; Qian, J.; Roy, I.; Lee, H. H.; Bergey, E. J.; Tramposch, K. M.; He, S.; Swihart, M. T.; Maitra, A.; Prasad, P. N. *Nano Lett.* **2007**, *7*, 761–765, DOI: 10.1021/nl063031m.

(111) Bronstein, N. D.; Li, L.; Xu, L.; Yao, Y.; Ferry, V. E.; Alivisatos, A. P.; Nuzzo, R. G. *ACS Nano* **2014**, *8*, 44–53, DOI: 10.1021/nn404418h.

(112) Müller, J.; Lupton, J. M.; Lagoudakis, P. G.; Schindler, F.; Koeppe, R.; Rogach, A. L.; Feldmann, J.; Talapin, D. V.; Weller, H. *Nano Lett.* **2005**, *5*, 2044–2049, DOI: 10.1021/nl051596x.

(113) Pisanello, F.; Leménager, G.; Martiradonna, L.; Carbone, L.; Vezzoli, S.; Desfonds, P.; Cozzoli, P. D.; Hermier, J.-P.; Giacobino, E.; Cingolani, R.; Vittorio, M. D.; Bramati, A. *Adv. Mater. 25*, 1974–1980, DOI: 10.1002/adma.201203171.

(114) Talapin, D. V.; Nelson, J. H.; Shevchenko, E. V.; Aloni, S.; Sadtler, B.; Alivisatos, A. P. *Nano Lett.* **2007**, *7*, 2951–2959, DOI: 10.1021/nl072003g.

(115) Javaux, C.; Mahler, B.; Dubertret, B.; Shabaev, A.; Rodina, A. V.; Efros, A. L.; Yakovlev, D. R.; Liu, F.; Bayer, M.; Camps, G.; Biadala, L.; Buil, S.; Quelin, X.; Hermier, J.-P. *Nat. Nanotechnol.* **2013**, *8*, 206–212, DOI: 10.1038/nnano.2012.260.

(116) Rabouw, F. T.; Lunnemann, P.; van Dijk-Moes, R. J. A.; Frimmer, M.; Pietra, F.; Koenderink, A. F.; Vanmaekelbergh, D. *Nano Lett.* **2013**, *13*, 4884–4892, DOI: 10.1021/nl4027567.

(117) Klimov, V. I.; McGuire, J. A.; Schaller, R. D.; Rupasov, V. I. *Phys. Rev. B* **2008**, *77*, 195324, DOI: 10.1103/PhysRevB.77.195324.

(118) Spinicelli, P.; Buil, S.; Quélin, X.; Mahler, B.; Dubertret, B.; Hermier, J.-P. *Phys. Rev. Lett.* **2009**, *102*, 136801, DOI: 10.1103/PhysRevLett.102.136801.

(119) Fisher, B. R.; Eisler, H.-J.; Stott, N. E.; Bawendi, M. G. *J. Phys. Chem. B* **2004**, *108*, 143–148, DOI: 10.1021/jp035756+.

(120) Kambhampati, P. *J. Phys. Chem. C* **2011**, *115*, 22089–22109, DOI: 10.1021/jp2058673.

(121) García-Santamaría, F.; Brovelli, S.; Viswanatha, R.; Hollingsworth, J. A.; Htoon, H.; Crooker, S. A.; Klimov, V. I. *Nano Lett.* **2011**, *11*, 687–693, DOI: 10.1021/nl103801e.

(122) Cragg, G. E.; Efros, A. L. *Nano Lett.* **2010**, *10*, 313–317, DOI: 10.1021/nl903592h.

(123) Frantsuzov, P.; Kuno, M.; Jankó, B.; Marcus, R. A. *Nat. Phys.* **2008**, *4*, 519–522, DOI: 10.1038/nphys1001.

(124) Lifshitz, E.; Dag, I.; Litvitn, I. D.; Hodes, G. *J. Phys. Chem. B* **1998**, *102*, 9245–9250, DOI: 10.1021/jp981880v.

(125) Voznyy, O.; Sargent, E. H. *Phys. Rev. Lett.* **2014**, *112*, 157401, DOI: 10.1103/PhysRevLett.112.157401.

(126) Coropceanu, I.; Rossinelli, A.; Caram, J. R.; Freyria, F. S.; Bawendi, M. G. *ACS Nano* **2016**, *10*, 3295–3301, DOI: 10.1021/acsnano.5b06772.

(127) Gong, K.; Kelley, D. F. *J. Phys. Chem. Lett.* **2015**, *6*, 1559–1562, DOI: 10.1021/acs.jpclett.5b00566.

(128) Demortière, A.; Leonard, D. N.; Petkov, V.; Chapman, K.; Chattopadhyay, S.; She, C.; Cullen, D. A.; Shibata, T.; Pelton, M.; Shevchenko, E. V. *J. Phys. Chem. Lett.* **2018**, *9*, 1900–1906, DOI: 10.1021/acs.jpclett.8b00914.

(129) Diroll, B. T.; Gogotsi, N.; Murray, C. B. *Chem. Mater.* **2016**, *28*, 3345–3351, DOI: 10.1021/acs.chemmater.6b00376.

(130) Taylor, J.; Kippeny, T.; Rosenthal, S. J. *J. Clust. Sci.* **2001**, *12*, 571–582, DOI: 10.1023/A:1014246315331.

(131) McGuire, J. A.; Sykora, M.; Robel, I.; Padilha, L. A.; Joo, J.; Pietryga, J. M.; Klimov, V. I. *ACS Nano* **2010**, *4*, 6087–6097, DOI: 10.1021/nn1016296.

(132) Rabouw, F. T.; Kamp, M.; van Dijk-Moes, R. J. A.; Gamelin, D. R.; Koenderink, A. F.; Meijerink, A.; Vanmaekelbergh, D. *Nano Lett.* **2015**, *15*, 7718–7725, DOI: 10.1021/acs.nanolett.5b03818.

(133) Knowles, K. E.; McArthur, E. A.; Weiss, E. A. *ACS Nano* **2011**, *5*, 2026–2035, DOI: 10.1021/nn2002689.

(134) Wu, K.; Rodríguez-Córdoba, W. E.; Liu, Z.; Zhu, H.; Lian, T. *ACS Nano* **2013**, *7*, 7173–7185, DOI: 10.1021/nn402597p.

(135) Wu, K.; Du, Y.; Tang, H.; Chen, Z.; Lian, T. *J. Am. Chem. Soc.* **2015**, *137*, 10224–10230, DOI: 10.1021/jacs.5b04564.

(136) Nasilowski, M.; Spinicelli, P.; Patriarche, G.; Dubertret, B. *Nano Lett.* **2015**, *15*, 3953–3958, DOI: 10.1021/acs.nanolett.5b00838.

(137) Rabouw, F. T.; van der Bok, J. C.; Spinicelli, P.; Mahler, B.; Nasilowski, M.; Pedetti, S.; Dubertret, B.; Vanmaekelbergh, D. *Nano Lett.* **2016**, *16*, 2047–2053, DOI: 10.1021/acs.nanolett.6b00053.

(138) Jones, M.; Lo, S. S.; Scholes, G. D. *Proc. Natl. Acad. Sci. U.S.A.* **2009**, *106*, 3011–3016.

(139) Abdellah, M.; Karki, K. J.; Lenngren, N.; Zheng, K.; Pascher, T.; Yartsev, A.; Pullerits, T. *J. Phys. Chem. C* **2014**, *118*, 21682–21686, DOI: 10.1021/jp506536h.

(140) Voznyy, O. *J. Phys. Chem. C* **2011**, *115*, 15927–15932, DOI: 10.1021/jp205784g.

(141) Gómez-Campos, F. M.; Califano, M. *Nano Lett.* **2012**, *12*, 4508–4517, DOI: 10.1021/nl3016279.

(142) Saniepay, M.; Mi, C.; Liu, Z.; Abel, E. P.; Beaulac, R. *J. Am. Chem. Soc.* **2018**, *140*, 1725–1736, DOI: 10.1021/jacs.7b10649.

(143) Mooney, J.; Krause, M. M.; Saari, J. I.; Kambhampati, P. *Phys. Rev. B* **2013**, *87*, 081201, DOI: 10.1103/PhysRevB.87.081201.

(144) Verberk, R.; van Oijen, A. M.; Orrit, M. *Phys. Rev. B* **2002**, *66*, 233202, DOI: 10.1103/PhysRevB.66.233202.

(145) Utterback, J. K.; Grennell, A. N.; Wilker, M. B.; Pearce, O. M.; Eaves, J. D.; Dukovic, G. *Nat. Chem.* **2016**, *8*, 1061–1066, DOI: 10.1038/nchem.2566.

(146) Utterback, J. K.; Hamby, H.; Pearce, O. M.; Eaves, J. D.; Dukovic, G. *J. Phys. Chem. C* **2018**, *122*, 16974–16982, DOI: 10.1021/acs.jpcc.8b05031.

(147) Eshet, H.; Grünwald, M.; Rabani, E. *Nano Lett.* **2013**, *13*, 5880–5885, DOI: 10.1021/nl402722n.

(148) Cline, R. P.; Utterback, J. K.; Strong, S. E.; Dukovic, G.; Eaves, J. D. *J. Phys. Chem. Lett.* **2018**, *9*, 3532–3537, DOI: 10.1021/acs.jpclett.8b01148.

(149) Angeloni, I.; Raja, W.; Brescia, R.; Polovitsyn, A.; De Donato, F.; Canepa, M.; Bertoni, G.; Proietti Zaccaria, R.; Moreels, I. *ACS Photonics* **2016**, *3*, 58–67, DOI: 10.1021/acsphotonics.5b00626.

(150) Janke, E. M.; Williams, N.; She, C.; Zherebetskyy, D.; Hudson, M.; Wang, L.; Gosztola, D. J.; Schaller, R. D.; Lee, B.; Sun, C.; Engel, G. S.; Talapin, D. V. *J. Am. Chem. Soc.* **2018**, DOI: 10.1021/jacs.8b08753.

(151) Bladt, E.; van Dijk-Moes, R. J. A.; Peters, J.; Montanarella, F.; de Mello Donega, C.; Vanmaekelbergh, D.; Bals, S. *J. Am. Chem. Soc.* **2016**, *138*, 14288–14293, DOI: 10.1021/jacs.6b06443.

(152) Semonin, O. E.; Johnson, J. C.; Luther, J. M.; Midgett, A. G.; Nozik, A. J.; Beard, M. C. *J. Phys. Chem. Lett.* **2010**, *1*, 2445–2450, DOI: 10.1021/jz100830r.

(153) Bruns, O. T. et al. *Nature Biomedical Engineering* **2017**, *1*, 0056, DOI: 10.1038/s41551-017-0056.